NOTICE TO BORROWERS

In presenting this dissertation as partial fulfillment of the requirements for an advanced degree from Georgia State University, I agree that the library of the university will make it available for inspection and circulation in accordance with its regulations governing materials of this type. I agree that permission to quote from, to copy from, or to publish from this dissertation may be granted by the author, by the professor under whose direction it was written, or by the Dean of the College of Arts and Sciences. Such quoting, copying, or publishing must be solely for scholarly purposes and must not involve potential financial gain. It is understood that any copying from or publication of this dissertation that involves potential financial gain will not be allowed without written permission of the author.

All dissertations and theses deposited in the Georgia State University Library may be used only in accordance with the stipulations prescribed by the author in the preceding statement.

The author of this dissertation is

Nils Henning Turner
P.O. Box 17654
Atlanta, Georgia 30316-0654

The director of this dissertation is

Theo A. ten Brummelaar
Department of Physics and Astronomy
College of Arts and Sciences

A Prototype Imager for the CHARA Array

A Dissertation

Presented in Partial Fulfillment of Requirements for the
Degree of Doctor of Philosophy
in the College of Arts and Sciences
Georgia State University

1997

by

Nils Henning Turner

Committee:

Theo A. ten Brummelaar, Chair

William G. Bagnuolo, Jr., Member

Douglas R. Gies, Member

Harold A. McAlister, Member

James E. Purcell, Member

Mark A. Shure, Member

Date

William H. Nelson, Chair
Department of Physics and Astronomy

Abstract

Traditional methods of data collection in active fringe tracking Michelson stellar interferometers involve logging and analyzing the signals within the fringe tracking system for the scientific information about the object being observed. While these methods are robust and have produced excellent scientific results, they become more problematic as next-generation Michelson stellar interferometers are built with more telescopes and the aim of performing routine imaging.

The Center for High Angular Resolution Astronomy (CHARA) Array is one such next-generation instrument presently under construction on Mount Wilson, north of Los Angeles, California. The CHARA Array will feature a separation of the tasks of active fringe tracking and imaging, thereby increasing the bandwidth, sensitivity, and data acquisition rate. Presented is a prototype version of an imager for the CHARA Array. The prototype imager employs single-mode fiber optic strands to convey the light from simulated telescopes to a smaller, non-redundant, remapped pupil plane, which in turn feeds a low resolution prism spectrograph. The spectrograph features two cylindrical optical elements whose net effect is to focus the light to a smaller plate scale in the spectral dimension than in the orthogonal spatial dimension. The actual Array imager will build on lessons learned from the prototype and will include capability for five telescopes, further degrees of freedom in adjustment, a computer interface, and automatic intensity calibration.

Acknowledgements

Gee, where do I start? I have been at GSU for a long time and so many people have been a part of my success here. I will start by thanking my parents, Dale and Ilo Turner, for always being there. They have supported me emotionally and financially through some turbulent times, and for that I am most grateful. It has been a real joy watching our relationship transform from me being their son to me being their friend and confidant, as well as son.

I would like to thank all my graduate student colleagues, both past and present, for helping me to get through the "graduate experience" relatively unscathed, from helping me avert boredom in class and backpacking trips to building fences and seeing the latest special effects extravaganza movie. These include (but are not limited to), John Hildebrand, Jim Kinney, Lewis Roberts, Brian Mason, Victor Bellitto, Bill Lee, Don Barry, Tony Kaye, Michelle Thaller, Reed Riddle, and Elizabeth Ferrara.

I would also like to thank Charles Hopper, Jim Stephenson, Kerry Whitetree, and Carleton Mitchum for their patience in having me, day after day, in the Physics and Astronomy machine shop. Their good nature and helpful suggestions went a long way to making this dissertation a success.

Before I forget, I want to thank one of my undergraduate mentors at the University of Wyoming, Mel Dyck. Mel introduced me to the field of interferometry and encouraged me to attend Georgia State University. Indirectly, his words of advice have kept me going when the research front looked bleak and private employment looked tempting.

Thanks are due to all the faculty and staff in the Physics and Astronomy department. Their efficiency and (financial) support were quite a windfall. Chief among these that I would like to single out are Hal McAlister and Theo ten Brummelaar. Throughout the years, Hal kept his confidence in me and provided me with support

to travel to conferences, to travel on observing runs, to work with other interferometer groups (IOTA), and to lift my spirits when the Atlanta experience was less than charming. It is an honor to work with him. I have only known Theo for five years, but it feels like he is a pal from way back. Theo has been so helpful in getting past some of the technical stumbling blocks of building the imager and getting it to work. Yet, his importance goes much deeper. No matter how bad things got, you could always count on Theo to come up with a joke to keep things light yet still keep focused. I look forward to being his friend and colleague for many years to come. Others in the department (past and present) that have made a large impact on me (who I will miss dearly) are Bill Hartkopf, Bill Bagnuolo, Ingemar Furenlid (whom we tragically lost), Doug Gies, Sandy Land, John Wilson, and Mark Shure.

In the land outside of astronomy I am indebted to the likes of people like Sallie Cruise, the Road to Ruin String Band, and the members of the Atlanta Flying Disc Club. Sallie has been so cheerful and upbeat throughout the time I have known her. It is so much fun to catch up on the latest events, tell about my ultimate exploits, and in general, practice the gift of gab. The Road to Ruin String Band (Theo ten Brummelaar, Sallie Cruise, Doug Gies, John Jackson, Bill Pounds, and myself) has been an excellent outlet for those creative energies. They taught me about the fun of folk music and the importance of friendship in group endeavors. The Atlanta Flying Disc Club and its events have been a mainstay in my social life since coming to Atlanta. It has been a boon to be able to find a game of ultimate when things were not going well in the lab. There is nothing like running around chasing a piece of spinning plastic to get you really tired physically, sleeping well, and coming back to the project with a fresh mind.

My dissertation committee deserves special commendation. They had to put up with my constantly slipping deadlines and a writing style that is usually too terse or too verbose, rarely that happy medium in between. They include Theo ten Brummelaar, Hal McAlister, Bill Bagnuolo, Doug Gies, Jim Purcell, and Mark Shure.

Finally, I would like to give special thanks to Renee Moog and Dennis and Sharon Cryor for providing me a place to stay when my lease ran out and the imager was just not helping me finish on time.

For all these people, I am grateful. Thank you.

Contents

List of Tables

List of Figures

Chapter 1

Introduction to Michelson Stellar Interferometry

To measure the angular extent of a star (or separation between stars in the case of a binary star system) using Michelson stellar interferometry, the observer stops down a larger telescope into two subapertures. Ideally, the diameters would match r_0 (Section 1.3.1) and be adjustable in separation. If the angular extent being measured is small enough, interference fringes will still be visible on the widest sub-aperture separation. However, if the angular extent is larger, at some sub-aperture separation, the fringes would disappear, and the angular extent can be derived. Michelson used this technique to measure the angular sizes of the main moons of Jupiter (Michelson 1891) and, with a modification to the Mount Wilson 100" telescope (Michelson and Pease 1921), to measure the angular diameter of Betelgeuse (α Orionis).

As technology progressed, the sub-apertures were no longer confined to the same telescope structure, and modern Michelson stellar interferometry was born. At present, it is poised to make significant contributions to the field of stellar astrophysics. Following McAlister (1985), these anticipated contributions include determinations of binary star separations and position angles and stellar diameters, limb darkening, effective temperatures, and rotation. By calculating properties such as luminosities and masses from the above observables, one can test the validity of stellar atmosphere models. The present generation of optical/IR Michelson stellar interferometers, with the design goal of rapid and routine data collection, will take the first step by providing high quality and quantity of stellar astrophysical data.

This dissertation describes the design study and prototype construction of an imager for one such Michelson stellar interferometer, the CHARA Array. A refinement of the prototype will go a long way toward the goal of making the collection of stellar astrophysical data both rapid and routine.

1.1 Basic Principles of Interference

The mathematical treatment of multiple beam interference begins with an analysis of the superposition of electromagnetic waves. The electric field component of the wave equation, derived from Maxwell's equations,

$$\nabla^2 E - \frac{n^2}{c^2}\frac{\partial^2 E}{\partial t^2} = 0,$$

where n is the index of refraction of the medium and c the speed of light in vacuum, yields solutions of the form,

$$E = Ae^{i\phi_t}, \tag{1.1}$$

where A is the amplitude of the wave, and ϕ_t is the phase, given as

$$\begin{aligned} \phi_t &= (\omega t - 2\pi w x) + \varphi. \\ &= \omega t + \phi \end{aligned} \tag{1.2}$$

In equation 1.2, w (the letter "w") is the wavenumber $(1/\lambda)$ and φ is a phase associated with the source. Note also in equation 1.2 that ϕ_t is time dependent. Detection of radiation is a time-averaging process involving the square of the E-field. For this allow

$$\begin{aligned} E &= A\cos(\phi_t) \\ &= A\cos(\omega t + \phi), \end{aligned}$$

and

$$\begin{aligned} E^2 &= A^2 \cos^2(\omega t + \phi) \\ &= A^2[\cos \omega t \cos \phi - \sin \omega t \sin \phi]^2 \\ &= A^2[\cos^2 \omega t \cos^2 \phi - 2 \cos \omega t \sin \omega t \cos \phi \sin \phi + \sin^2 \omega t \sin^2 \phi]. \end{aligned}$$

Taking the time average,

$$\begin{aligned} E^2 &= A^2 \Big[\Big(\frac{1}{2}\Big) \cos^2 \phi - (0) + \Big(\frac{1}{2}\Big) \sin^2 \phi \Big] \\ &= \frac{A^2}{2}. \end{aligned}$$

Superposing two time-averaged waves,

$$E = E_1 + E_2,$$

where the solution in equation 1.1 is now given as

$$E = Ae^{i\phi},$$

the square of the amplitude of the resulting wave becomes,

$$\begin{aligned} A^2 &= E \cdot E^* \\ &= (\Re(E))^2 + (\Im(E))^2 \\ &= (A_1 \cos \phi_1 + A_2 \cos \phi_2)^2 + (A_1 \sin \phi_1 + A_2 \sin \phi_2)^2 \\ &= A_1^2 + A_2^2 + 2A_1 A_2 \cos(\phi_2 - \phi_1). \end{aligned}$$

By use of the vacuum permittivity constant (ϵ_0), the relationship between intensity and the electric field is given as,

$$\begin{aligned} I &= \frac{c\epsilon_0}{n} E^2 \\ &= \frac{c\epsilon_0}{2n} A^2 \\ &= \frac{c\epsilon_0}{2n} \Big[A_1^2 + A_2^2 + 2A_1 A_2 \cos(\phi_2 - \phi_1) \Big]. \end{aligned} \tag{1.3}$$

Since

$$\frac{c\epsilon_0}{2n}A_1^2 = I_1,$$

and

$$\frac{c\epsilon_0}{2n}A_2^2 = I_2,$$

the combined intensity can be written as,

$$\begin{aligned} I &= I_1 + I_2 + 2\sqrt{I_1 I_2}\cos(\phi_2 - \phi_1) \\ &= I_1 + I_2 + 2\sqrt{I_1 I_2}\cos \mathrm{d}, \end{aligned} \tag{1.4}$$

where

$$\begin{aligned} \mathrm{d} &= -2\pi w(x_2 - x_1) - (\varphi_2 - \varphi_1) \\ &= -2\pi w(x_2 - x_1) + \varphi_{12}^{\mathrm{obs}}. \end{aligned} \tag{1.5}$$

1.1.1 Coherence and Finite Bandpass

For actual signals encountered in nature, equation 1.4 needs to be modified for at least two effects, object coherence and finite bandwidth. Equation 1.4 shows a sinusoidal variation which is strictly an artifact of the interferometric signal detection. Information about the source is found by investigating the object coherence. Due to the lengthiness of a rigorous derivation, the result will be stated without proof. For more complete derivations, see Born and Wolf (1989), Chapter 10 or Klein and Furtak (1986), Chapter 8. The effect of object coherence is to modulate the sinusoidal function in equation 1.4 with another function known as the *coherence* function of the source. Equation 1.4 then becomes

$$I = I_1 + I_2 + 2\sqrt{I_1 I_2}|\gamma_{\mathrm{coherence}}|\cos \mathrm{d}. \tag{1.6}$$

Ignoring the complex nature of the coherence function, the effects of the source and beam intensities can be subsumed into a slightly different function known as the

visibility function. The visibility function is a measure of the contrast of the fringes – the ratio of the amplitude of the fringe pattern to the background intensity $(I_1 + I_2)$. Equation 1.6 can be rewritten as

$$I = I_1 + I_2 + (I_1 + I_2)V(w)\cos \mathrm{d}. \tag{1.7}$$

The effect of a finite bandwidth modulates the sinusoidal term in equation 1.7 yet further. To see this, consider a few simplifications (which do not effect the general result). Let $I_1 = I_2 = \frac{1}{2}$, allow a normalization term, and allow the phases arising from the source to average to zero (by taking many samples over time). Equation 1.7 then becomes

$$\begin{aligned} I &= I_0\Big[1 + V(w)\cos(2\pi w(x_2 - x_1))\Big] \\ &= I_0\Big[1 + V(w)\cos(2\pi w\mathcal{D}(w))\Big], \end{aligned} \tag{1.8}$$

where $\mathcal{D}(w) = x_2 - x_1$. Note that $\mathcal{D}(w)$ is a function of the wavenumber. The path length difference between two arms of ground-based interferometers will involve at least two different media, air and vacuum. Air and any transmission optics used are wavenumber dependent. Consider a filter of central wavenumber w_0 and width Δw. The shape of the bandpass is a step function; the transmission is zero when $w < w_0 - \Delta w/2$ and $w > w_0 + \Delta w/2$ and one when $w_0 - \Delta w/2 < w < w_0 + \Delta w/2$. The total intensity becomes

$$\begin{aligned} I(w_0, \Delta w) &= \frac{1}{\Delta w}\int_{w_0-\Delta w/2}^{w_0+\Delta w/2}\Big[1 + V(w)\cos(2\pi w\mathcal{D}(w))\Big]dw \\ &\simeq 1 + \frac{V(w_0)}{\Delta w}\int_{w_0-\Delta w/2}^{w_0+\Delta w/2}\cos(2\pi w\mathcal{D}(w_0))dw \\ &\simeq 1 + \frac{V(w_0)}{2\pi\mathcal{D}(w_0)\Delta w}\sin(2\pi w\mathcal{D}(w_0))\Big|_{w_0-\Delta w/2}^{w_0+\Delta w/2} \\ &\simeq 1 + V(w_0)\frac{\sin(\pi\mathcal{D}(w_0)\Delta w)}{\pi\mathcal{D}(w_0)\Delta w}\cos(\pi\mathcal{D}(w_0)w_0) \end{aligned} \tag{1.9}$$

where equation 1.9 is obtained through the use of one of the trigonometric factoring identities. Note that dispersion is basically ignored in that $\mathcal{D}(w)$ is taken to be a

constant, $\mathcal{D}(w_0)$. Dispersion will be addressed in Section 6.5.2.

1.1.2 Channel Fringes

As can be seen in equation 1.9, the argument of the cosine function is wavenumber dependent. Therefore, if one were to spread the signal spectrally across the detector, each wavenumber in the spectrum would have a different fringe spacing. As the difference in path length changes between the two arms of the interferometer ($\mathcal{D}$), the number of fringes visible in the spectrum, $\mathcal{N}$, changes, which can be represented as

$$\mathcal{N} = \mathcal{D} \cdot (w_{\max} - w_{\min}).$$

Channel fringes are useful in group delay fringe tracking (Section 3.1.5), enabling the operation of an interferometer at lower light levels than fringe phase tracking (Section 3.1.4).

1.1.3 Fourier Analysis

In practice, Fourier analysis techniques are used to extract the information about fringe frequencies in the detected intensity. The Fourier transform of a function $f(x)$ is given as

$$\mathcal{F}\Big[f(x)\Big] = \int_{-\infty}^{\infty} f(x) e^{-i2\pi ux} dx.$$

If equation 1.8 is set to $f(x)$ and the the source visiblity set to one, the Fourier transform becomes

$$\begin{aligned}
\mathcal{F}\Big[I(w)\Big] &= \int_{-\infty}^{\infty} \Big[1 + \cos(2\pi\mathcal{D}w)\Big] e^{-i2\pi uw} dw \\
&= \int_{-\infty}^{\infty} e^{-i2\pi uw} dw + \int_{-\infty}^{\infty} \cos(2\pi\mathcal{D}w) e^{-i2\pi uw} dw \\
&= \delta(u) + \frac{1}{2}\Big[\delta(u - \mathcal{D}) + \delta(u + \mathcal{D})\Big] \qquad (1.10)
\end{aligned}$$

Generally, the Fourier transform is a complex quantity. So, in order to find the peaks in the transform, the square of the modulus of the transform is calculated. This operation is known as finding the *power spectrum*. Calculating the power spectrum of equation 1.10, one gets

$$\mathcal{F}\Big[I(w)\Big]\mathcal{F}^*\Big[I(w)\Big] = \delta(u) + \frac{1}{4}\delta(u-\mathcal{D}) + \frac{1}{4}\delta(u+\mathcal{D}) \tag{1.11}$$

Note in equation 1.11 that there are three delta function peaks, a large peak centered at 0 with two smaller peaks at $\pm\mathcal{D}$. When a sinusoidal function is transformed, the power spectrum is symmetric about the y-axis, and as a result, only positive values are usually plotted.

1.2 The van Cittert–Zernike Theorem

An electromagnetic disturbance occurs at a position $\boldsymbol{R}$ in the universe. Spherical waves propagate away from that position to eventually be detected by an observer at a position $\boldsymbol{r}$. Following Clark (1994), a number of simplifying assumptions are adopted to make the functional form tractable. First of all, the vector nature of the fields is suppressed (polarization is ignored). Next, the three dimensional nature of the source is projected to the two dimensions of the celestial sphere, essentially only allowing determination of a "surface brightness". Thirdly, the space between the source and the observer is empty. Also, the source is assumed to be spatially incoherent – radiation from two different spots on the source is statistically independent. And finally, the radiation is assumed to be quasi-monochromatic – the frequencies of light involved in the superposition are clustered near some central value.

Because the space between is empty, Huygen's Principle (Born and Wolf 1989) can be used to describe the propagation,

$$E_\nu^{\rm obs}(\boldsymbol{r}) = \iint\limits_{\rm surface} E_\nu^{\rm src}(\boldsymbol{R})\frac{e^{\frac{i2\pi\nu|\boldsymbol{R}-\boldsymbol{r}|}{c}}}{|\boldsymbol{R}-\boldsymbol{r}|}dS, \tag{1.12}$$

where $E^{\rm obs}$ and $E^{\rm src}$ are the electric fields at the observation and source positions respectively. If two observation points are chosen, a *spatial coherence function* (in optical astronomy, it is frequently known as a *complex visibility function*) can be

defined as

$$V_\nu(\boldsymbol{r}_1, \boldsymbol{r}_2) = \langle E_\nu^{\rm obs}(\boldsymbol{r}_1) E_\nu^{\rm obs\,*}(\boldsymbol{r}_2)\rangle. \tag{1.13}$$

Because the source radiation is assumed to be incoherent, the expectation product of the source fields of equation 1.13 is only non-zero when $\boldsymbol{R}_1 = \boldsymbol{R}_2$. Therefore, combining equations 1.12 and 1.13 one gets the following,

$$V_\nu(\boldsymbol{r}_1, \boldsymbol{r}_2) = \iint\limits_{\rm surface} \langle |E_\nu^{\rm src}(\boldsymbol{R})|^2\rangle |\boldsymbol{R}|^2 \frac{e^{\frac{-i2\pi\nu(|\boldsymbol{R}-\boldsymbol{r}_2|-|\boldsymbol{R}-\boldsymbol{r}_1|)}{c}}}{|\boldsymbol{R}-\boldsymbol{r}_1||\boldsymbol{R}-\boldsymbol{r}_2|} dS. \tag{1.14}$$

In equation 1.14, the origin can be arranged to be close to the observer. The great distance between the source and the observer makes $\boldsymbol{R} \gg \boldsymbol{r}$. Equation 1.14 then becomes,

$$V_\nu(\boldsymbol{r}_1, \boldsymbol{r}_2) \simeq \int\limits_{\rm solid\ angle} I_\nu(\hat{\boldsymbol{R}}) e^{\frac{-i2\pi\nu\hat{\boldsymbol{R}}\cdot(\boldsymbol{r}_1-\boldsymbol{r}_2)}{c}} d\Omega, \tag{1.15}$$

where $I_\nu(\hat{\boldsymbol{R}})$ has replaced $\langle |E_\nu^{\rm src}(\boldsymbol{R})|^2\rangle |\boldsymbol{R}|^2$ (in a manner similar to equation 1.3), and the integral has been converted from a surface integral to a solid angle integral. By choosing a convenient two-dimenstional coordinate system containing the interferometer baseline $(\boldsymbol{r}_1 - \boldsymbol{r}_2)$, equation 1.15 can be expressed in terms of direction cosines. In this coordinate system, the z-axis is in the direction of the source, the x-axis is parallel to the projection of the baseline, and the y-axis is orthogonal to both of them ($l = \cos\theta_x$; $m = \cos\theta_y$). Consequently, the unit vector in the direction of the source, $\hat{\boldsymbol{R}}$, has coordinate values of $(l, m, \sqrt{1-l^2-m^2})$, making this explicit in equation 1.15, one gets

$$V_\nu(u, v) \simeq \iint I_\nu(l, m) \frac{e^{-i2\pi(ul+vm)}}{\sqrt{1-l^2-m^2}} dl dm. \tag{1.16}$$

Note that equation 1.16 is in the form of a two-dimensional Fourier transform. All the information available about the source is contained in the complex visibility function. This is the incentive for measuring visibilities.

1.3 Imaging and Phase Closure

As is described in every text dealing with physical optics, the process of image formation involves the Fourier transform of the transmission function of the aperture plane (Born and Wolf 1989; Klein and Furtak 1986). With filled-in aperture instruments such as single-mirror telescopes, the complex visibility function shown in equation 1.16 has data for all values of u and v up to the edge of the mirror. This is to say that there is visibility information for all "baselines" up to a maximum separation of the diameter of the telescope mirror. In interferometry, the visibility information is not so densely packed, but the area of the uv-plane touched upon is much larger. There is a visiblity "point" for each baseline. The word "point" has been put in quotes to remind one that there is in fact a clustering of (u, v) points at each nominal baseline because of the non-infinitesimal size of the individual telescopes in the interferometer. In addition, interferometers are usually located on the Earth, which rotates. As a result, the baseline at which a visibility is measured is a projection of the physical baseline (layed out on the Earth) to the uv-plane. During the course of observation, the group of visibility "points" will trace out an ellipse segment.

1.3.1 Atmospheric Turbulence

Most interferometers are built on the Earth. Observing with these interferometers involves looking through the atmosphere at a distant object. Small temperature changes ($< 1°$C) in the atmosphere cause random changes in wind velocity, creating turbulent eddies. These eddies cause changes to the mean index of refraction of the air, and accumulated over a long path through the atmosphere, they create the three main effects of atmospheric *seeing*: *twinkling* (or *scintillation*) – random intensity fluctuations due to interference phenomena as light from the same star passes through slightly different paths on the way to the observer; *quiver* – random motion of the apparent position of the star relative to the mean position due to angle-of-arrival changes; and *spreading* – the effect of moving light power farther away from the core in the diffraction pattern, simulating a more highly aberrated optical system.

Tyson (1991) describes the basics of turbulence in the literature with the aim of defining the needs of an adaptive optics system. Tango and Twiss (1980) describe

a condensed version and how it applies to Michelson stellar interferometry. This summary is a condensation of Tyson (1991). Kolmogorov (1961) investigated the mean-square velocity difference between two points in space and defined a structure tensor, D_{ij}. Assuming that the atmosphere is isotropic and homogeneous, as well as the turbulence being incompressible, this structure tensor becomes a structure function,

$$D_v(r) = C_v^2 r^{\frac{2}{3}},$$

where r is the separation of the two points in space, and C_v^2 is the velocity structure constant, a measure of the energy in the turbulence. The velocity structure constant holds as long as the value of r is larger than l_0, the smallest sized eddy (the *inner scale*) and smaller than L_0, the largest sized eddy (the *outer scale*). Typically, $l_0 \sim 3$ mm while $L_0 \sim 3$ m. Tatarskii (1961) related the velocity structure to an index of refraction structure,

$$D_n(r) = C_n^2 r^{\frac{2}{3}},$$

where now,

$$l_0 \ll r \ll L_0.$$

An important benchmark can be created by assuming the atmosphere to be made up of a mean index of refraction part and a fluctuating index of refraction part. The Fourier transform of the covariance of this field gives the power spectral density of the atmosphere, a measure of how the turbulent power is distributed at various spatial scales. After performing the ensemble averaging in the covariance, the spectrum, expressed in spherical coordinates, is given as

$$\begin{aligned} \Phi_n(K) &= \frac{5}{18\pi} C_n^2 K^{-3} \int_{l_0}^{L_0} \sin(Kr) r^{-\frac{1}{3}} dr \\ &= (0.033) C_n^2 K^{-\frac{11}{3}}, \end{aligned} \tag{1.17}$$

where, in equation 1.17, the integral is evaluated for $l_0 = 0$ and $L_0 = \infty$. Equation 1.17 is known as the *Kolmogorov spectrum*.

Of interest to the task of imaging is knowing how the index of refraction structure of the atmosphere affects the expected phase of the wavefront. Because the fluctuations of the atmosphere are random, there is no way to know exactly which path a part of the wavefront used. However, knowing the index of refraction structure, a statistical averaging over the ways to pass through a path length of L allow the determination of a *phase structure function*,

$$D_\phi = (1.46)k^2 C_n^2 L \rho^{\frac{5}{3}},$$

where k is the wavenumber, and ρ is the distance between two parallel paths through the atmosphere. Fried (1965) defines a coherence length (also known as the *seeing cell* size), r_0, beyond which atmospheric distortion limits performance,

$$r_0 = \Big[\frac{(0.423)k^2}{\cos(\theta_{\text{zenith}})} \int_0^L C_n^2(h)dh\Big]^{-\frac{3}{5}},$$

where θ_{zenith} is the zenith angle, C_n^2 can vary with altitude h, and L is the path length. For Kolmogorov turbulence and plane wavefronts, the following relationship holds,

$$D_\phi = (6.88)\left(\frac{r}{r_0}\right)^{\frac{5}{3}}.$$

In addition to giving a quantitative measure of the phase structure function, r_0 is also used in characterization of the temporal behavior of the turbulent atmosphere. If the beam is larger than the seeing cell size, the time of interest is the time it takes the wind to transport the beam one seeing cell size,

$$\tau \simeq (0.53)\left(\frac{r_0}{v_{\text{wind}}}\right)\left(\frac{B}{r_0}\right)^{\frac{1}{6}},$$

where B is the beam diameter, and v_{wind} the wind velocity. At visible wavelengths, $\tau \sim 15$ milliseconds.

1.3.2 Phase Closure

Recall in equation 1.5 that there is a phase term which contains information about a particular *uv* point of the source (made explicit by combining the two phase terms in each arm). From Section 1.3.1, it becomes obvious that the atmosphere is going to modify φ_{12} and mask the phase information about the source. Radio interferometry has encountered these problems already. Cornwell and Fomalont (1994) state a general formulation of the relationship between the observed complex visibility function and the true complex visibility function (assuming well designed telescopes),

$$V_{ij}^{\text{obs}}(t) = g_i(t)g_j^*(t)V_{ij}(t) + \varsigma_{ij}(t), \tag{1.18}$$

where i and j represent two different telescopes, $g_i(t)$ represents the modifying effects of telescope i (including the effects of the atmosphere along the path to telescope i), and $\varsigma_{ij}(t)$ is a zero-mean thermal noise term (insignificant in the optical and near IR). The observed object phase term in equation 1.5 now becomes (ignoring the thermal term)

$$\varphi_{ij}^{\text{obs}} = \varphi_{ij} + \arg(g_i) - \arg(g_j).$$

The minus sign on the term of telescope j alone comes about because of the complex conjugate in equation 1.18. Jennison (1958) encountered this problem in the phase-unstable instruments of his time and came up with a solution, *phase closure*. If one calculates the sum of a group of three telescopes, C_{ijk}^{obs}, the error terms drop out,

$$\begin{aligned} C_{ijk}^{\text{obs}} &= \varphi_{ij}^{\text{obs}} + \varphi_{jk}^{\text{obs}} + \varphi_{ki}^{\text{obs}} \\ &= \varphi_{ij} + \arg(g_i) - \arg(g_j) + \varphi_{jk} + \arg(g_j) - \arg(g_k) + \varphi_{ki} + \arg(g_k) - \arg(g_i) \\ &= \varphi_{ij} + \varphi_{jk} + \varphi_{ki} \\ &= C_{ijk}. \end{aligned} \tag{1.19}$$

In practice, using phase closure information for imaging involves a few extra steps over straight Fourier inversion. First of all, the source should be modelled; a model such as a point source, two point sources, a uniformly illuminated disk, a limb-darkened disk, etc. The model provides estimates of the true phases on two

baselines, and the closure phase gives the value of the third phase. This provides a model refinement to provide better estimates of the true phases on the two baselines. The process is iterated until the model stabilizes. Strictly speaking, images could be created by starting with an empty model. However, the more information the phase closure imaging algorithm has about the model, the more robust the solution.

While phase closure is an indispensible tool for imaging in atmospherically degraded conditions, it does come at a price. For an interferometer of N telescopes, the number of baselines (and hence the maximum number of visibility phases available for imaging) is given as $\binom{N}{2}$. If phase closures are used, the number of independent measures drops to $\binom{N-1}{2}$. The binomial notation is given as,

$$\binom{N}{M} = \frac{N!}{(N-M)!M!}.$$

In addition, if the initial model is not good enough, the iteration process may never converge.

Related to phase closure is the issue of mappings. A mapping is a general concept. It can be applied to the overall layout of the telescopes on the Earth as well as subsets buried with the workings of the interferometer. The idea behind a mapping is to spatially encode the information about a given baseline. Recall the results of Thomas Young's double slit experiment (for example, Klein and Furtak 1986, pages 272–274). The intensity as a function of distance along a screen (for a fixed distance $\mathcal{R}$ from the slits) is given as

$$I_w(x) = I_0 \cos^2\left(\frac{\pi w a x}{\mathcal{R}}\right).$$

If one were to increase a, the slit spacing, the frequency of the fringes would increase (the spacing between one valley and the next would decrease). When one has more than two telescopes, it is conceivable to create a mapping which would encode the information from each baseline into its own fringe spacing on the detector. Fourier analysis techniques would then be used to extract the source information.

There are two general classes of mappings, redundant and non-redundant. In a redundant mapping, the individual telescopes are laid out on the Earth in such a way that the same uv point is sampled with two different telescope pairs. A redundant

mapping does have the advantage that it gives two (or more) independent measures of a phase closure, making the knowledge of a model less critical. A non-redundant mapping sacrifices the security of being more model independent, gaining greater uv coverage in the process. As alluded to previously, the image reconstruction process more critically depends on initial models. In practice, non-redundant mappings in optical and IR instruments perform best when reconstructing images of morphologically simple objects: unresolved point sources, uniform and limb-darkened disks, and additive combinations of the two.

Chapter 2

The CHARA Array

The Center for High Angular Resolution Astronomy (CHARA) Array is a five telescope, two-dimensional Michelson stellar interferometer currently under construction on Mount Wilson, north of Los Angeles, California. The project is jointly funded by the National Science Foundation (NSF) and Georgia State University. Project and scientific management are led by Harold A. McAlister of CHARA at Georgia State University (GSU). The main individuals involved in the CHARA Array are (in addition to McAlister) Stephen T. Ridgway (National Optical Astronomy Observatories), Theo A. ten Brummelaar (CHARA), William G. Bagnuolo, Jr.(CHARA), William I. Hartkopf (CHARA), Mark A. Shure (CHARA), Laszlo Sturmann (CHARA), Robert Cadman (CHARA), Nils H. Turner (CHARA), and Alexandra Land (CHARA). Progress on the Array is monitored in a series of technical reports that are published quarterly, and immediately upon publication are available through the World Wide Web at http://www.chara.gsu.edu/chara/. In addition to the technical report series, the original final report document to the NSF (McAlister et al. 1994) is available as well.

The Array features custom-designed one-meter aperture telescopes (actually *beam reducing* telescopes) located in a Y-shaped configuration within a 400 m diameter circle. Light incident upon the telescopes is reduced to a beam 12.5 cm in diameter (an 8:1 reduction) and conveyed to a central Beam Synthesis Facility (BSF) by means of a vacuum pipe. In the process of travelling to the BSF, the light from each of the telescopes undergoes the same number of reflections. Not only that, but the reflections are at nearly the same angles and in the same order. This is done to make

the polarization effects from beam transfer the same in all telescopes. Once inside the BSF, the light from each telescope, while still in vacuum, is fed into a constant path length offset system known as the Pipes of Pan (PoP, original conceptions of the path length offset system had the appearance of a pan pipe flute). The PoP allows the zero phase point of the Array as a whole to be some point on the celestial sphere other than the zenith. From here, the light goes through an Optical Path Length Equalizer (OPLE), one for each telescope. The OPLE systems are a modification of a Jet Propulsion Laboratory (JPL) design, the control system developed on the Mark III (Shao et al. 1988) and refined on the Navy Prototype Optical Interferometer (NPOI, Armstrong 1994). The OPLE systems are being built at GSU and assembled and integrated at JPL. Each OPLE system consists of a cats-eye reflector (an optical element in which the input and output beams are parallel, even when the cats-eye is slightly misaligned) on a cart under computer control to the sub-micron level. The light is then sent through another beam reducer to reduce the beam to 25 mm (a 5:1 reduction).

At this point, the light is split by wavelength using dichroic filters, reflecting IR for the IR system and transmitting the visible. The visible light is sent through atmospheric and longitudinal dispersion correctors, and through a beam "switchyard" to allow the light from any of the five telescopes to be at any of the beam positions within the fringe tracking system. The light is further split by polarization, using one polarization for fringe tracking and the other for imaging and tip-tilt correction. Fringe tracking will be accomplished using group delay tracking (Section 3.2) on two telescopes at a time. One OPLE system will be chosen as a reference, say 5. The zero path between baseline 5 and 4 will be maintained by moving OPLE 4, the zero path between baseline 4 and 3 will be maintained by moving OPLE 3, etc. (a schematic is shown in Figure 3.2). A prototype of the imaging system is described in this dissertation.

Presently (December 1997). the BSF has been completed. The manufacturer of the telescopes has begun assembly of the first two telescopes. Three pairs of matched telescope primary and secondary mirrors have been delivered. Parts for two OPLE carts have been built and JPL has demonstrated one working OPLE cart. Coarse OPLE rail alignment has been completed and finer alignment has been started. Concrete foundations have been laid for all five telescopes, complete with retaining

walls when required by terrain. One of these foundations (W2) has had a pier cast on top. Optical tables for the 5:1 beam reducer, atmospheric and longitudinal dispersion correctors, and beam switchyard have been delivered and installed. Optical tables for the fringe tracking system, IR imaging system, alignment system, and imaging system will be delivered and installed by early January 1998. The mirrors for the 5:1 beam reducer have been specified and ordered. Bids for the remaining optical mirror flats will be requested shortly. The enclosure domes have been completed and await shipment.

The last major task to be addressed is the vacuum beam transfer pipes that convey the light to the BSF. Preliminary design has been started and construction should begin early in the new construction season (April 1998). Also at the start of the new construction season, the remaining telescope piers will be cast and the control room building will be begun. By June 1998, the first two telescope enclosures (to be located at S1 and S2) will be complete, and by July 1998, the first two telescopes will be delivered and installed and telescope control software development can begin. In June 1998, the remaining two primary and secondary mirror pairs will be delivered. Development of the fringe tracking system will start in March 1998. Fine alignment of the OPLE rails will be completed by March 1998 and JPL will then demonstrate two (simultaneously) working OPLE carts. The remaining control systems will be delivered in April 1998. The remaining optical flat mirrors will be delivered in December 1998.

Chapter 3

Beam Combination Techniques

There are many ways in which one can combine the light from two or more telescopes. The beam combination choice in a particular design of interferometer is frequently made for practicality, simplicity, cost, available technology, and/or innovation. Before discussing how the beams from five telescopes are going to be combined in the CHARA Array, it is useful to look at how it has been done in the past.

3.1 Fringe Detection and Tracking

3.1.1 Passive Interference

The earliest optical/IR (amplitude) interferometers, which were two telescope interferometers, were generally passive devices. The instruments were designed to be stable. Since vibration is usually the most detrimental effect, the instruments were not designed to have many components in motion internally, usually, just the telescopes. Data were collected by estimating the zero path difference location between the two telescopes for some time in the future, say 90 seconds, setting the path length equalizer to that point, and waiting for the rotation of the Earth to bring the fringe packet across the detectors. This technique was used to great effect by the CERGA I2T (Koechlin 1988; Gay and Mekarnia 1988), and some very useful science was published as a result (Di Benedetto and Rabbia 1987).

Other interferometers that have used or are using this technique are IRMA (Benson et al. 1991) and FLUOR (Coudé du Foresto and Ridgway 1992). IOTA (Dyck

et al. 1995) uses a variation of this technique. Instead of waiting for Earth rotation to bring the interferometer through its zero path point, the path length compensator is driven at a certain speed to get the detected fringe packet frequency to lie above the noise level in the detectors. This improves the signal-to-noise ratio and also speeds up the observing cycle. It is worth noting here that the FLUOR beam combiner described in Coudé du Foresto and Ridgway (1992) is now in operation at IOTA (Coudé du Foresto et al. 1996).

3.1.2 Tango and Twiss Method

Tango and Twiss (1980) describe a theoretical method of measuring the coherence envelope to get an estimate of the visibility. In a very basic Michelson stellar interferometer, there is one beam splitter. Due to the nature of beam splitters, there is a π phase difference between the two outputs. As a result, the photon counts within the two channels, A and B, are related to the interference pattern by,

$$A \propto I_0\Big[1 + V(w)\cos(2\pi w\mathcal{D})\Big]$$

and

$$B \propto I_0\Big[1 - V(w)\cos(2\pi w\mathcal{D})\Big].$$

Note that at any given time, the total light in the system is $2I_0$. A visibility estimate can be made by performing the following operation,

$$\Big[V(w)\cos(2\pi w\mathcal{D})\Big]^2 = \frac{(A-B)^2}{(A+B)^2}. \tag{3.1}$$

3.1.3 Delay Curve Measurement

The first way of implementing the Tango and Twiss method is to view the path length changes induced by the atmosphere as a random quantity. If $\cos^2(2\pi w\mathcal{D})$ is averaged over many samples, equation 3.1 becomes,

$$\frac{V^2(w)}{2} = \frac{(A-B)^2}{(A+B)^2}.$$

Stepping through the coherence envelope and measuring visibilities along the way creates a *delay curve* (Davis and Tango 1986). A delay curve and knowledge of the shape of the bandpass allows the coherence envelope to be modelled and the object visibility to be calculated.

3.1.4 Path Length Modulation

The second way of implementing the Tango and Twiss method is to shift the phase of the system by one quarter every other sampling cycle. In the Mark III (Shao et al. 1988), this phase shift is done in time. When the system is near the object phase center, the path length in one of the arms is varied. The modulation is a triangle wave at 500 Hz where the amplitude of the triangle wave (valley to peak) is the wavelength of light at which the fringe phase is tracked. The data collection process involves dividing the time of one excursion (from a valley to a peak or a peak to a valley) equally into four bins and counting the number of photons in each bin. During that excursion (equivalent to 2π in phase), each bin will undergo a $\frac{\pi}{2}$ phase change, and the photon counts in each bin will be,

$$\begin{aligned}
A &\propto I_0\Big[1 + V(w)\cos(2\pi w\mathcal{D})\Big] \\
B &\propto I_0\Big[1 + V(w)\cos(2\pi w(\mathcal{D} + \lambda/4))\Big] \\
&\propto I_0\Big[1 - V(w)\sin(2\pi w\mathcal{D})\Big] \\
C &\propto I_0\Big[1 + V(w)\cos(2\pi w(\mathcal{D} + \lambda/2))\Big] \\
&\propto I_0\Big[1 - V(w)\cos(2\pi w\mathcal{D})\Big] \\
D &\propto I_0\Big[1 + V(w)\cos(2\pi w(\mathcal{D} + 3\lambda/4))\Big] \\
&\propto I_0\Big[1 + V(w)\sin(2\pi w\mathcal{D})\Big].
\end{aligned}$$

From this point it is very easy to see that,

$$2\pi w\mathcal{D} = \arctan\Big(\frac{A - C}{D - B}\Big)$$

and

$$V^2(w) \propto \frac{(A-C)^2 + (D-B)^2}{A+B+C+D}.$$

Besides the Mark III, other instruments using path length modulation for tracking fringes (or differentiating baselines) are the Cambridge Optical Aperture Synthesis Telescope (COAST, Boysen and Rogers 1992) and the Navy Prototype Optical Interferometer (NPOI, Armstrong 1994).

3.1.5 Group Delay Tracking

The final way to perform active fringe tracking is to use the channel spectrum in a technique known as group delay tracking. Following Lawson (1993), only one experiment prior to 1993, work done by Kim (1989) in conjunction with the Mark III, dealt with group delay fringe tracking with stellar light. In this technique, using a two-dimensional detector, the stellar light is dispersed along one axis of the detector. The effect of dispersion is to make the effective bandpass of the system wider, easing discovery of the observable coherence envelope. The relative path length between the two arms of the interferometer is adjusted until channel fringes are observed. On a two-dimensional detector, the channel fringes (near the point of zero path length difference, the zero path point) have a ray-like appearance (Bedding et al. 1992), each ray designated as the peak of the cosine curve. The central ray corresponds to the zero path point. Across a single spatial channel, there are no fringes. If one chooses a spatial channel on either side of the central one, there will be a non-zero number of fringes across it. The farther away from the central spatial channel, the more rays it crosses and hence, more observed fringes.

In practice, one tracks several spatial channels on either side of the central spatial channel because of the ambiguity of which way to correct when the atmosphere moves the fringes off center. ten Brummelaar (1997) describes the advantage of using group delay tracking over path length modulation. The chief advantage is that group delay tracking only requires one phase pixel per spectral channel and is wavelength independent while path length modulation requires four and is wavelength dependent and hence will have a brighter magnitude limit. In addition path length modulation with fail catastrophically while group delay tracking can be used in a passive tracking

mode and the information extracted during post-processing.

The CHARA Array will employ group delay tracking. In addition, the Sydney University Stellar Interferometer (SUSI, Davis 1993) employs it and the ASEPS-0 Palomar Test Bed Interferometer (Colavita et al. 1994). NPOI employs a hybrid of path length modulation (for differentiating baselines) and group delay tracking (allowing fringe tracking for dimmer objects).

3.2 Baseline Encoding

In two telescope interferometers there is only one baseline. The question of baseline encoding is not an issue. However, in the case of interferometers of three or more telescopes, encoding becomes important. For feasability, interferometers frequently remap the uv-plane. The astronomer needs to know how the internal instrument visibilities relate to the actual object visibilities.

There are two general ways of encoding the baseline information, *temporally* and *spatially*.

3.2.1 Temporal

In temporal encoding, there is a (known) time dependence on the instrument visibility. Path length modulation is an example of temporal encoding. In the case of the Mark III, the modulation was a simple triangle wave with a frequency of 500 Hz. Scaling up to a three telescope interferometer will require the addition of another path length equalizer and a control system to operate it. To acquire values for each of the time bins A–D, for both equalizer systems, it is most convenient to combine the light from all three telescopes into a common beam. However, if both path length modulators are operating at 500 Hz, there is an ambiguity of how to apply the error signal that is generated. So to get the system to work, the second equalizer has to run at a different frequency, by at least a factor of two, to avoid aliasing problems. In the optical, the atmosphere limits the servo loop to a minimum of 300 Hz.

There are two main problems scaling temporal encoding. First of all, with each additional telescope, the time bin becomes a factor of two shorter, and the magnitude limit of the instrument becomes correspondingly brighter. This problem can

be partially alleviated by operating two path length modulators in anti-phase (Armstrong 1994). However, it is not clear how a system would perform with *two* pairs of anti-phase path length modulators in simultaneous use. Secondly, at some point, the path length modulation system (usually a piezo-electric stack translator) can no longer keep up mechanically. Usually this means there is too much mass to move. This being said, two three-telescope interferometers using temporal encoding have achieved closure phase, COAST (Baldwin et al. 1996) and NPOI (Benson et al. 1997).

3.2.2 Spatial

In spatial encoding, as was touched upon in Section 1.3.2, the information about a baseline is stored according to the separation of the two channels. Additional channels can be added simply by choosing a location for the new channel such that the interference fringes formed by the new channel with each of the previous channels do not inhibit the detection and measurement of each of the previous sets of interference fringes. The information is then extracted using Fourier analysis. In most practical interferometers using (or intending to use) spatial encoding for imaging, the concept of spatial encoding becomes bit more opaque because there are usually two or more layers of spatially encoding – encoding the uv-plane of the sky and then remapping it into something more manageable in the various sub-systems.

While investigating the restrictions of remappings, ten Brummelaar and Bagnuolo (1994) found that the minimum separation between any two beams is comparable to two times the beam diameter. They found the relationship assuming a Rayleigh-like criterion, only this time, the peaks were in the Fourier rather than the image domain. Once the bases of the baseline peaks started to overlap, the measured peak positions changed. Figure 3.1 shows sample map patterns in two dimensions and one dimension for four beams. As will be shown in Section 3.4, the two-dimensional pattern requires smaller optics but a narrower bandpass, and the one-dimensional pattern, while requiring larger optics, lends itself well to use in spectrograph systems.

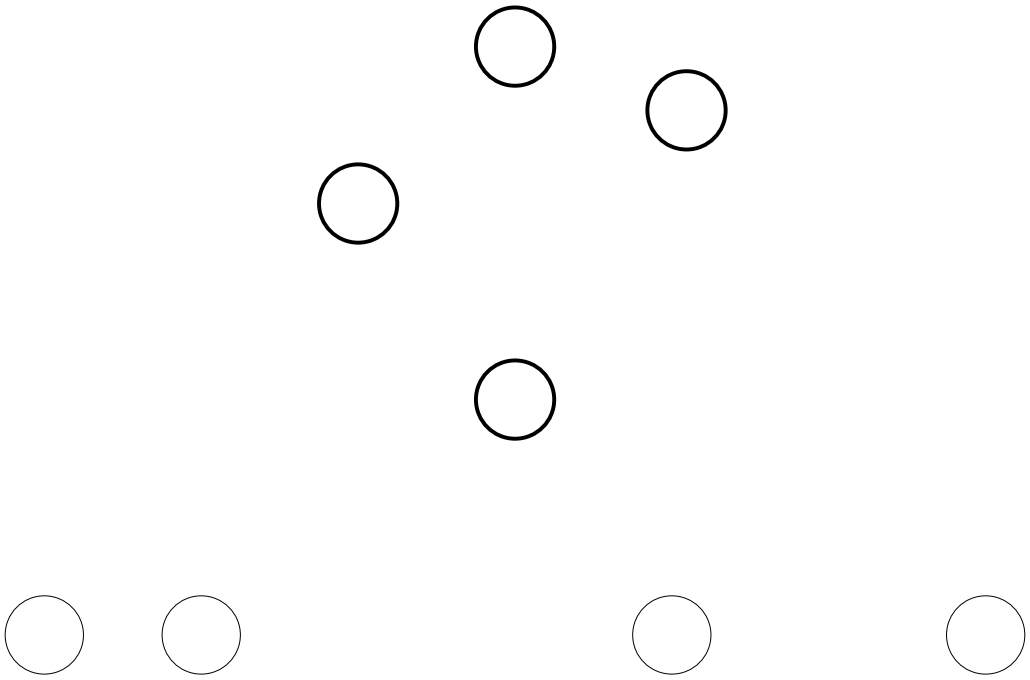

Figure 3.1: Here is shown two ways to map four beams. The bold circles are for a two-dimensional pattern while the normal circles are for an one-dimensional pattern. Note that the largest dimension in the one-dimensional pattern is larger than that of the two-dimensional pattern.

3.3 Separation of Fringe Tracking and Imaging

In developing the preliminary design for the CHARA Array data collection, ten Brummelaar and Bagnuolo (1994) make a convincing case for separating the tasks of fringe tracking and imaging. The main point of the argument is that active fringe tracking imposes some fairly stiff constraints on an imaging system that is part of the fringe tracking system (as temporally encoded systems require). An active fringe tracking system needs to collect data at rates fast enough to freeze the atmospheric fluctuations. This requirement means that the spectral bands have to be broad (but not too broad, as in the case of path length modulation) and necessarily coarse to collect enough light in the short integration time. In contrast, an imaging system does not have these requirements. If there is a fringe tracking system doing its job, the imaging system can passively collect its data with more appropriate integration times and high spectral resolutions to achieve a higher signal-to-noise ratio than would otherwise be possible if the imaging system were part of the fringe tracking system.

Separating the two systems has another tangible benefit which is important in the typical way interferometers are brought into operation – a development path. The more important system, active fringe tracking, could be brought up first. When the time comes to install the imaging system, the fringe tracking system will not have to be disturbed. Also, separate systems embolden one to build a more innovative (with its attendant risks) imaging system in the hope of making the beam combination task less expensive and more efficient. If the innovation does not pan out, the fringe tracking system can be used to collect scientific data.

3.4 Proposed CHARA Array Imager Designs

All of the following design proposals are discussed by ten Brummelaar and Bagnuolo (1994). At the time of that publication, the CHARA Array was to have seven telescopes. When full funding was not granted, the number of telescopes was reduced to five. However, in all critical construction areas where the addition of telescopes would require major renovation, space was allotted to handle up to eight telescopes.

In the imager/fringe-tracking decision making process, a figure of merit formulation was developed to weigh the pros and cons of a given design. In that formulation,

were values representing the number of optical surfaces, the number of reconfigurations required to obtain all baseline visibility measures and phase closures, the bandpass, and the detector efficiency. Though not explicitly included in the figure of merit, expense and complexity assisted in the final decision. Bandpass and detector efficiency are linked. Commercially available detectors tend to fall into two classes, single-pixel detectors and two-dimensional arrayed detectors. The single-pixel detector can be moderately efficient (40%) with no noise but are expensive (per pixel). Single-pixel detectors are integral in temporal encoding systems and require a narrow bandpass to function properly. Arrayed detectors are more efficient (70%) but with more noise, and are relatively inexpensive per pixel. They allow group delay tracking to be possible.

3.4.1 Three Way Beam Combiner

The first idea that comes to mind in designing an imager system is the extrapolation of the multiple-telescope fringe tracking system which is shown in Figure 3.2. One of the sides of the fringe tracking system can be sacrificed by swapping the mirrors for beam splitters, and another array of combined beams can be created. At the detector ends (single-pixel rather than two-dimensional) of the second array of beam splitters, each pair of output beams contain information from three telescopes, enough information to calculate a phase closure. A diagram of this proposed layout is shown in Figure 3.3. However, in the example given in Figure 3.3, for seven telescopes, there are only phase closures for seven of the fifteen possible. In order to get the other available phase closures, either the second array of beamsplitters needs to be re-arranged or the beams need to be switched at the input to the fringe tracking system. This method was abandoned early on due to the relatively high number of optical surfaces, low data throughput (five reconfigurations are required to acquire the fifteen phase closure measurements), and limited bandwidth. In addition, it was later discovered that the fringe tracking part and the imaging part could not simultaneously be in phase for all beam splitters.

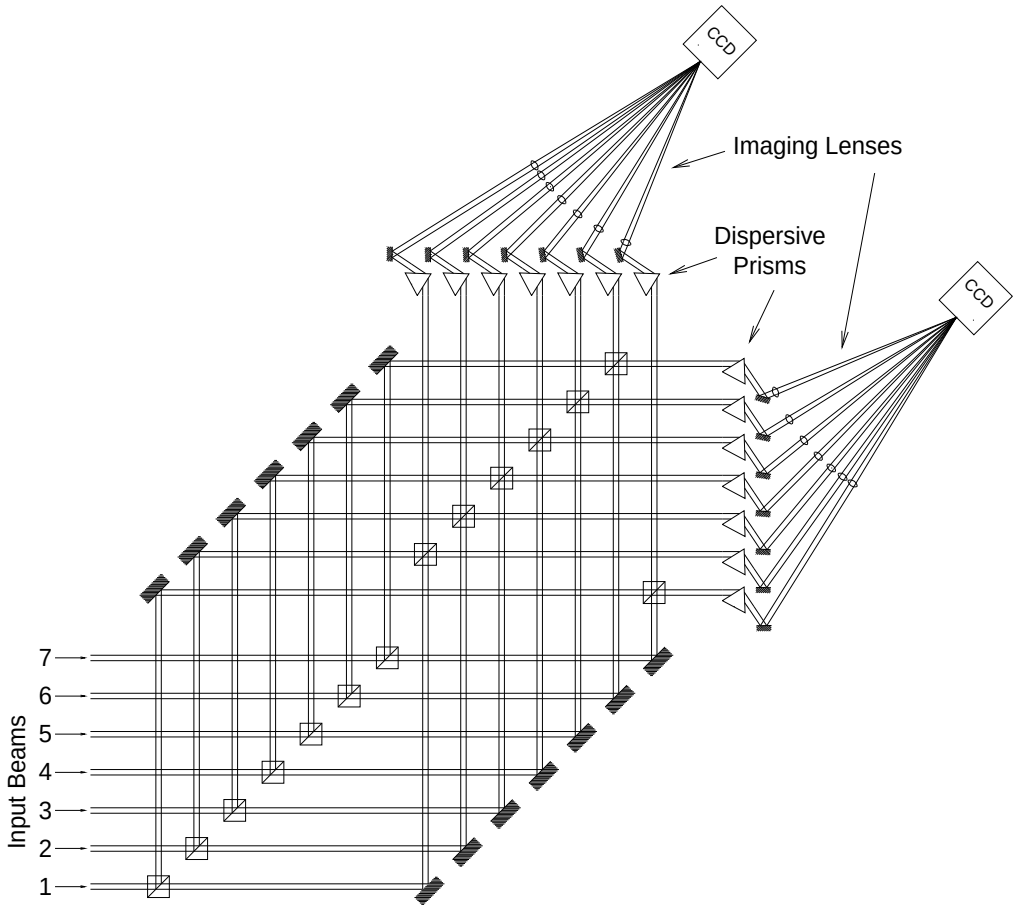

Figure 3.2: A schematic layout of a seven-telescope group delay fringe tracking system. As shown in this diagram, telescopes 7 and 6 are path length equalized, telescopes 6 and 5 . . . , and telescopes 1 and 7 are path length equalized to close the loop. Diagram courtesy of Theo ten Brummelaar.

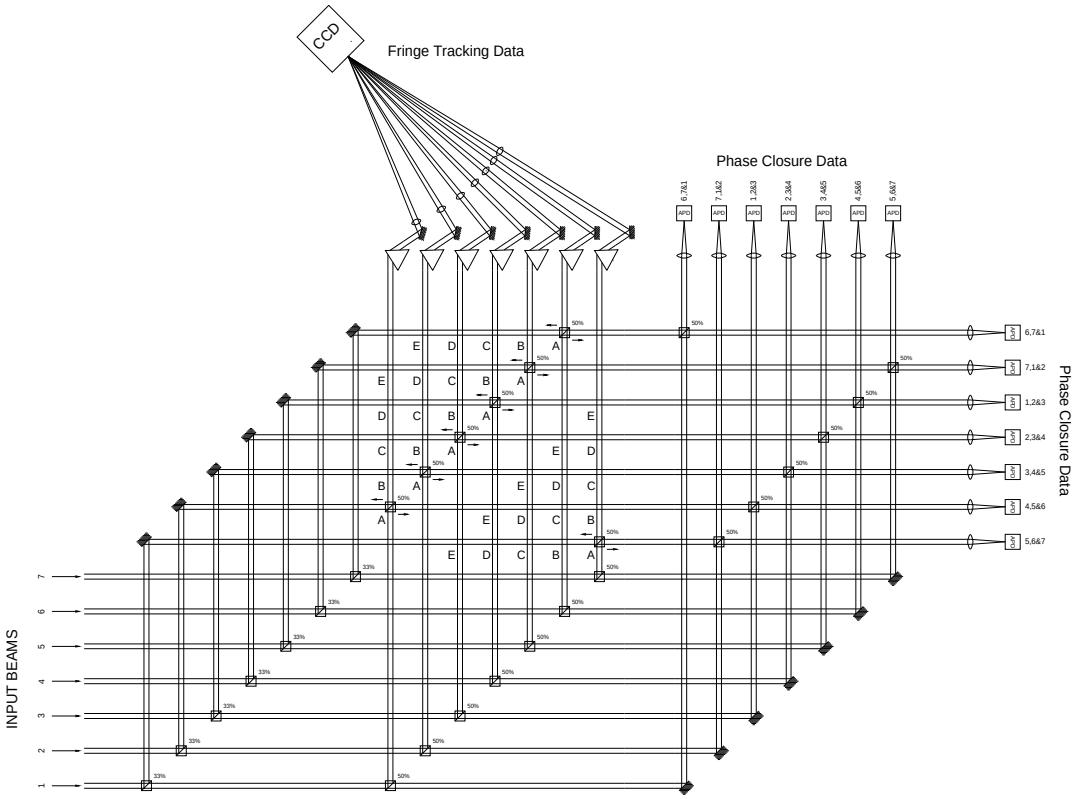

Figure 3.3: A schematic layout of a three way beam combiner. Note that the diagram also incorporates a fringe tracking system. Diagram courtesy of Theo ten Brummelaar.

3.4.2 All Beam Combiner

The COAST interferometer combines the light from four telescopes, creating four outputs with light from each of the four telescopes in each (Boysen and Rogers 1992). Figure 3.4 shows the COAST idea extended to eight telescopes (the COAST interferometer uses a beam combiner resembling one of the upper halves in Figure 3.4). Each telescope beam goes through three beam splitters on its way to one of eight single-pixel detectors. Again, this design was abandoned early on for several reasons. First of all, because information from all eight (it has to be a power of 2) is encoded at each detector, the temporal encoding algorithm that would be required to sort out the visibility and phase closure information exceeds by far the technical capability that any interferometry group has yet demonstrated. Secondly, the number and orientation of reflections is not consistent across the combiner. This can lead to polarization problems. Thirdly, additional reflections would have to be added to these beams to get them in a suitable configuration for this beam combination technique. These would have to be introduced with care to avoid introducing path length differences. Finally, as in the Three Way Combiner, the use of single-pixel detectors necessarily limits the usable bandwidth.

3.4.3 Remapped 1-D Non-Redundant Beam Combiner

In an effort to circumvent the temporal encoding problem and increase the bandwidth, designs were looked at that encoded the baselines spatially and used a spectrograph to disperse the light and keep the fringes (which have different frequencies at different wavelengths) from washing out. The first of these is shown in Figure 3.5. In this plan, one-dimensional, equally-spaced beams would undergo a complex set of reflections to be remapped into a one-dimensional, non-redundant pattern which would be incident on a beam reducing telescope designed to shrink the pattern to something the spectrograph can deal with. There are several disadvantages with this design. Chief among them is the large number of extra reflections introduced in the remapping procedure, several just to maintain path length equality and reflection symmetry in the beams. In addition, to combine seven beams simultaneously, the beam reducer would have to be very large. Assuming the 25 mm diameter beams in the CHARA Array after the final instrument beam reduction, the imager beam reducing telescope

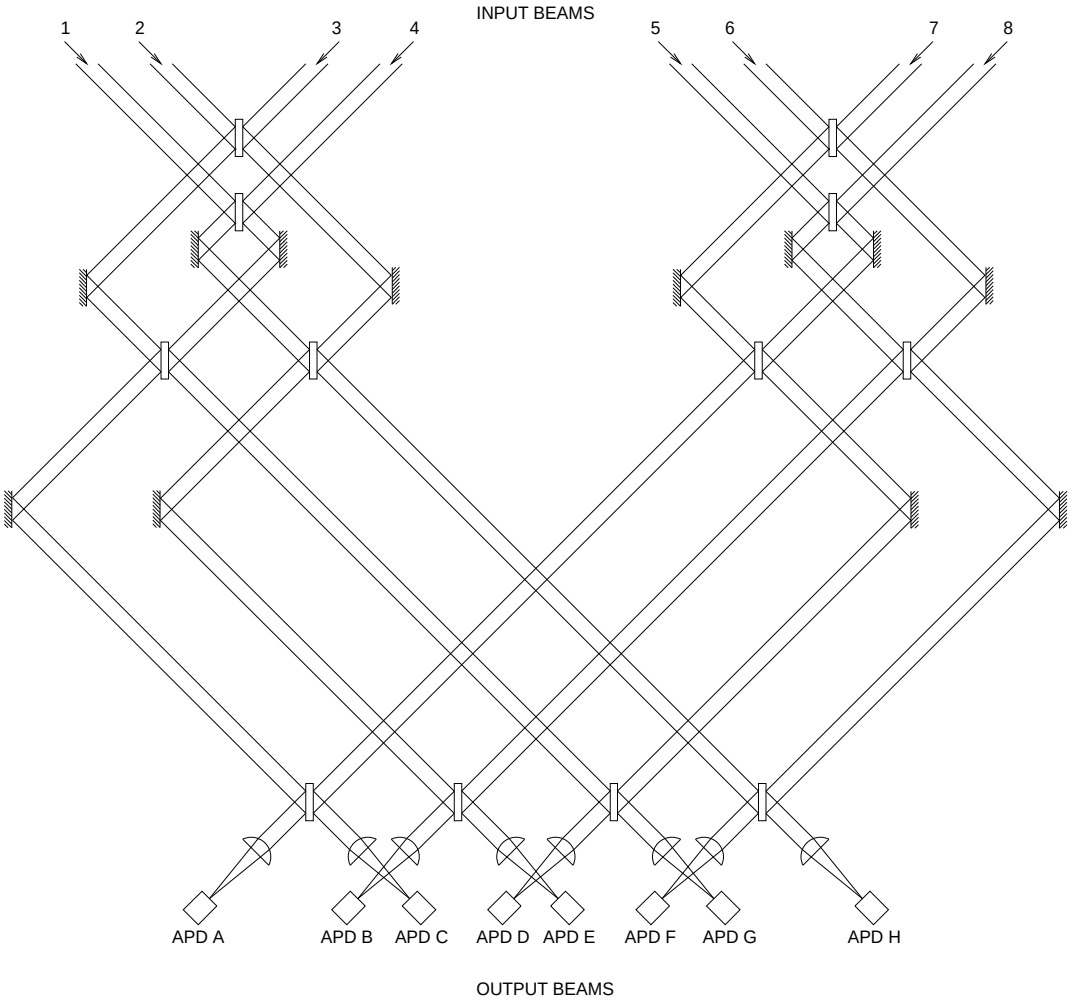

Figure 3.4: A schematic layout of an all beam combination system. This is an extension of the COAST (Buscher 1988) idea. Diagram courtesy of Theo ten Brummelaar.

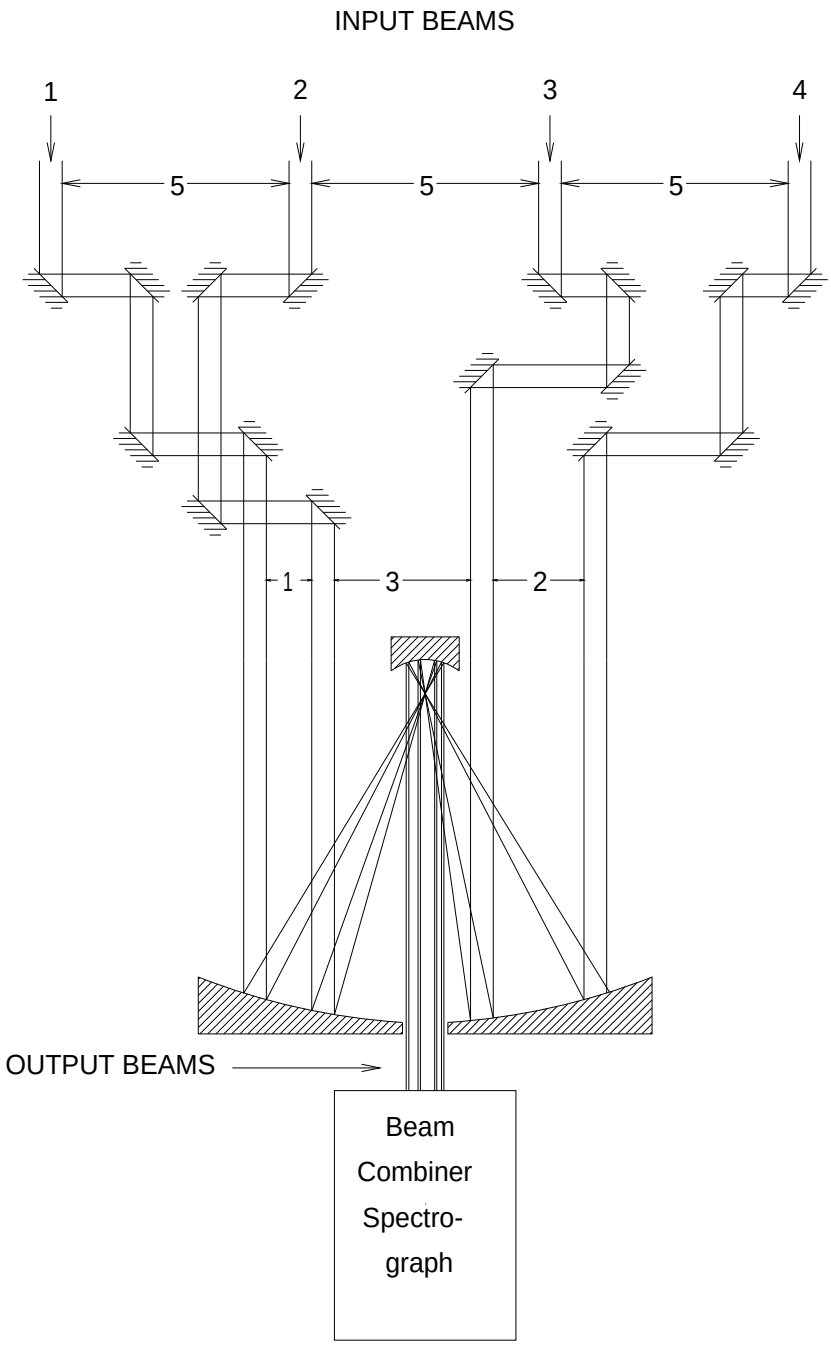

Figure 3.5: A schematic layout of a remapped one-dimensional non-redundant mapping combiner using a large objective. Note the many reflections required. Diagram courtesy of Theo ten Brummelaar.

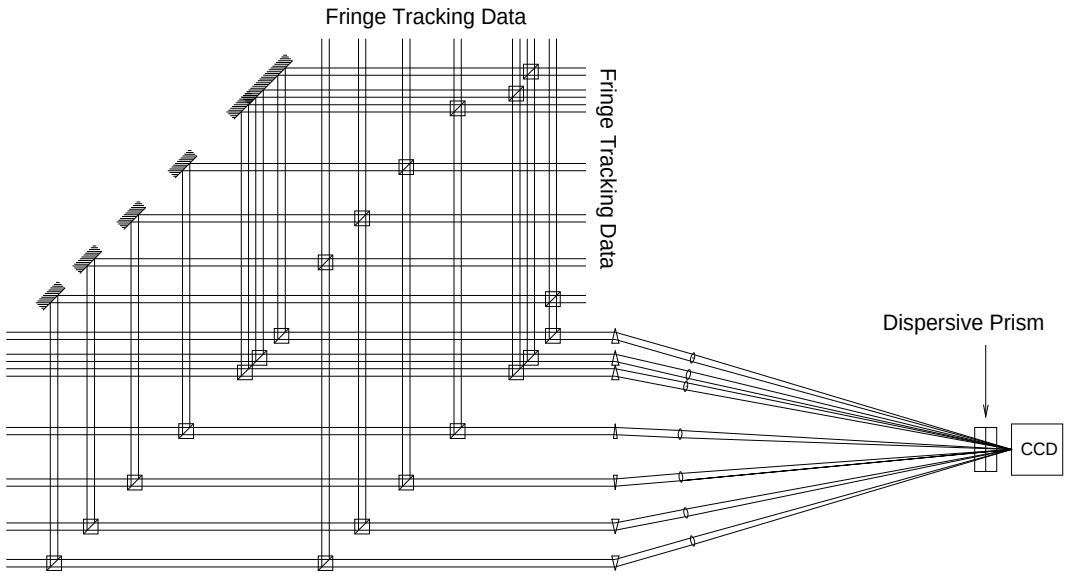

Figure 3.6: A schematic layout of a non-remapped one-dimensional non-redundant array combiner. Diagram courtesy of Theo ten Brummelaar.

would have to be 1.25 m across.

3.4.4 Non-Remapped 1-D Non-Redundant Beam Combiner

Borrowing the fresnel lens concept, one can conceive of a beam combiner that looks something like what is shown in Figure 3.6. Because of the necessity of equalizing path lengths, the curve traced out by the phase centers of each of the beams would not be a straight line and an actual combiner of this design would not be as simple as that shown in Figure 3.6. In addition, it is not at all obvious how a transmission optic would significantly steer a 25 mm beam without dispersing it. For the same reasons given in Section 3.4.1, the imaging and fringe tracking systems would not be in phase simultaneously. For these reasons, this design was not adopted.

3.4.5 Remapped 2-D Non-Redundant Beam Combiner

Readdressing the remapped one-dimensional, non-redundant pattern option with the aim of reducing the size of the imager beam reducer led to a remapped *two*-dimensional, non-redundant pattern, shown in Figure 3.7. The imager beam reducer

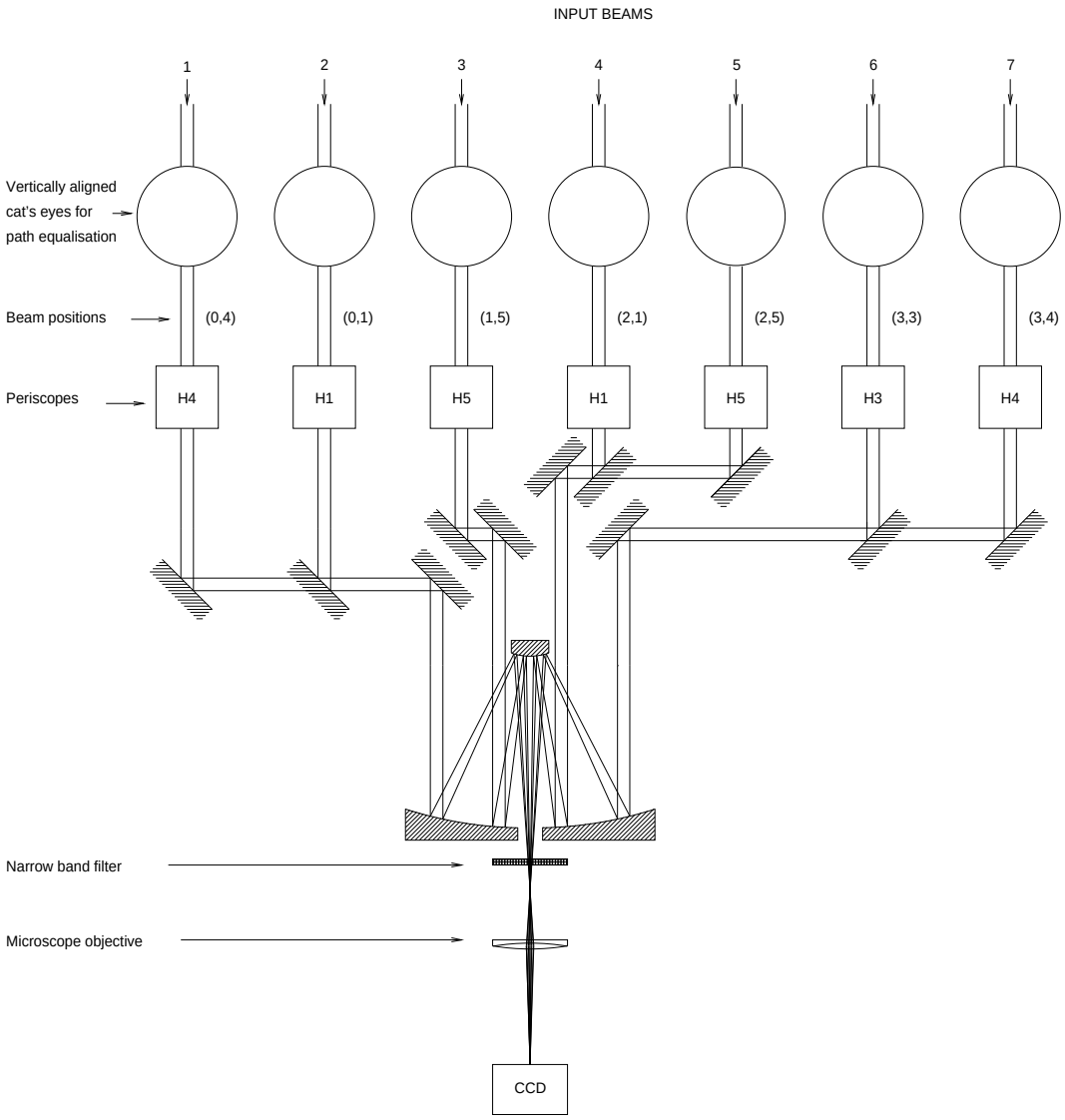

Figure 3.7: A schematic layout of a remapped two-dimensional non-redundant array combiner. Note on the diagram the words "Beam positions". These are the coordinates of the beam location on the objective. The first coordinate is the horizontal coordinate, while the second is a vertical coordinate coming out of the page. The view is looking down, so beams that appear to pass through mirrors are actually at a different level. Diagram courtesy of Theo ten Brummelaar.

primary is reduced to 30 cm from 1.25 m. However, because the pattern is two-dimensional, increasing the bandwidth by dispersion cannot be done. In a manner similar to the single-pixel detector designs, the bandwidth would have to be limited through the use of narrow-band filters. Also, in the process of creating the two-dimensional pattern, care must be taken to insure path length equalizations. As in the case of the design in Figure 3.5, that means more reflections.

3.5 The Fiber Optic Beam Combiner

The design that was eventually decided upon incorporates the ability to gather all baseline visibilities and phase closures simultaneously, is separate from the fringe tracking system (and can be simultaneously in phase with it), has a high bandwidth, has a minimal number of optical surfaces, and is compact. This is done through the judicious use of single-mode fiber optic strands. A schematic is shown in Figure 3.8. In this design, the seven beams from each telescope are launched into single-mode fiber optic strands. The output of each strand is recollimated and rearranged into a non-redundant linear mapping pattern to spatially encode the visibility and raw phase of each baseline. The linear array is then fed through a prism to disperse the light in a direction orthogonal to the linear array spacing. Then the encoded and dispersed light is focused with a long focal length achromat. Prior to coming to a complete focus, a long focal length negative cylindrical element is inserted into the beam. It is oriented with its non-curved axis aligned parallel to the linear array. This is shown in Figure 3.9. To first order, the negative cylindrical element "recollimates" the light, but only in the spectral dimension. A short focal length positive cylindrical element, oriented the same as the negative element, is then inserted into the beam to bring the light to a focus in the spectral dimension. The end effect is to have the spatial frequency dimension (containing the fringe pattern) be brought to a focus with a larger focal length than the spectral dimension. One then gets high magnification along the spatial frequency dimension and low magnification (large spectral coverage) along the spectral dimension. This technique was succesfully demonstrated in the MAPPIT experiment (Bedding et al. 1992).

To test the feasability, a prototype was conceived to test a number of the new elements of the design; coupling efficiency into a single-mode fiber optic strand (Sec-

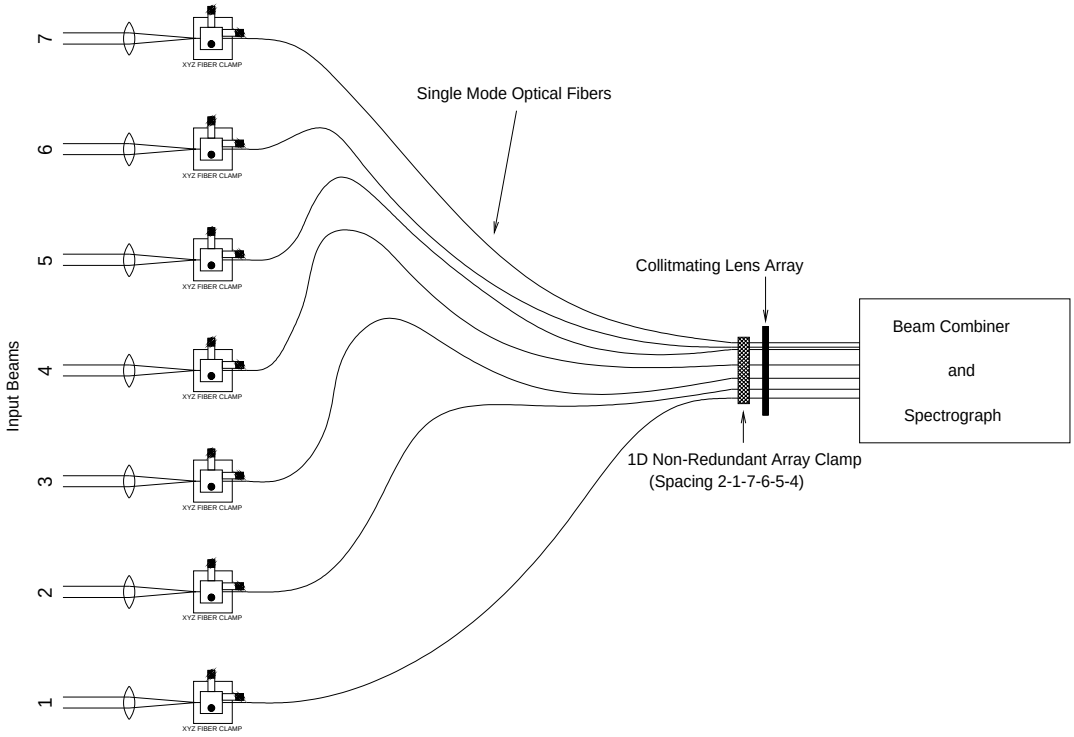

Figure 3.8: A (very) schematic diagram of the proposed CHARA Array imager. Note that in this diagram there are seven telescopes, the number in the original proposal to the National Science Foundation. Note also that fringe tracking (Figure 3.2) is a completely separate system and is *not* displayed here. The instrument built would be scaled back to five. Diagram courtesy of Theo ten Brummelaar.

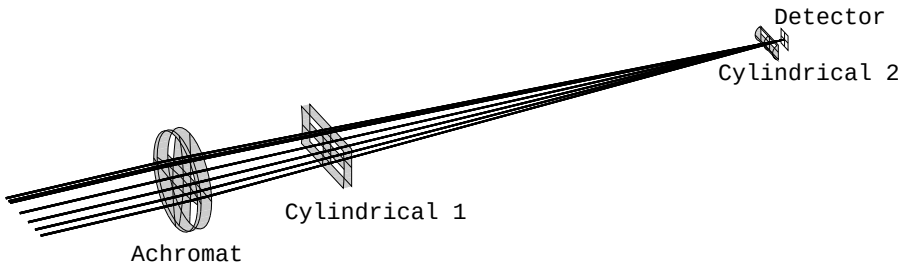

Figure 3.9: An optical ray trace of the Spectrograph Beam Combiner. This was drawn using *Beam 4* (Stellar Software, P.O. Box 10183, Berkeley, California 94709). Diagram courtesy of Theo ten Brummelaar.

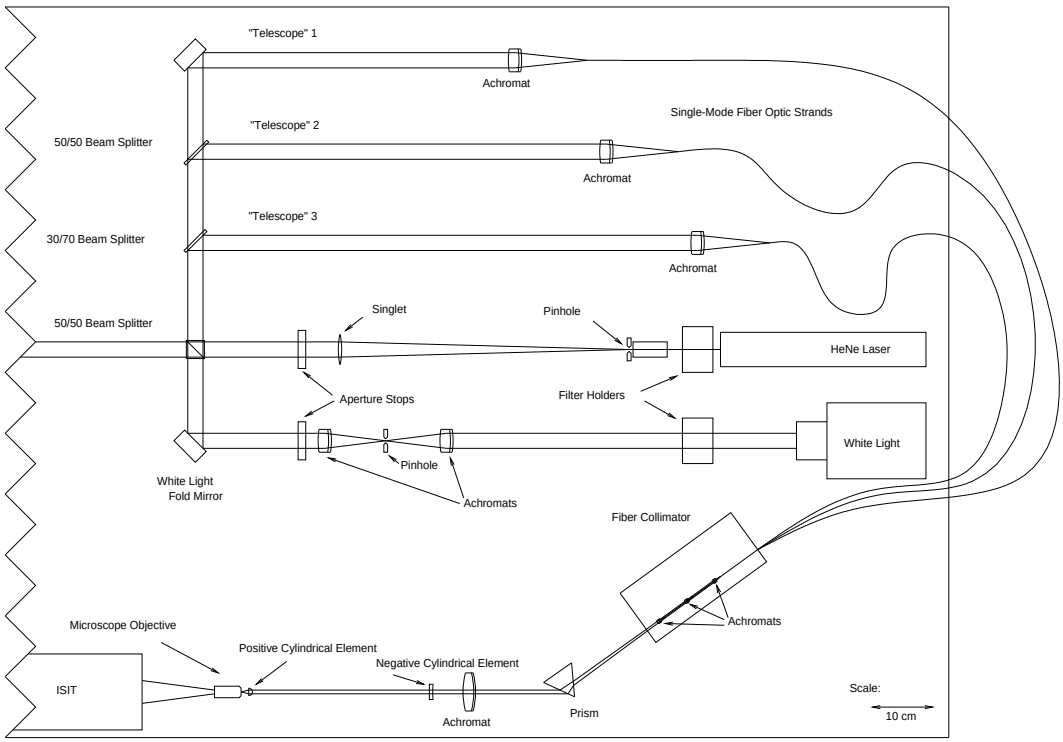

Figure 3.10: This is a schematic diagram of the light sources and optics used for the construction of the prototype imager.

tions 4.3.4 and 6.2), polarization sensitivity and fringe contrast of the strands (Section 6.3.2), and the effects of dispersion due to the different strand lengths (Section 6.5.2). Figure 3.10 shows a dimensionally accurate schematic of the prototype setup used in this dissertation and Figure 3.11 shows a "bird's-eye" view of the prototype systems and light source assemblies.

The prototype imager described in this dissertation is an original concept by Theo ten Brummelaar and is designed and built by the author. Whereas several other groups have built devices incorporating various elements of the prototype, this is the first time, to the author's knowledge, that white light fringes from remapped single-mode fiber optic strands have been detected by simple reimaging. Single-mode fiber groups usually perform the interference within close proximity fiber couplers.

The unique aspect of this prototype is to use single-mode fiber optic strands to

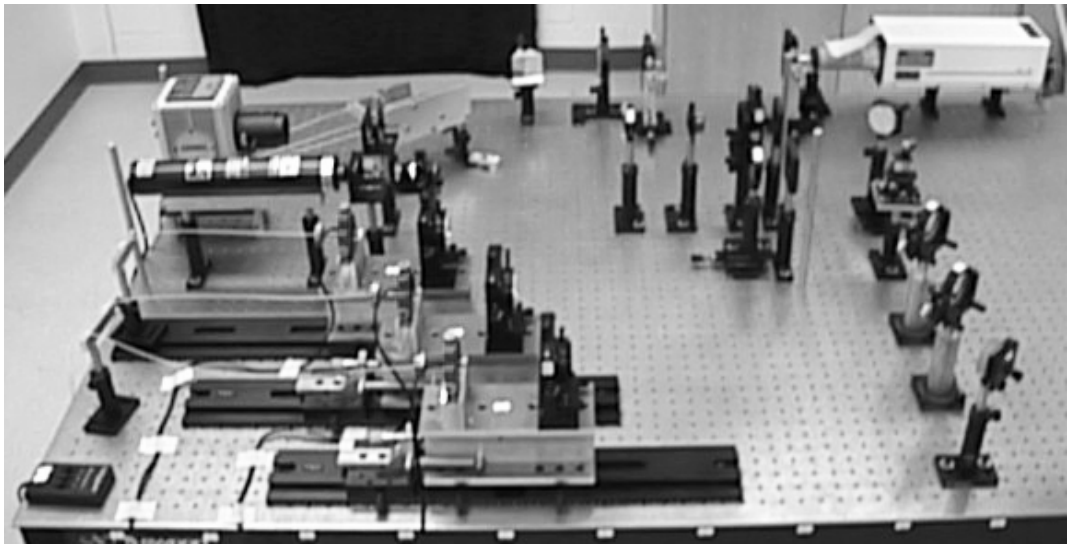

Figure 3.11: This is a bird's-eye view of the prototype imager. A description can be found in Figure 3.10.

replace a potentially complex chain of optics. The difficulty in dealing with the single-mode strands is well worth the gain in simplicity and efficiency.

Chapter 4

Single-Mode Fiber Optical Strands – Theory and Practice

The step-index fiber optic strand is a very long and thin construction of two types of glass and plastic in a concentric cylindrical configuration. It consists of a *core* of one glass type (index of refraction $n_{\rm core}$) embedded within a *cladding* of another glass type (index of refraction $n_{\rm clad}$), surrounded by a sheath made of plastic, teflon, or some similar material to allow the strand to flex without breaking. The *numerical aperture* of the strand is defined as,

$$\text{N.A.} = \sqrt{|n_{\rm clad}^2 - n_{\rm core}^2|}.$$

Step-index fiber optic strands come in two basic varieties, the single-mode strand and the multi-mode strand. The basic geometries are similar, but the single-mode strand has a core size of ~ 3 μm, while that of the multi-mode strand is ~ 100 μm.

Up until recently, fiber optic strands (both single-mode and multi-mode) were mostly the tool of the communications industry professional. Fiber optic strands allow for a streamlined packaging process in astronomical instruments. Multi-mode strands have found a niche in the construction of spectrographs, both single-object (Barry, 1995) and multi-object (Barden et al., 1992). Spectrographs do not require phase preservation and hence multi-mode strands make an ideal choice for wide spectral coverage and high coupling efficiencies (greater than 70%). Multi-mode strands allow the spectrograph to be located in a temperature and vibrationally controlled

environment while the telescope is free to move. So long as the incident cone angle ($2\arctan((2f\text{-ratio})^{-1})$) does not exceed the arcsine of the numerical aperture, the multi-mode strand makes an excellent replacement for a wide variety of traditional beam transfer optics. Should the arcsine of the numerical aperture be exceeded, multi-mode strands can still be used. However, there is a general focal ratio degradation (the output cone angle is larger than the input) in multi-mode strands, and one must design the output transfer optics carefully. Single-mode strands have proved useful in situations where phase preservation is required. Generally, they are used as the communications link between components where high bandpasses are required. Recently, they have come into use in interferometric imagers (Coudé du Foresto and Ridgway, 1992; Coudé du Foresto et al., 1996). Single-mode strands have the feature of filtering all incoming wavefronts to the intrinsic mode of the strand. In the case of the atmospherically aberrated image, the single-mode strand translates the phase variations of the atmosphere, which would degrade interferometer performance, into intensity variations which can be calibrated (Shaklan and Roddier, 1988). In addition, single-mode strands do not exhibit the focal ratio degradation in multi-mode strands. Because the astronomer might not have access to the vast body of research and development published about single-mode strands (often times published in obscure communications industry journals), a derivation of the basic guide equations is included in Section 4.2.

4.1 The Dielectric Waveguide

A single-mode fiber optic strand is a dielectric waveguide. Most students encounter waveguides in the latter stages of courses on electricity and magnetism. In that course, the type of waveguide encountered is usually the hollow, (perfectly) conductive waveguide. Though the physics and mathematics involved are essentially the same, conceptually, there are slight differences. The key difference is the localization of the electric ($\boldsymbol{E}$) and magnetic ($\boldsymbol{H}$) fields and what they imply about the form of the waveguide.

In the conductive waveguide, $\boldsymbol{E}$ and $\boldsymbol{H}$ are completely confined to the interior of the waveguide. This comes about because a perfectly conductive surface is perfectly reflective at all wavelengths of light – the wave does not penetrate the conductor at

all.

In a dielectric waveguide, not all of the energy of the wave passing through the guide is confined to the core (analagous to the hollow part of the conductive waveguide). As a result, a few extra parameters have to be balanced to make the waveguide work. These parameters will be addressed in Section 4.2. To address the core confinement problem, materials with slightly different indices of refraction are used together, the larger index material in the core. Though one could design the core material to use air as the cladding, the resulting device is impractical, as will be discussed in Chapter 5. In practice, $n_{\text{core}} - n_{\text{clad}} \ll 1$. The value of this difference is typically 0.01.

4.2 Waveguide Modes – Cylindrical Geometry

Cylindrical geometry boundary value problems frequently reduce to solving some variant of Bessel's equation. For this reason, an appendix is dedicated to summarizing the basic properties of Bessel's equation. Appendix D collects information on solutions, notation, approximations, and relations of functions encountered in solving Bessel's equation. Appendix D should be read in conjunction with this section.

For the purposes of this derivation, a few simplifications will be made. First, the core of the strand, of radius a and index n_{core}, will be within a cladding, of index n_{clad}, of infinite extent. Since the cladding is actually of finite extent, there are some radiation losses. Their effect is small over distances of the order of meters (Jeunhomme 1983, Section 3.3). The second simplification centers the strand on the z-axis. The strand is flexible, and will in general not always lie along a preferred axis. Bending introduces *birefringence*, a changing of the polarization properties of the guided wave along two orthogonal axes, which, in general, also leads to losses. This effect will be discussed in Section 4.3. The procedure in solving for the guided modes follows Marcuse (1982) using the notation of Wangsness (1986).

4.2.1 Setting Up the Problem

As stated above, the geometry is of a material of index n_{core}, of radius a, centered on the z-axis, completely embedded within a material of index n_{clad}. An electromagnetic

wave is travelling within this construct in the positive z-axis direction (getting into this construct will be discussed in Section 4.3).

The components of the wave take the following form,

$$\begin{aligned} \boldsymbol{E} &= \boldsymbol{\mathcal{E}}(\rho,\phi)e^{i(k_g z-\omega t)} \\ &= \Big[\mathcal{E}_\rho(\rho,\phi)\hat{\boldsymbol{\rho}} + \mathcal{E}_\phi(\rho,\phi)\hat{\boldsymbol{\phi}} + \mathcal{E}_z(\rho,\phi)\hat{\boldsymbol{z}}\Big]e^{i(k_g z-\omega t)} \end{aligned} \tag{4.1}$$

and

$$\begin{aligned} \boldsymbol{H} &= \boldsymbol{\mathcal{H}}(\rho,\phi)e^{i(k_g z-\omega t)} \\ &= \Big[\mathcal{H}_\rho(\rho,\phi)\hat{\boldsymbol{\rho}} + \mathcal{H}_\phi(\rho,\phi)\hat{\boldsymbol{\phi}} + \mathcal{H}_z(\rho,\phi)\hat{\boldsymbol{z}}\Big]e^{i(k_g z-\omega t)}, \end{aligned} \tag{4.2}$$

where bold face symbols represent vector quantities, $\hat{\boldsymbol{\rho}}$, $\hat{\boldsymbol{\phi}}$, and $\hat{\boldsymbol{z}}$ are the unit vectors in cylindrical coordinates, and $k_g = \frac{2\pi}{\lambda_g}$, λ_g being the wavelength of the propagated mode.

4.2.2 Maxwell Equations

The materials involved in the waveguide are linear, isotropic and homogeneous. There are no free charges or currents, the permeability is that of free space for both media ($\mu_{\text{core}} = \mu_{\text{clad}} = \mu_0$). For this situation, the Maxwell equations become

$$\boldsymbol{\nabla}\cdot\boldsymbol{E} = 0, \tag{4.3}$$

$$\boldsymbol{\nabla}\cdot\boldsymbol{H} = 0, \tag{4.4}$$

$$\boldsymbol{\nabla}\times\boldsymbol{E} = -\mu_0\frac{\partial\boldsymbol{H}}{\partial t}, \tag{4.5}$$

and

$$\boldsymbol{\nabla}\times\boldsymbol{H} = n^2\epsilon_0\frac{\partial\boldsymbol{E}}{\partial t}, \tag{4.6}$$

where n is either n_{core} or n_{clad}. Equations 4.3–4.6 are subject to the following boundary conditions (at the boundary, $\rho = a$)

$$(E_\phi)_{\text{core}} = (E_\phi)_{\text{clad}} \tag{4.7}$$

$$(E_z)_{\text{core}} = (E_z)_{\text{clad}} \tag{4.8}$$

$$(H_\phi)_{\text{core}} = (H_\phi)_{\text{clad}} \tag{4.9}$$

$$(H_z)_{\text{core}} = (H_z)_{\text{clad}}. \tag{4.10}$$

4.2.3 The Scalar Equations

If $\boldsymbol{F}$ is a vector field function, the divergence and curl in cylindrical coordinates are given as

$$\boldsymbol{\nabla} \cdot \boldsymbol{F} = \frac{1}{\rho}\frac{\partial}{\partial\rho}\Big(\rho F_\rho\Big) + \frac{1}{\rho}\frac{\partial F_\phi}{\partial\phi} + \frac{\partial F_z}{\partial z} \tag{4.11}$$

$$\boldsymbol{\nabla} \times \boldsymbol{F} = \left[\frac{1}{\rho}\frac{\partial F_z}{\partial\phi} - \frac{\partial F_\phi}{\partial z}\right]\hat{\boldsymbol{\rho}} + \left[\frac{\partial F_\rho}{\partial z} - \frac{\partial F_z}{\partial\rho}\right]\hat{\boldsymbol{\phi}} + \left[\frac{1}{\rho}\frac{\partial}{\partial\rho}\Big(\rho F_\phi\Big) - \frac{1}{\rho}\frac{\partial F_\rho}{\partial\phi}\right]\hat{\boldsymbol{z}}. \tag{4.12}$$

By use of equations 4.1, 4.2, 4.11, and 4.12, equations 4.3–4.6 generate the following equations

$$\frac{1}{\rho}\mathcal{E}_\rho + \frac{\partial\mathcal{E}_\rho}{\partial\rho} + \frac{1}{\rho}\frac{\partial\mathcal{E}_\phi}{\partial\phi} + ik_g\mathcal{E}_z = 0, \tag{4.13}$$

$$\frac{1}{\rho}\mathcal{H}_\rho + \frac{\partial\mathcal{H}_\rho}{\partial\rho} + \frac{1}{\rho}\frac{\partial\mathcal{H}_\phi}{\partial\phi} + ik_g\mathcal{H}_z = 0, \tag{4.14}$$

$$\frac{1}{\rho}\frac{\partial\mathcal{E}_z}{\partial\phi} - ik_g\mathcal{E}_\phi = i\omega\mu_0\mathcal{H}_\rho, \tag{4.15}$$

$$ik_g\mathcal{E}_\rho - \frac{\partial \mathcal{E}_z}{\partial \rho} = i\omega\mu_0\mathcal{H}_\phi, \tag{4.16}$$

$$\frac{1}{\rho}\mathcal{E}_\phi + \frac{\partial \mathcal{E}_\phi}{\partial \rho} - \frac{1}{\rho}\frac{\partial \mathcal{E}_\rho}{\partial \phi} = i\omega\mu_0\mathcal{H}_z, \tag{4.17}$$

$$\frac{1}{\rho}\frac{\partial \mathcal{H}_z}{\partial \phi} - ik_g\mathcal{H}_\phi = -i\omega n^2\epsilon_0\mathcal{E}_\rho, \tag{4.18}$$

$$ik_g\mathcal{H}_\rho - \frac{\partial \mathcal{H}_z}{\partial \rho} = -i\omega n^2\epsilon_0\mathcal{E}_\phi, \tag{4.19}$$

and

$$\frac{1}{\rho}\mathcal{H}_\phi + \frac{\partial \mathcal{H}_\phi}{\partial \rho} - \frac{1}{\rho}\frac{\partial \mathcal{H}_\rho}{\partial \phi} = -i\omega n^2\epsilon_0\mathcal{E}_z. \tag{4.20}$$

There are eight equations because equations 4.5 and 4.6 each produce three scalar equations, one for each coordinate. These six scalar equations, along with equations 4.3 and 4.4, add up to eight.

At this point, one notes that equations 4.15 and 4.19 involve only the quantities $\mathcal{H}_\rho$, $\mathcal{E}_\phi$, $\mathcal{E}_z$, and $\mathcal{H}_z$, while equations 4.16 and 4.18 involve only the quantities $\mathcal{H}_\phi$, $\mathcal{E}_\rho$, $\mathcal{E}_z$, and $\mathcal{H}_z$. Piecing this information together, one gets

$$\mathcal{E}_\rho = -\frac{i}{\kappa^2}\Big(k_g\frac{\partial \mathcal{E}_z}{\partial \rho} + \omega\mu_0\frac{1}{\rho}\frac{\partial \mathcal{H}_z}{\partial \phi}\Big), \tag{4.21}$$

$$\mathcal{E}_\phi = -\frac{i}{\kappa^2}\Big(k_g\frac{1}{\rho}\frac{\partial \mathcal{E}_z}{\partial \phi} - \omega\mu_0\frac{\partial \mathcal{H}_z}{\partial \rho}\Big), \tag{4.22}$$

$$\mathcal{H}_\rho = -\frac{i}{\kappa^2}\Big(k_g\frac{\partial \mathcal{H}_z}{\partial \rho} - \omega n^2\epsilon_0\frac{1}{\rho}\frac{\partial \mathcal{E}_z}{\partial \phi}\Big), \tag{4.23}$$

and

$$\mathcal{H}_\phi = -\frac{i}{\kappa^2}\Big(k_g \frac{1}{\rho}\frac{\partial \mathcal{H}_z}{\partial \phi} + \omega n^2 \epsilon_0 \frac{\partial \mathcal{E}_z}{\partial \rho}\Big), \tag{4.24}$$

where

$$\kappa^2 = k_g^2 - \omega^2 n^2 \epsilon_0 \mu_0.$$

Equations 4.21, 4.22, and 4.17 combine to give

$$\frac{\partial^2 \mathcal{H}_z}{\partial \rho^2} + \frac{1}{\rho}\frac{\partial \mathcal{H}_z}{\partial \rho} + \frac{1}{\rho^2}\frac{\partial^2 \mathcal{H}_z}{\partial \phi^2} + \kappa^2 \mathcal{H}_z = 0, \tag{4.25}$$

while equations 4.23, 4.24, and 4.20 combine to give

$$\frac{\partial^2 \mathcal{E}_z}{\partial \rho^2} + \frac{1}{\rho}\frac{\partial \mathcal{E}_z}{\partial \rho} + \frac{1}{\rho^2}\frac{\partial^2 \mathcal{E}_z}{\partial \phi^2} + \kappa^2 \mathcal{E}_z = 0. \tag{4.26}$$

Trial solutions of

$$\mathcal{E}_z = AR(\rho)e^{i\nu\phi}$$

and

$$\mathcal{H}_z = BR(\rho)e^{i\nu\phi}$$

for equations 4.26 and 4.25, respectively, both yield

$$\rho^2 \frac{d^2 R}{d\rho^2} + \rho \frac{dR}{d\rho} + (\kappa^2 \rho^2 - \nu^2)R = 0. \tag{4.27}$$

By making a change of variable, $x = \kappa\rho$, equation 4.27 becomes

$$x^2 \frac{d^2 R}{dx^2} + x \frac{dR}{dx} + (x^2 - \nu^2)R = 0. \tag{4.28}$$

4.2.4 Differential Equation Solution

Note that equation 4.28 has the same form as equation D.1, Bessel's equation. Which one of the two linearly independent solutions that dominates will depend on the physical constraints of the problem, the wave energy tightly confined to the core with exponential decay as $\rho \to \infty$. With this in mind, J_ν describes the wave behavior best within the core (Appendix D). In the cladding, exponential decay can be had for imaginary values of κ and $H_\nu^{(1)}$. To make this imaginary property explicit, let

$$\kappa = i\xi.$$

From equations 4.26, 4.25, 4.21, 4.22, 4.23, and 4.24, the components of the solution inside the core become

$$\mathcal{E}_z = AJ_\nu(\kappa\rho)e^{i\nu\phi}, \tag{4.29}$$

$$\mathcal{H}_z = BJ_\nu(\kappa\rho)e^{i\nu\phi}, \tag{4.30}$$

$$\mathcal{E}_\rho = -\frac{i}{\kappa^2}\left[k_g\kappa AJ'_\nu(\kappa\rho) + i\omega\mu_0\frac{\nu}{\rho}BJ_\nu(\kappa\rho)\right]e^{i\nu\phi}, \tag{4.31}$$

$$\mathcal{E}_\phi = -\frac{i}{\kappa^2}\left[ik_g\frac{\nu}{\rho}AJ_\nu(\kappa\rho) - \kappa\omega\mu_0 BJ'_\nu(\kappa\rho)\right]e^{i\nu\phi}, \tag{4.32}$$

$$\mathcal{H}_\rho = -\frac{i}{\kappa^2}\left[-i\omega n_{\text{core}}^2\epsilon_0\frac{\nu}{\rho}AJ_\nu(\kappa\rho) + k_g\kappa BJ'_\nu(\kappa\rho)\right]e^{i\nu\phi}, \tag{4.33}$$

and

$$\mathcal{H}_\phi = -\frac{i}{\kappa^2}\left[\kappa\omega n_{\text{core}}^2\epsilon_0 AJ'_\nu(\kappa\rho) + ik_g\frac{\nu}{\rho}BJ_\nu(\kappa\rho)\right]e^{i\nu\phi}, \tag{4.34}$$

where κ is now defined by

$$\kappa^2 = k_g^2 - \omega^2 n_{\text{core}}^2 \epsilon_0 \mu_0.$$

In a similar manner, the components of the solution in the cladding become

$$\mathcal{E}_z = C H_\nu^{(1)}(i\xi\rho) e^{i\nu\phi}, \tag{4.35}$$

$$\mathcal{H}_z = D H_\nu^{(1)}(i\xi\rho) e^{i\nu\phi}, \tag{4.36}$$

$$\mathcal{E}_\rho = -\frac{1}{\xi^2}\Big[k_g \xi C H_\nu^{(1)'}(i\xi\rho) + \omega\mu_0 \frac{\nu}{\rho} D H_\nu^{(1)}(i\xi\rho)\Big] e^{i\nu\phi}, \tag{4.37}$$

$$\mathcal{E}_\phi = -\frac{1}{\xi^2}\Big[k_g \frac{\nu}{\rho} C H_\nu^{(1)}(i\xi\rho) - \xi\omega\mu_0 D H_\nu^{(1)'}(i\xi\rho)\Big] e^{i\nu\phi}, \tag{4.38}$$

$$\mathcal{H}_\rho = -\frac{1}{\xi^2}\Big[-\omega n_{\text{clad}}^2 \epsilon_0 \frac{\nu}{\rho} C H_\nu^{(1)}(i\xi\rho) + k_g \xi D H_\nu^{(1)'}(i\xi\rho)\Big] e^{i\nu\phi}, \tag{4.39}$$

and

$$\mathcal{H}_\phi = -\frac{1}{\xi^2}\Big[\xi\omega n_{\text{clad}}^2 \epsilon_0 C H_\nu^{(1)'}(i\xi\rho) + k_g \frac{\nu}{\rho} D H_\nu^{(1)}(i\xi\rho)\Big] e^{i\nu\phi}, \tag{4.40}$$

where ξ is now defined by

$$\xi^2 = \omega^2 n_{\text{clad}}^2 \epsilon_0 \mu_0 - k_g^2.$$

4.2.5 The Eigenvalue Equation

The boundary conditions at $\rho = a$, equations 4.7–4.10, applied to equations 4.29, 4.30, 4.32, 4.34, 4.35, 4.36, 4.38, and 4.40 generate a set of four homogeneous equations, and five unknowns, A, B, C, D, and k_g. According to principles of linear algebra, for there to be a solution at all, the determinant of the equation set must be zero. This is enough information to determine the value(s) of k_g, the allowed modes of propagation.

In this analysis, the interest is in the allowable modes. As a result, the coefficients will not be determined; their effect is included implicitly in the determinant of the homogeneous equation set,

$$\begin{vmatrix} J_\nu(\kappa a) & 0 & -H_\nu^{(1)}(i\xi a) & 0 \\ \frac{k_g}{\kappa^2}\frac{\nu}{a}J_\nu(\kappa a) & \frac{i\omega\mu_0}{\kappa}J_\nu'(\kappa a) & \frac{k_g}{\xi^2}\frac{\nu}{a}H_\nu^{(1)}(i\xi a) & -\frac{\omega\mu_0}{\xi}H_\nu^{(1)'}(i\xi a) \\ 0 & J_\nu(\kappa a) & 0 & -H_\nu^{(1)}(i\xi a) \\ -\frac{i\omega n_{\text{core}}^2\epsilon_0}{\kappa}J_\nu'(\kappa a) & \frac{k_g}{\kappa^2}\frac{\nu}{a}J_\nu(\kappa a) & \frac{\omega n_{\text{clad}}^2\epsilon_0}{\xi}H_\nu^{(1)'}(i\xi a) & \frac{k_g}{\xi^2}\frac{\nu}{a}H_\nu^{(1)}(i\xi a) \end{vmatrix} = 0.$$

This simplifies to

$$\left[\frac{n_{\text{core}}^2}{n_{\text{clad}}^2}\frac{a\xi^2}{\kappa}\frac{J_\nu'(\kappa a)}{J_\nu(\kappa a)} + i\xi a\frac{H_\nu^{(1)'}(i\xi a)}{H_\nu^{(1)}(i\xi a)}\right]\left[\frac{a\xi^2}{\kappa}\frac{J_\nu'(\kappa a)}{J_\nu(\kappa a)} + i\xi a\frac{H_\nu^{(1)'}(i\xi a)}{H_\nu^{(1)}(i\xi a)}\right] = \left[\nu\left(\frac{n_{\text{core}}^2}{n_{\text{clad}}^2} - 1\right)\frac{k_g\omega^2 n_{\text{clad}}^2}{\kappa^2 c}\right]^2. \quad (4.41)$$

$H_\nu^{(1)}$ was chosen to describe the field behavior in the cladding because of its behavior at large argument values,

$$H_\nu^{(1)}(i\xi\rho) \propto e^{-\xi\rho}. \quad (4.42)$$

If this relation does not hold in the cladding, the energy is radiated away and the mode is no longer guided. The functional form of equation 4.42 hints at some kind of transition when $\xi = 0$. At $\xi = 0$, the waveguide encounters a cutoff condition for a particular mode, which is given as

$$\begin{aligned} k_g &= \omega n_{\text{clad}}\sqrt{\epsilon_0\mu_0} \\ &= \frac{\omega n_{\text{clad}}}{c} \\ k_c &= \frac{\omega_c n_{\text{clad}}}{c}. \end{aligned} \quad (4.43)$$

Solutions of the eigenvalue equation (equation 4.41) at the cutoff point can be ob-

tained more easily through several changes of variable. Let

$$J_\nu^+ = \frac{1}{\kappa a}\frac{J_{\nu+1}(\kappa a)}{J_\nu(\kappa a)}, \tag{4.44}$$

$$J_\nu^- = \frac{1}{\kappa a}\frac{J_{\nu-1}(\kappa a)}{J_\nu(\kappa a)}, \tag{4.45}$$

$$H_\nu^+ = \frac{1}{i\xi a}\frac{H_{\nu+1}^{(1)}(i\xi a)}{H_\nu^{(1)}(i\xi a)}, \tag{4.46}$$

and

$$H_\nu^- = \frac{1}{i\xi a}\frac{H_{\nu-1}^{(1)}(i\xi a)}{H_\nu^{(1)}(i\xi a)}. \tag{4.47}$$

Equation 4.41, through the use of equations 4.44–4.47 and D.23, becomes

$$\left[\frac{n_{\text{core}}^2}{n_{\text{clad}}^2}\left(J_\nu^- - J_\nu^+\right) - \left(H_\nu^- - H_\nu^+\right)\right]\left[\left(J_\nu^- - J_\nu^+\right) - \left(H_\nu^- - H_\nu^+\right)\right] = \left[2\nu\left(\frac{n_{\text{core}}^2}{n_{\text{clad}}^2} - 1\right)\frac{k_g\omega^2 n_{\text{clad}}^2}{a^2\xi^2\kappa^2 c}\right]^2. \tag{4.48}$$

The lefthand side of equation 4.48 can be rearranged as follows,

$$\begin{aligned}
\mathrm{LHS}_{\text{Eq. 4.48}} &= \left[\frac{n_{\text{core}}^2}{n_{\text{clad}}^2}\Big(J_\nu^- - J_\nu^+\Big) - \Big(H_\nu^- - H_\nu^+\Big)\right]\left[\Big(J_\nu^- - J_\nu^+\Big) - \Big(H_\nu^- - H_\nu^+\Big)\right] \\
&= \left[\Big(\frac{n_{\text{core}}^2}{n_{\text{clad}}^2}J_\nu^- - H_\nu^-\Big) - \Big(\frac{n_{\text{core}}^2}{n_{\text{clad}}^2}J_\nu^+ - H_\nu^+\Big)\right]\left[\Big(J_\nu^- - H_\nu^-\Big) - \Big(J_\nu^+ - H_\nu^+\Big)\right] \\
&= \Big(\frac{n_{\text{core}}^2}{n_{\text{clad}}^2}J_\nu^- - H_\nu^-\Big)\Big(J_\nu^- - H_\nu^-\Big) - \Big(\frac{n_{\text{core}}^2}{n_{\text{clad}}^2}J_\nu^- - H_\nu^-\Big)\Big(J_\nu^+ - H_\nu^+\Big) \\
&\quad - \Big(\frac{n_{\text{core}}^2}{n_{\text{clad}}^2}J_\nu^+ - H_\nu^+\Big)\Big(J_\nu^- - H_\nu^-\Big) + \Big(\frac{n_{\text{core}}^2}{n_{\text{clad}}^2}J_\nu^+ - H_\nu^+\Big)\Big(J_\nu^+ - H_\nu^+\Big) \\
&= -2\Big(\frac{n_{\text{core}}^2}{n_{\text{clad}}^2}J_\nu^- - H_\nu^-\Big)\Big(J_\nu^+ - H_\nu^+\Big) - 2\Big(\frac{n_{\text{core}}^2}{n_{\text{clad}}^2}J_\nu^+ - H_\nu^+\Big)\Big(J_\nu^- - H_\nu^-\Big) \\
&\quad + \Big(\frac{n_{\text{core}}^2}{n_{\text{clad}}^2}J_\nu^- - H_\nu^-\Big)\Big(J_\nu^- - H_\nu^-\Big) + \Big(\frac{n_{\text{core}}^2}{n_{\text{clad}}^2}J_\nu^- - H_\nu^-\Big)\Big(J_\nu^+ - H_\nu^+\Big) \\
&\quad - \Big(\frac{n_{\text{core}}^2}{n_{\text{clad}}^2}J_\nu^+ - H_\nu^+\Big)\Big(J_\nu^- - H_\nu^-\Big) + \Big(\frac{n_{\text{core}}^2}{n_{\text{clad}}^2}J_\nu^+ - H_\nu^+\Big)\Big(J_\nu^+ - H_\nu^+\Big) \\
&= -2\Big(\frac{n_{\text{core}}^2}{n_{\text{clad}}^2}J_\nu^- - H_\nu^-\Big)\Big(J_\nu^+ - H_\nu^+\Big) - 2\Big(\frac{n_{\text{core}}^2}{n_{\text{clad}}^2}J_\nu^+ - H_\nu^+\Big)\Big(J_\nu^- - H_\nu^-\Big) \\
&\quad + \left[\frac{n_{\text{core}}^2}{n_{\text{clad}}^2}\Big(J_\nu^+ + J_\nu^-\Big) - \Big(H_\nu^+ + H_\nu^-\Big)\right]\left[\Big(J_\nu^+ + J_\nu^-\Big) - \Big(H_\nu^+ + H_\nu^-\Big)\right].
\end{aligned} \tag{4.49}$$

Through the use of equation D.24, the terms in square brackets in equation 4.49 become

$$\begin{aligned}
&\left[\frac{n_{\text{core}}^2}{n_{\text{clad}}^2}\Big(J_\nu^+ + J_\nu^-\Big) - \Big(H_\nu^+ + H_\nu^-\Big)\right]\left[\Big(J_\nu^+ + J_\nu^-\Big) - \Big(H_\nu^+ + H_\nu^-\Big)\right] \\
&\qquad = \left[\frac{n_{\text{core}}^2}{n_{\text{clad}}^2}\Big(\frac{2\nu}{\kappa^2 a^2}\Big) - \Big(-\frac{2\nu}{\xi^2 a^2}\Big)\right]\left[\Big(\frac{2\nu}{\kappa^2 a^2}\Big) - \Big(-\frac{2\nu}{\xi^2 a^2}\Big)\right] \\
&\qquad = \Big(\frac{2\nu}{a^2\kappa^2\xi^2}\Big)^2\Big(\frac{n_{\text{core}}^2}{n_{\text{clad}}^2}\xi^2 + \kappa^2\Big)\Big(\xi^2 + \kappa^2\Big) \\
&\qquad = \Big(\frac{2\nu}{a^2\kappa^2\xi^2}\Big)^2\Big(-\frac{n_{\text{core}}^2}{n_{\text{clad}}^2}k_g^2 + k_g^2\Big)\Big(\omega^2\epsilon_0\mu_0(n_{\text{clad}}^2 - n_{\text{core}}^2)\Big) \\
&\qquad = \Big(\frac{2\nu}{a^2\kappa^2\xi^2}\Big)^2\Big(\frac{k_g\omega n_{\text{clad}}}{c}\Big)^2\Big(\frac{n_{\text{core}}^2}{n_{\text{clad}}^2} - 1\Big)^2.
\end{aligned} \tag{4.50}$$

Combining equations 4.48, 4.49, and 4.50, equation 4.41 becomes

$$\left(\frac{n_{\text{core}}^2}{n_{\text{clad}}^2}J_\nu^- - H_\nu^-\right)\left(J_\nu^+ - H_\nu^+\right) + \left(\frac{n_{\text{core}}^2}{n_{\text{clad}}^2}J_\nu^+ - H_\nu^+\right)\left(J_\nu^- - H_\nu^-\right) = 0. \tag{4.51}$$

4.2.6 Cutoff Solutions

Finding the solutions at cutoff involves determining the functional form of equation 4.51 near $\xi = 0$. First of all, consider the case of $\nu = 0$. In this case, equation 4.48 simplifies to

$$\left[\frac{n_{\text{core}}^2}{n_{\text{clad}}^2}\left(J_0^- - J_0^+\right) - \left(H_0^- - H_0^+\right)\right]\left[\left(J_0^- - J_0^+\right) - \left(H_0^- - H_0^+\right)\right] = 0. \tag{4.52}$$

Equation 4.52 holds true if one of two possible conditions occurs,

$$\begin{aligned}\frac{n_{\text{core}}^2}{n_{\text{clad}}^2}\left(J_0^- - J_0^+\right) - \left(H_0^- - H_0^+\right) &= \frac{n_{\text{core}}^2}{n_{\text{clad}}^2}\frac{\xi}{\kappa}\frac{J_1(\kappa a)}{J_0(\kappa a)} + i\frac{H_1^{(1)}(i\xi a)}{H_0^{(1)}(i\xi a)} \\ &= 0,\end{aligned} \tag{4.53}$$

or

$$\begin{aligned}\left(J_0^- - J_0^+\right) - \left(H_0^- - H_0^+\right) &= \frac{\xi}{\kappa}\frac{J_1(\kappa a)}{J_0(\kappa a)} + i\frac{H_1^{(1)}(i\xi a)}{H_0^{(1)}(i\xi a)} \\ &= 0.\end{aligned} \tag{4.54}$$

Allowing $\xi \to 0$ in the argument of $H_\nu^{(1)}(i\xi a)$, equation 4.53, through the use of equation D.16, becomes

$$\begin{aligned}
\frac{n_{\text{core}}^2}{n_{\text{clad}}^2}\frac{\xi}{\kappa}\frac{J_1(\kappa a)}{J_0(\kappa a)} + i\frac{-\frac{i}{\pi}\left(\frac{2}{i\xi a}\right)}{1+\frac{2i}{\pi}\ln\frac{e^\gamma i\xi a}{2}} &= 0 \\
\frac{n_{\text{core}}^2}{n_{\text{clad}}^2}\frac{\xi}{\kappa}\frac{J_1(\kappa a)}{J_0(\kappa a)} &= -i\frac{-\frac{2}{\pi\xi a}}{\frac{2i}{\pi}\ln\frac{e^\gamma\xi a}{2}} \\
&= \frac{1}{\xi a\ln\frac{e^\gamma\xi a}{2}} \\
\frac{n_{\text{clad}}^2}{n_{\text{core}}^2}\frac{J_0(\kappa a)}{J_1(\kappa a)} &= -\frac{\xi^2 a}{\kappa}\ln\frac{2}{e^\gamma\xi a}.
\end{aligned} \tag{4.55}$$

Equation 4.55 was simplified through the use of

$$\ln(i) = \frac{\pi}{2}i.$$

In the right hand side of equation 4.55, as $\xi \to 0$, the ξ^2 factor wins out over the $\frac{1}{\xi}$ in the logarithm causing that side to vanish. This can only happen if

$$J_0(\kappa a) = 0. \tag{4.56}$$

Upon inspection, it can be easily seen that equation 4.56 describes the cutoff condition of equation 4.54 as well.

Next, consider the case of $\nu = 1$. From equation D.16,

$$\lim_{\xi\to 0} H_1^+ = -\frac{2}{\xi^2 a^2}$$

and

$$\lim_{\xi\to 0} H_1^- = -\ln\frac{e^\gamma\xi a}{2}.$$

Equation 4.51 now becomes

$$\Big(\frac{n_{\text{core}}^2}{n_{\text{clad}}^2}\frac{1}{\kappa a}\frac{J_0(\kappa a)}{J_1(\kappa a)}+\ln\frac{e^\gamma\xi a}{2}\Big)\Big(\frac{1}{\kappa a}\frac{J_2(\kappa a)}{J_1(\kappa a)}+\frac{2}{\xi^2a^2}\Big) + \Big(\frac{n_{\text{core}}^2}{n_{\text{clad}}^2}\frac{1}{\kappa a}\frac{J_2(\kappa a)}{J_1(\kappa a)}+\frac{2}{\xi^2a^2}\Big)\Big(\frac{1}{\kappa a}\frac{J_0(\kappa a)}{J_1(\kappa a)}+\ln\frac{e^\gamma\xi a}{2}\Big)=0$$

and

$$\Big(\frac{n_{\text{core}}^2}{n_{\text{clad}}^2}J_0(\kappa a)+\kappa a\ln\frac{e^\gamma\xi a}{2}J_1(\kappa a)\Big)\Big(\xi^2a^2J_2(\kappa a)+2\kappa aJ_1(\kappa a)\Big) + \Big(\frac{n_{\text{core}}^2}{n_{\text{clad}}^2}\xi^2a^2J_2(\kappa a)+2\kappa aJ_1(\kappa a)\Big)\Big(J_0(\kappa a)+\kappa a\ln\frac{e^\gamma\xi a}{2}J_1(\kappa a)\Big)=0.$$

At this point, one can drop terms including simple powers of ξ, they will vanish as $\xi\to 0$; and

$$2\kappa aJ_1(\kappa a)\Big[J_0(\kappa a)\Big(\frac{n_{\text{core}}^2}{n_{\text{clad}}^2}+1\Big)+2\kappa a\ln\frac{e^\gamma\xi a}{2}J_1(\kappa a)\Big]=0. \tag{4.57}$$

The $\ln\xi$ term tends toward negative infinity as $\xi\to 0$. The term, $J_0(\kappa a)$, does not have enough flexibility to overcome it. Therefore, in order for equation 4.57 to hold true,

$$\kappa a=0 \tag{4.58}$$

or

$$J_1(\kappa a)=0. \tag{4.59}$$

Note here that the solution $\kappa a=0$ is included in equation 4.59.

Finally, consider the case of $\nu>1$. From equation D.16,

$$\lim_{\xi\to 0}H_1^+=-\frac{2}{\xi^2a^2}$$

and

$$\lim_{\xi\to 0} H_1^- = \frac{1}{2(\nu-1)}.$$

Equation 4.51 now becomes

$$\Big(\frac{n_{\text{core}}^2}{n_{\text{clad}}^2}\frac{1}{\kappa a}\frac{J_{\nu-1}(\kappa a)}{J_\nu(\kappa a)} - \frac{1}{2(\nu-1)}\Big)\Big(\frac{1}{\kappa a}\frac{J_{\nu+1}(\kappa a)}{J_\nu(\kappa a)} + \frac{2\nu}{\xi^2 a^2}\Big) + \Big(\frac{n_{\text{core}}^2}{n_{\text{clad}}^2}\frac{1}{\kappa a}\frac{J_{\nu+1}(\kappa a)}{J_\nu(\kappa a)} + \frac{2\nu}{\xi^2 a^2}\Big)\Big(\frac{1}{\kappa a}\frac{J_{\nu-1}(\kappa a)}{J_\nu(\kappa a)} - \frac{1}{2(\nu-1)}\Big) = 0$$

and

$$\Big(\frac{n_{\text{core}}^2}{n_{\text{clad}}^2}J_{\nu-1}(\kappa a) - \frac{\kappa a}{2(\nu-1)}J_\nu(\kappa a)\Big)\Big(\xi^2 a^2 J_{\nu+1}(\kappa a) + 2\nu\kappa a J_\nu(\kappa a)\Big) + \Big(\frac{n_{\text{core}}^2}{n_{\text{clad}}^2}\xi^2 a^2 J_{\nu+1}(\kappa a) + 2\nu\kappa a J_\nu(\kappa a)\Big)\Big(J_{\nu-1}(\kappa a) - \frac{\kappa a}{2(\nu-1)}J_\nu(\kappa a)\Big) = 0.$$

At this point, one can drop terms including simple powers of ξ, they will vanish as $\xi \to 0$; and

$$2\nu\kappa a J_\nu(\kappa a)\Big[J_{\nu-1}(\kappa a)\Big(\frac{n_{\text{core}}^2}{n_{\text{clad}}^2}+1\Big) - \frac{\kappa a}{\nu-1}J_\nu(\kappa a)\Big] = 0. \tag{4.60}$$

Upon first inspection, there appear to be three possible solutions,

$$\kappa a = 0, \tag{4.61}$$

$$J_\nu(\kappa a) = 0, \tag{4.62}$$

and

$$J_{\nu-1}(\kappa a)\Big(\frac{n_{\text{core}}^2}{n_{\text{clad}}^2}+1\Big) - \frac{\kappa a}{\nu-1}J_\nu(\kappa a) = 0. \tag{4.63}$$

However, equation 4.61 is not really a solution. This can be seen by going back to equation 4.51. Approximating the behavior of $J_\nu(\kappa a)$ near $\kappa a = 0$ by taking the first

term in equation D.5, one gets the following for $\nu > 1$,

$$\lim_{\kappa a \to 0} J_\nu^+ = \frac{1}{2(\nu - 1)}$$

and

$$\lim_{\kappa a \to 0} J_\nu^- = \frac{2\nu}{\kappa^2 a^2}.$$

Inserting these results into equation 4.51, one gets

$$\Big(\frac{n_{\text{core}}^2}{n_{\text{clad}}^2}\frac{2\nu}{\kappa^2 a^2} - \frac{1}{2(\nu-1)}\Big)\Big(\frac{1}{2(\nu+1)} + \frac{2\nu}{\xi^2 a^2}\Big) + \Big(\frac{n_{\text{core}}^2}{n_{\text{clad}}^2}\frac{1}{2(\nu+1)} + \frac{2\nu}{\xi^2 a^2}\Big)\Big(\frac{2\nu}{\kappa^2 a^2} - \frac{1}{2(\nu-1)}\Big) = 0.$$

As κa and ξa tend toward zero, the terms with $\kappa^2 a^2$ and $\xi^2 a^2$ in the denominator completely dominate the terms containing ν. This leads to the following simplification,

$$\frac{4\nu^2}{\kappa^2 \xi^2 a^4}\Big(\frac{n_{\text{core}}^2}{n_{\text{clad}}^2} + 1\Big) = 0, \tag{4.64}$$

which does not stay bounded as $\kappa a \to 0$ and $\xi a \to 0$. Since a solution to equation 4.51 must also satisfy equation 4.64, equation 4.61 is not a solution.

4.2.7 Modal Nomenclature

Up to this point, the term *mode* has been glossed over. In the most general sense, a mode is any electro-magnetic wave incident on the fiber optic strand. Of this infinity of modes, only a very small subset is "guided", meaning that the phase of the incident wave on one end is preserved upon exit from the other end. The non-guided modes correspond to situations where the wave goes in off-axis and is radiated away from the core (the wave "just passes through"). Mode mixing in multi-mode fiber optic strands leads to corruption of the phase of the incident wave. It can be partially overcome at the cost of bandwidth (Shaklan, 1989).

In the case of waveguides of rectangular geometry, the modes split very neatly into *transverse magnetic* (TM) and *transverse electric* (TE) modes. In a TE mode, the value of the longitudinal component of $\boldsymbol{E}$ is zero, and the components of $\boldsymbol{E}$ and $\boldsymbol{H}$ depend only on the longitudinal component of $\boldsymbol{H}$. In the case of a TM mode, the roles of $\boldsymbol{E}$ and $\boldsymbol{H}$ are reversed (Wangsness, 1986).

Waveguides having a cylindrical geometry do not split their modes so neatly. Most of the modes are hybrid modes, having contributions from the longitudinal components of both $\boldsymbol{E}$ and $\boldsymbol{H}$. If the mode has a larger contribution from $\boldsymbol{H}$ than $\boldsymbol{E}$, at some reference point, the mode is designated HE. If the mode has a larger contribution from $\boldsymbol{E}$ than $\boldsymbol{H}$, the mode is designated EH. In addition to the hybrid modes, TM and TE modes also exist for the cylindrical geometry.

Following Snitzer (1961), equation 4.56 is the cutoff condition for both the TM and TE modes. Equation 4.58 is the cutoff condition for the HE_{11} mode (the subscripts will be described shortly), while equation 4.59 is that for more HE modes. Finally, equation 4.62 cuts off EH modes, while equation 4.63 cuts off HE modes. In summary,

$$
\begin{aligned}
&TM_{0\eta} : J_0(\kappa a) = 0 && \nu = 0 \\
&TE_{0\eta} : J_0(\kappa a) = 0 && \nu = 0 \\
&HE_{11} : \kappa a = 0 && \nu = 1 \\
&HE_{1\eta} : J_1(\kappa a) = 0 && \nu = 1 \\
&HE_{\nu\eta} : J_{\nu-1}(\kappa a)\left(\frac{n_{\text{core}}^2}{n_{\text{clad}}^2} + 1\right) - \frac{\kappa a}{\nu - 1} J_\nu(\kappa a) = 0 && \nu > 1 \\
&EH_{\nu\eta} : J_\nu(\kappa a) = 0 && \nu > 0.
\end{aligned}
$$

In the above equations, ν represents the order of the Bessel function in question, and η represents the ηth *root* of said Bessel function. However, the numbering of the roots does not include the one at 0 for J_ν, $\nu \neq 0$. So, $\eta = 1$ corresponds to the first (positive) root *not* passing through the origin. At $\nu = 1$, note the degeneracy of $HE_{1\eta}$ and $EH_{\nu\eta}$. The cutoff conditions are identical for HE_{12} and EH_{11}, HE_{13} and EH_{12}, etc. In general, $HE_{1(\eta')}$ and $EH_{1(\eta'-1)}$ are degenerate for $\eta' > 1$.

Marcuse (1982) calculates κa for the cutoff at several of the lower order combinations. The results are summarized in Table 4.1.

$\text{Mode}_{\nu\eta}$	κa	$\text{Mode}_{\nu\eta}$	κa
HE_{11}	0.000	EH_{21}	5.136
TM_{01} TE_{01}	2.405	TM_{02} TE_{02}	5.520
HE_{21}	2.445	HE_{22}	5.538
HE_{12} EH_{11}	3.832	HE_{13} EH_{12}	7.016

Table 4.1: Mode designation and value of κa at cutoff. For the HE modes, $\nu > 1$, $n^2_{\text{core}}/n^2_{\text{clad}} = 1.1$. Adapted from Marcuse (1982).

From looking at Table 4.1, one easily sees the single-mode regime.

$$0 < \kappa a < 2.405 \tag{4.65}$$

Recall that κ contains the mode propagation constant and is frequency dependent. The value κa is known as the *normalized frequency*. The frequency at the upper limit is given by (using equation 4.43),

$$\begin{aligned}
\kappa^2 &= k_c^2 - \omega_c^2 n^2_{\text{core}} \epsilon_0 \mu_0 \\
&= k_c^2 - \frac{\omega_c^2 n^2_{\text{core}}}{c^2} \\
&= \frac{\omega_c^2 n^2_{\text{clad}}}{c^2} - \frac{\omega_c^2 n^2_{\text{core}}}{c^2} \\
&= \frac{\omega_c^2 |n^2_{\text{clad}} - n^2_{\text{core}}|}{c^2} \\
\kappa a &= 2.405 \\
\frac{\omega_c(\text{N.A.})}{c} a &= 2.405 \\
\frac{2\pi f_c(\text{N.A.})}{c} a &= 2.405 \\
f_c &= \frac{2.405 c}{2\pi a(\text{N.A.})}
\end{aligned}$$

The absolute value of the difference between the squares of the indices of refraction is taken because the interest here is the magnitude of κ. Note also the substitution of

numerical aperture (N.A.) into the above equations. The waveguide is single-mode so long as

$$0 < f_c < \frac{2.405c}{2\pi a(\text{N.A.})}. \tag{4.66}$$

If one makes the following change of variable,

$$\begin{aligned} \mathcal{V} &= \frac{2\pi a}{c}(\text{N.A.})f_c \\ &= \frac{2\pi a}{\lambda}(\text{N.A.}), \end{aligned}$$

Equation 4.66 simplifies to

$$0 < \mathcal{V} < 2.405, \tag{4.67}$$

which, by comparison to Equation 4.65, indicates that $\mathcal{V}$ is just the normalized frequency.

4.3 Physical Properties of Real Strands

The discussion in Section 4.2 involved a simplification of the geometry to explore the basic idea of a guided mode. In an actual fiber optic strand, there are other effects that must be dealt with; among them, dispersion (waveguide, material, and modal), birefringence, polarization, and coupling. These will all be discussed (to various depths) in the subsequent sections.

4.3.1 Strand Properties

The type of fiber optic strand used in the prototype is the F-SV (see Appendix B for the vendor list). The properties are summarized in Table 4.2.

4.3.2 Dispersion

Dispersion in single-mode dielectric waveguides can be addressed by three basic effects, waveguide, material, and modal dispersions. These effects can be seen qualita-

Property	Value
core diameter ($2a$)	3.8 μm
cladding diameter	125 μm
sheath diameter	250 μm
n_{core}	1.4616
n_{clad}	1.4571
N.A.	0.11
λ_c	546 nm
$2w$	4.2 μm

Table 4.2: Properties for the Newport F-SV Single-Mode Fiber Optical strand. λ_c is the cutoff wavelength and $2w$ is the mode field diameter at λ_c (see Section 4.3.4).

tively through the use of a dispersion curve diagram, shown in Figure 4.1. Recall from equation 4.43, that the propagation constant, k_g, has a wavelength dependence. In the diagram, the propagation constant is plotted versus the frequency. If the indices of refraction of both the core and cladding are independent of the frequency, the core and cladding can both be represented as (different) straight lines in the diagram.

The effects of waveguide dispersion are plotted schematically for the HE_{11} mode in Figure 4.1. Starting at a frequency of zero, equation 4.43 shows that the propagation constant is also zero. As the frequency is increased, the propagation constant follows the line corresponding to the cladding for a bit (note the subscript of the index in equation 4.43). As the frequency increases yet further, more and more of the energy of the guided wave is concentrated in the core. This can be seen by looking at the form of equation 4.42, higher frequencies translate to larger values of ξ and a higher concentration of energy in the core material. This "S"-shaped functional dependence of k_g on frequency is known as waveguide dispersion.

Material dispersion is the most well known effect of the three. It is what allows prisms to work, and is also the reason why the lengths of any two fiber optic strands used as conduits for beam combination must be very close in length (depending on the bandwidth). In general, dielectrics, such as the glasses used in typical single-mode fiber optic strands, have a greater dispersion (a larger change in the propagation constant per unit frequency interval) at higher frequencies. In Figure 4.1, material dispersion would have the effect of bending the limiting lines corresponding to the core

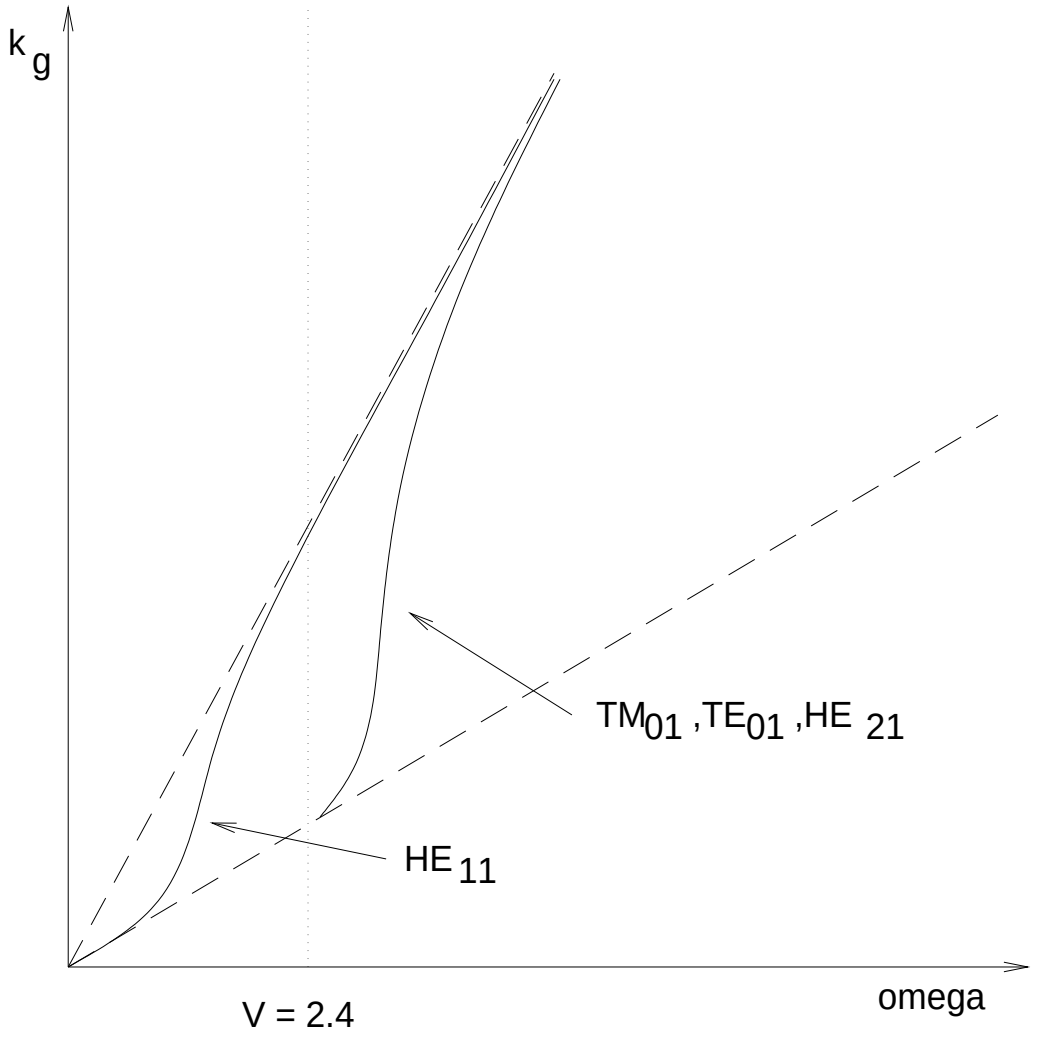

Figure 4.1: Plotted here is a qualitative diagram of the dispersion curve of a single-mode strand. The upper dashed line corresponds to $k_g n_{\text{core}}$ while the lower one corresponds to $k_g n_{\text{clad}}$. The angle between the curves has been greatly exaggerated to reveal the morphology of the dispersion curve. Several modes have been plotted.

and cladding regimes, curving them both upward, the curve getting steeper as the frequency increases. In the visible realm, material dispersion dominates waveguide dispersion.

Recall that circular core dielectric waveguides support more modes than just the HE_{11} mode. At a normalized frequency ($\mathcal{V}$) of 2.405, the waveguide is no longer single-mode. Abruptly, the TE_{01} and TM_{01} modes begin to be guided. Like the HE_{11} mode, the TE_{01} and TM_{01} modes start at the line corresponding to the cladding material and work their way to the core line asymptotically. The different value of the propagation constant at a given frequency for the different modes is known as modal dispersion.

4.3.3 Birefringence and Polarization

As was alluded to in Section 4.2, real waveguides have effects of birefringence. In the ideal case, the HE_{11} mode is actually two degenerate, orthogonal, and linearly polarized HE_{11} modes. A component is birefringent if it somehow breaks the degeneracy of the two modes. Following Eickhoff et al. (1981), birefringence comes about from circular core cross-section deviations, bending ("transverse stress"), and longitudinal twist. The core deviations and bending lead to a linear birefringence, while the twist leads to a circular birefringence. These two types of birefringence are related to each other in the same way as linear and circular polarization are related to one another.

When polarized light is coupled into a waveguide, the state of polarization varies continuously along the strand. This comes about because the core and cladding are concentric. Core deviations are difficult to detect independently because the effects of bending and twisting tend to dominate. However, since the goal here is not to know the exact core shape, only to use the strand as a conduit, only the polarization difference between the input and output needs to be known. These can be tuned by bending and twisting (Shaklan, 1990).

Birefringence is characterized by minute changes in the propagation constant. Bending the strand sets up a birefringent condition where the axes are parallel to the radius of curvature and perpendicular to the plane of the bend. The propagation

constant change is approximated by

$$\delta k_g \simeq -\frac{0.85}{\lambda}\Big(\frac{r}{R}\Big)^2 l, \tag{4.68}$$

where δk_g is in radians, r is the radius of the cladding, R is the radius of the bend, and l is the length of the bent strand in meters (Shaklan and Roddier, 1987). Equation 4.68 is a worst case scenario, it assumes that all of the strand is bent in the same plane. The effect cancels if two equal-length sections of the strand are bent in perpendicular planes. A twist in the strand rotates the polarization according to

$$\Omega = 0.073\tau l,$$

where Ω is in radians, τ is the twist rate in radians per meter, and l is the length of the twist in meters (Shaklan and Roddier, 1987).

4.3.4 Coupling

The HE_{11} mode profile, determined by Equations 4.29–4.34 in the core and Equations 4.35–4.40 in the cladding, very closely approximates a Gaussian,

$$I_{HE_{11}}(\rho) = \Big(e^{-\frac{\rho^2}{w^2}}\Big)^2. \tag{4.69}$$

Marcuse (1977) empirically found the 1/e-width (as a function of $\mathcal{V}$) of this Gaussian to be,

$$w = a\Big(0.65 + \frac{1.619}{\mathcal{V}^{\frac{3}{2}}} + \frac{2.879}{\mathcal{V}^6}\Big). \tag{4.70}$$

The "best fit" approximate Gaussian is found by equating the power of the Gaussian and the actual mode profile and determining w. Buck (1995) finds the ratio of the actual mode profile to the Gaussian to be 0.94 at $\mathcal{V} = 1.2$ and ~ 1 at $\mathcal{V} = 2.4$. A normalized frequency of 1.2 corresponds to a wavelength of over 1 μm, well longer than any wavelength used, so the Gaussian approximation can be used in all cases.

Since the beams from the telescopes have Fresnel type far-field diffraction, bringing the beam to a focus on the strand tip creates an Airy spot. Following Born and

Wolf (1989)

$$I_{\text{Airy}}(\rho) = \left(\frac{2J_1(\alpha\rho)}{\alpha\rho}\right)^2,$$

where

$$\alpha = \frac{2\pi R_{\text{aperture}}}{\lambda f_{\text{lens}}}. \tag{4.71}$$

Coupling this Airy spot to the Gaussian mode of the optical strand involves losses. However, the coupling can be quite good if the focal length of the Launcher system lens (see Section 5.3.1) is chosen such that the Airy spot diameter closely matches the mode diameter at the specific wavelength of interest. Figure 4.2 shows the effects of the choice of lens at a wavelength of 547.2 nm, near the cutoff wavelength of the fiber optic strand used in the prototype. All tests were done using the 120 mm focal length lens.

The above analysis is for images which are not atmospherically degraded. In the CHARA Array, these images will not be perfect. The CHARA Array will have a tip-tilt system in operation which will keep the Airy spot centered on the strand tip. However, the higher order aberrations will still be present. Assuming that a static alignment can consistently be found, Shaklan and Roddier (1988) give estimates of coupling efficiency versus normalized frequency for several different seeing conditions.

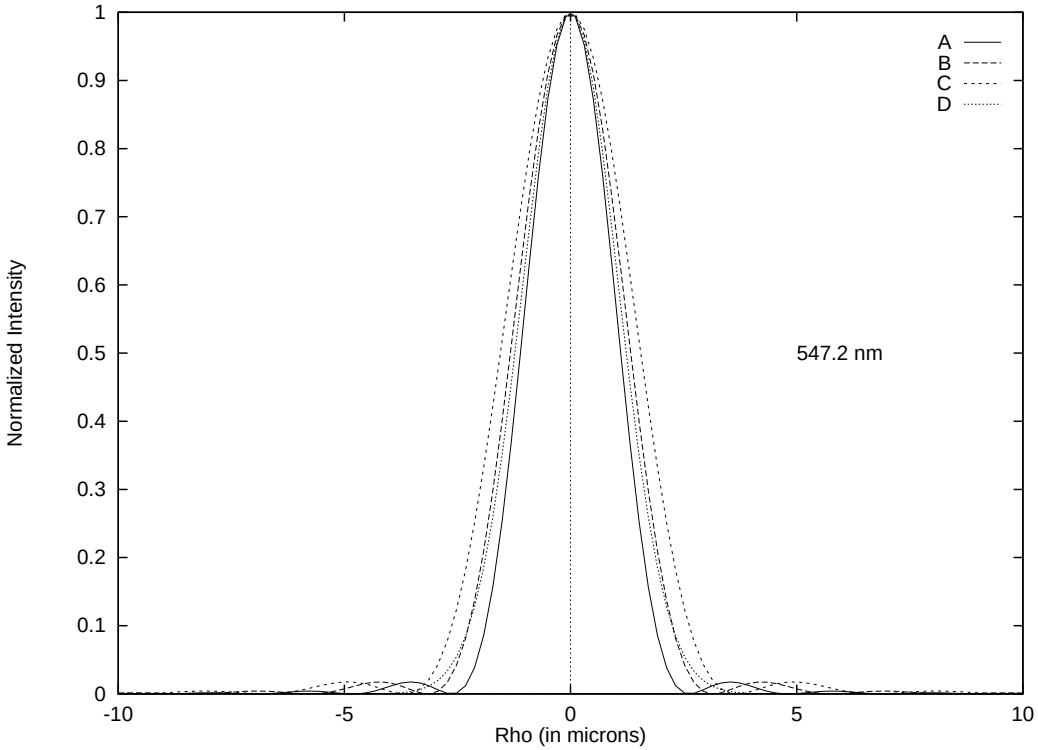

Figure 4.2: Here is shown the HE_{11} mode profile (Curve D) and Airy spots for three different focal lengths of lenses, 100 mm (Curve A), 120 mm (Curve B), and 140 mm (Curve C). The wavelength is 547.2 nm, very close to the wavelength cutoff of the 3.8 μm core diameter optic strand.

Chapter 5

The Prototype Imager – Construction

5.1 Overview

The prototype imager discussion is split into two chapters. This chapter describes aspects of the construction of the imager while Chapter 6 describes data collected with two versions of the Imager. The first version interfered two beams as a proof of concept and the second version realized the final version of the prototype – three beams lined up in a non-redundant, linear pattern. The main systems of the imager break very neatly into three opto-mechanical systems and a "system" involving the fiber optic strands by themselves. The three opto-mechanical systems have been named the *Fiber Launcher*, *Fiber Collimator*, and *Spectrograph* systems. A listing, by system, of all the parts used can be found in Appendix A. Appendix B lists contact information for vendors of the key elements of each system. Finally, Appendix C lists all of the shop drawings used to create the prototype imager.

5.2 Creation of Fiber Optic Strands

As was touched upon in Chapter 3, the key element in the imager is fiber optic strands – single-mode strands in the present case. One of the main frustrations in dealing with these strands is their fragility. The strands – core, cladding, and sheath

– typically have outer diameters of a quarter of a millimeter. This, coupled with their transparency, tends to make them invisible against almost all backgrounds until one is quite close. This leaves the strands vulnerable to breakage from careless snags, slipped tools, etc. A popular method of getting a smooth surface for clean input and output of light is to "cleave" the tip of the strand. This is done by scoring the spot on the strand where the new end is to be and gently bending the strand until it breaks at that point, (hopefully) leaving a smooth surface. However, in order to score the glass strand effectively, one must dissolve away the plastic sheath in the vicinity of the strand tip. The glass is very brittle and is even more vulnerable without the protective sheath.

Georgia State University developed a spectroscopic telescope which uses fiber optic strands to convey the light to a modified Ebert-Fastie spectrograph (Barry 1995). In the development of that instrument, various methods of making the fiber optic strands more robust were investigated. In the end, it was decided to run the strand through a length of teflon tubing, with each end of the teflon securely fastened – one end to the telescope, and the other end to the spectrograph. Snags of the the assembly will be borne by the teflon rather than the strand. In addition to the teflon tubing, short lengths of stainless steel tubing ("hypodermic" tubing) are adhered to each end of the strand. To achieve a smooth surface, the end is polished – glass, plastic, adhesive, stainless steel and all. Also, single-mode fiber optic strands benefit from a nice piece of steel on which to clamp without fear of disturbing the coupling properties. The procedures in Sections 5.2.1 and 5.2.2 follow Barry (1995), Sections 4.5 and 4.6.

5.2.1 Preparation for Polishing

For the prototype, the strand length has been standardized to 255.3 cm (8' 4.5"). Because the strands used in the prototype were constructed at different times some variation of the standard was noted. In fact, this oversight prevented all three baselines from being simultaneously observed (Section 6.5.2). The present section and the next are excerpts from the laboratory log.

Hold down clamps for the teflon tubing and fiber optic strands have been designed for the above strand length and a teflon tubing length of 243.8 cm (8'). Using the long axis of a common SAE threaded optical table from Newport Corporation works

well as a guide. A sharp razor blade makes a very clean cut. Teflon is prone to be statically charged and as a result collects dust. This dust can impede the insertion of the strand. Dust the tubing by running the length of the tubing between two fingers. Fasten the tubing to a flat surface long enough to be able to straighten out the entire length of the tubing. This process vastly eases the insertion of the strand. Carefully insert the strand, pushing in about 3 cm at a time. The strand is longer than the tubing, so equalize the extra length between the two ends. These can be re-adjusted at any time so long as the tubing is relatively straight. Carefully coil up the tubing.

At this point, one needs to prepare the short lengths of stainless steel tubing for adhering to the strand ends. Cut off two lengths of tubing, each about 2.5 cm using diagonal cutters. The cutters will pinch the ends of the tubing, so one needs to grind away tubing material until the interior hole is round. This is done by gripping the tubing with a pin-vise and manually grinding it dry against 167 grit (or similar) silicon carbide paper. Progress was monitored with a 100X microscope with a modified viewing stage. The microscope modifications are discussed in Section 5.2.2. When the hole looks round, one must clear the debris inside. Occasionally compressed air will work, but using a short length of scrap strand is the most effective. There will be times in which neither of these methods will work. When this happens, start over with a new length of tubing. Both ends of the tubing need to be ground, in that the diagonal cutters pinch both sides.

One must now adhere these short lengths of tubing to each end of the strand. The adhesive used is a zero-shrink epoxy. The standard five-minute epoxies shrink a small bit as they cure. This can lead to "micro-kinks" in the strand and possible mode scrambling (a change of the guide properties). On a scrap of disposable material, place eight drops of resin and one drop of hardener. Use separate toothpicks in the resin and hardener to avoid contamination. Mix the adhesive thoroughly. Typically, this means about a minute or a minute and a half, when the mixture becomes a uniform color and stiffens. Slide each of the lengths of the tubing onto their respective ends of the strand so that about 3 cm of the strand sticks out. Liberally apply the adhesive to both ends of the exposed strand. Slide the tubing to a point where only about 1 mm of strand is exposed. Use the toothpick to remove the globule of adhesive. Pull the tubing back to where 3 cm of the strand is exposed and repeat this process. After the third time, enough adhesive will have wicked its way into the gap between

the tubing and strand to give a good bond. With about 1 mm of exposed strand past the tubing on each end, let the epoxy cure. Get as much of the globule of epoxy off the ends as possible. Let the epoxy cure at least 72 hours. Let it cure longer if there is time. Be sure the ends are suspended so they do not get adhered to any surface.

5.2.2 Polishing Process

The polishing process makes use of aluminum oxide abrasive sheets in seven grit sizes – 60, 30, 12, 5, 3, 1, and 0.3 μm and a liquid polishing extender. In addition, one needs a specially designed jig to keep the stainless steel tubing perpendicular to the abrasive surface during the polishing process. This jig consists of a pin-vise held within a cylindrical sleeve by a set screw (*Fiber Vise, Part A*, Figure C.24). This assembly, in turn, slides within another larger cylindrical sleeve (*Fiber Vise, Part B*, Figure C.25). The final tool used in the polishing process is a modified microscope. The standard viewing stage is removed in favor of a jig which can accomodate the *Fiber Vise, Part A* (*Microscope Stage, Part A*, Figure C.26).

Before beginning the polishing process, one must mount the strand tip in the *Fiber Vise, Part A*. The pin-vise chosen is hollow. Insert the strand tip into the back-end of the pin-vise. Clamp onto the stainless steel tubing, leaving about 3–5 mm of tubing to protrude beyond the *Fiber Vise, Part A*. Carefully tape the teflon tubing to the pin-vise for strain relief.

The first step in polishing a strand end involves grinding away the excess epoxy on the outside of the stainless steel tubing. This process can be simplified if the *Fiber Launcher, Assembly 4, Part B* is readily at hand. This part has a hole in one end in which the stainless steel tubing is designed to fit. Using an old sheet of the above mentioned 60 μm grit abrasive dry works well. A magnifying lens (about 10–30X) will help to see where the pieces of cured adhesive are located. Holding the *Fiber Vise, Part A* horizontal, grind away the excess adhesive, periodically checking it for fit in the *Fiber Launcher, Assembly 4, Part B*. Once it fits easily, wipe it clean of loose debris.

The polishing process is straight-forward, and tedious. One progressively goes from the 60 μm grit abrasive to the 0.3 μm grit. Start by taping an abrasive sheet to a hard and flat surface. Place ten drops of the polishing extender on an unused section of the abrasive sheet. Gently set the *Fiber Vise, Part B* onto this pool. Slide

the *Fiber Vise, Part A* into *Fiber Vise, Part B* and start polishing using very gentle pressure and a tight circular motion. When the pressure is just right, the strand tip will make soft squeaks, much like the sound of a finger running across a clean plate, on all grits except the 60 μm. At the end of the allotted time, thoroughly rinse both of the *Fiber Vise* parts with water and dry them with disposable paper towels. Inspect the strand tip at 100X using the modified microscope. If there are any scratches visible that are much larger in scale than the majority of the others, repeat the polishing process at the present grit size. Once the inspection goes satisfactorily, dab the abrasive sheet dry using a paper towel and go onto the next smaller grit size. Adequate polishing times are three minutes for the 60, 30, 12, and 5 μm grit sizes, and five minutes for the 3, 1, and 0.3 μm grit sizes. After completion, scratches should not be visible at 100X, and the surface should look smooth and the polished stainless steel tubing should be quite reflective.

5.3 Opto-Mechanical Systems

As stated at the beginning of this chapter, the systems of the prototype imager have been divided into three opto-mechanical systems, the Fiber Launcher, Fiber Collimator, and Spectrograph systems. The Fiber Launcher system involves all assemblies associated with getting the light from the 25 mm diameter collimated beams (simulating the beams from the individual Array telescopes) into the fiber optic strands. The Fiber Collimator system involves all assemblies associated with clamping the output ends of the fiber optic strands and getting them into a non-redundant, one-dimensional pattern of smaller (on the order of 3 mm diameter) collimated beams. The Spectrograph system involves all assemblies associated with dispersing the small pattern of collimated beams and re-imaging them onto a detector.

5.3.1 Launcher System

The design philosophy in creating this system was to make assemblies as robust as was practical. By its nature, the prototype imager is a passive device. The more firm the individual components, the less often it will require adjustment.

The foundation of the Launcher system is a rail and carriage assembly. The

rails feature a precision dovetail flange while the carriages, with a matched dovetail groove, employ teflon slide bearings and a spring loaded lock screw. This lock screw limits the side-to-side motion of the carriage while still allowing the carriage to move along the rail. As a result, the carriage performs well as the moveable part in a long translation stage. Adopting this strategy allows one to cover a wide range of launch points for just about any conceivable combination of input and output phase center points.

The prototype described here is for three beam combination. The overall layout is shown in Figure 3.10. These beams simulate the output of CHARA Array telescopes (Chapter 2) and are brought to a focus on the strand tip by means of a two-element, cemented achromat. These achromats have a focal lengths of 120 mm to a 2% precision, and are optimized for wavelengths of 480.0, 546.1, and 643.8 nm. For clarity, these beams will be referred to as "Telescope" 1, "Telescope" 2, and "Telescope" 3. "Telescope" 3 is the reference apparatus. It is not moved in the zero path point search (Section 6.4.5). This reference apparatus consists of an "I"-beam foundation, which supports a gimballed lens mount and a motorized optic strand positioner, bolted onto two carriages. The I-beam apparatus can be seen in Figure 5.1.

"Telescope" 2 and "Telescope" 1 have I-beam foundations nearly identical to that of "Telescope" 3, but since provision has to be made to adjust them relative to the reference, an additional carriage supports a micrometer, creating a repositionable translation stage. A close up of the micrometer assembly is shown in Figure 5.2. The micrometer clamp (the aluminum "L"-bracket in Figure 5.2), has a hole diameter of 0.375 inches (Figure C.6). This is one of the standard sizes for micrometers. It allows an upgrade path to a motorized micrometer should it prove necessary (or convenient!).

Finally, attention needs to be drawn to the manner in which the optic strand tip is located and fastened down. The shop drawings with dimensions and a few tips on construction techniques can be found in Figures C.7, C.8, and C.9. Figure 5.3 shows the backside of the clamp and the way in which the teflon tubing is held to stress relieve the optic strand inside. Note in Figure 5.1 that the strand tip is held in place by a nylon set screw. It was found that if the strand tips were not held down on both ends, coupling and zero path point positions were not repeatable.

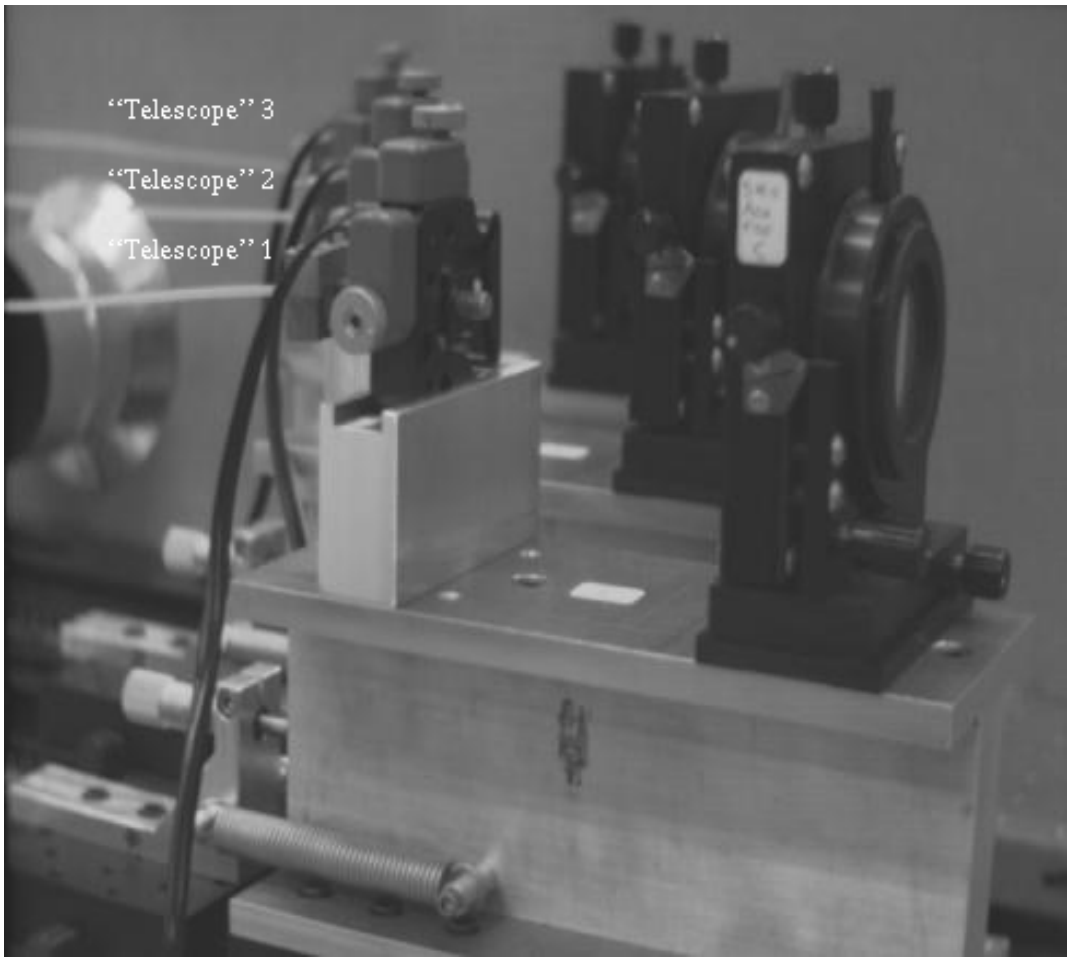

Figure 5.1: A view of the Fiber Launcher system from slightly above the optical axis height. Note that the three input beams are labelled as "Telescope" 3, "Telescope" 2, and "Telescope" 1. These labels are maintained throughout this dissertation.

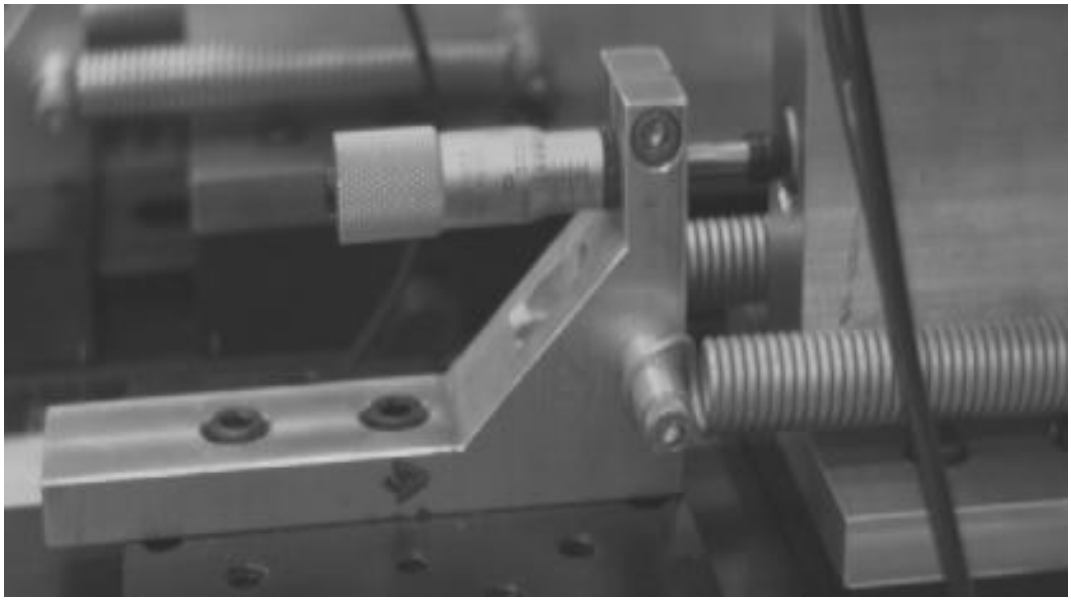

Figure 5.2: A close-up view of the micrometer assembly of the Fiber Launcher System.

5.3.2 Collimator System

The entire Collimator system assembly is show in Figure 5.4. The tubing clamp in the Collimator system is similar to the clamp at the other end, shown in Figure 5.3. To simplify the design (fewer pieces and simpler machining tasks), the top part of the clamp (labelled with a number in Figure 5.4) provides the "rigid" surface for holding down the strand tips. Serendipitously, this allowed an additional freedom of motion in the angular position of the strand tip which turned out to be necessary in tuning the Spectrograph system (see Section 6.4.4).

Commercial lens mounts, which hold 6 mm diameter and 10 mm focal length achromats (same design specifications as the achromats described in Section 5.3.1), are incorporated into a miniaturized, custom-built X-Y-Z translation stage. Because of inaccuracies in machining, during assembly of these custom stages, shims had to be incorporated in order to get the stages to function properly. Finally, in Figure 5.4, note the staggered pattern of each of the "Telescopes". This was done to get the output beams close enough to be able to use off-the-shelf optical element sizes in the Spectrograph system.

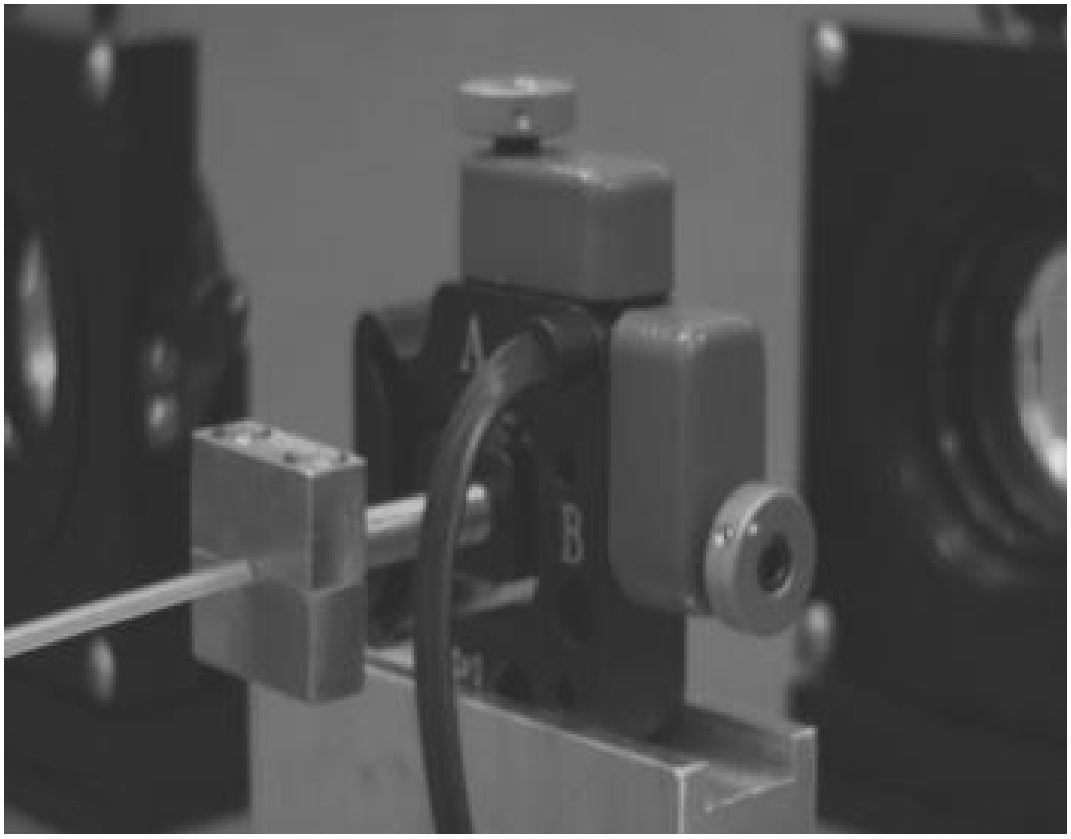

Figure 5.3: A close-up view of the teflon tubing clamp assembly for the Fiber Launcher System. This setup allows the optic strand inside the tubing to be stress relieved

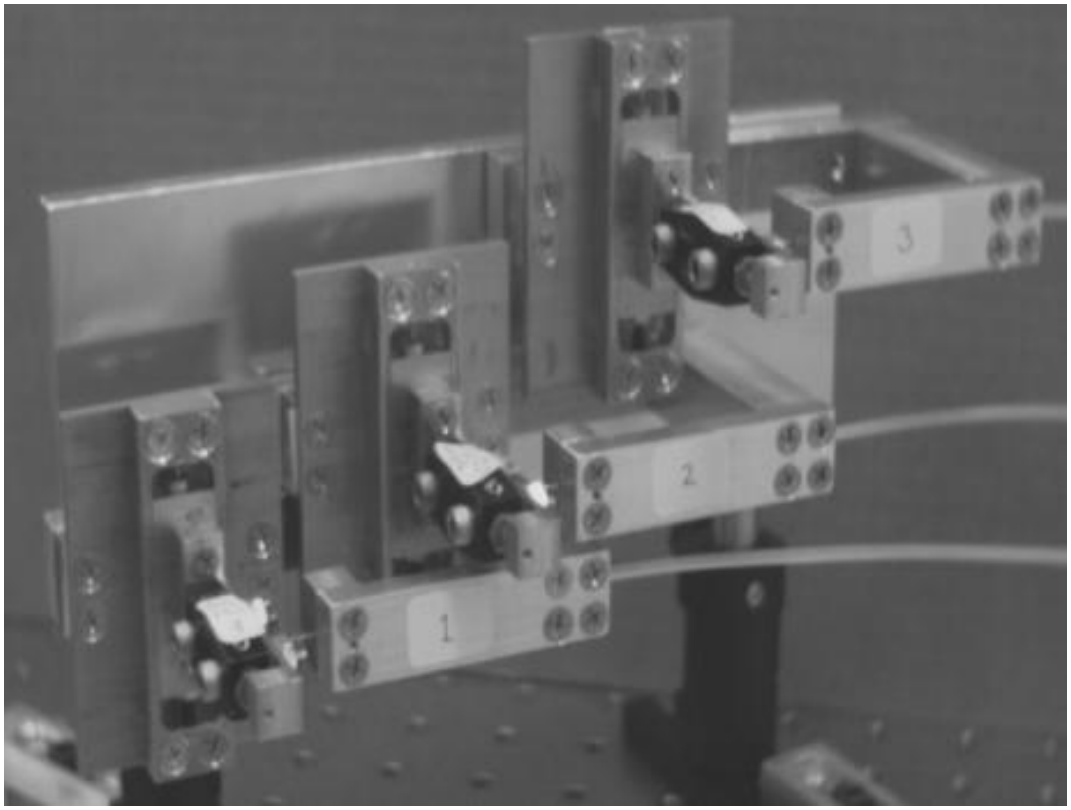

Figure 5.4: The Fiber Collimator System. The "Output" numbers on each system correspond to the "Telescope" numbers in Figure 5.1. "Output" 1 is at the bottom, "Output" 2 in the middle, and "Output" 3 at the top.

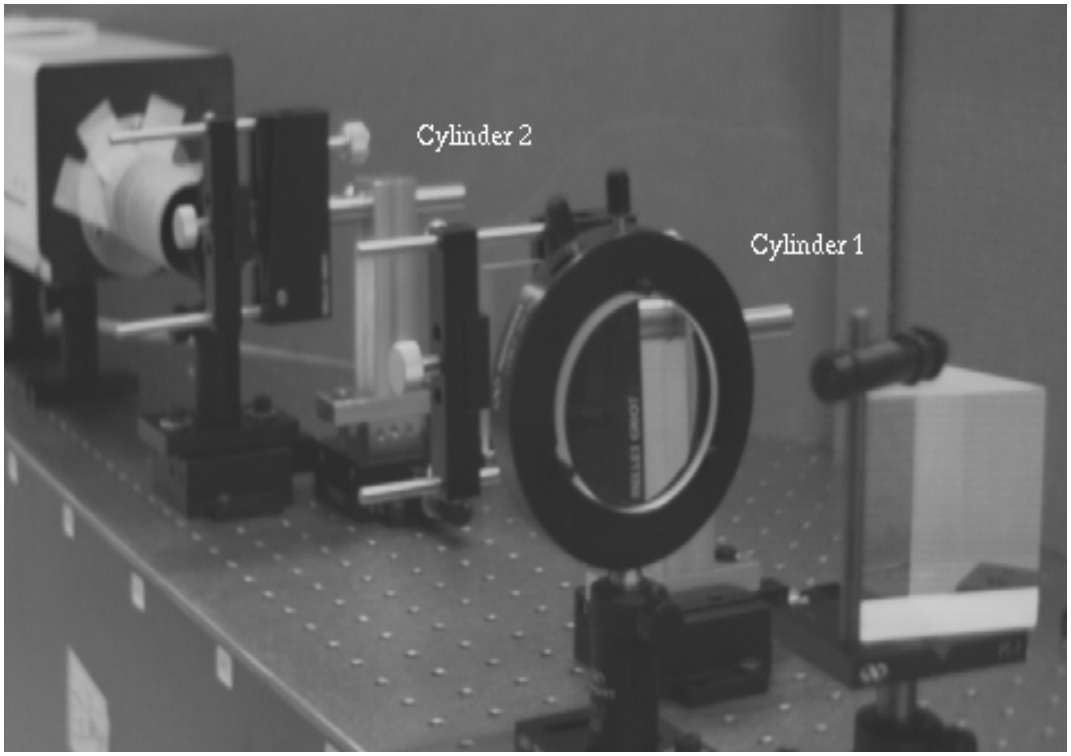

Figure 5.5: The Spectrograph System. Cylinder 1 is a negative element while Cylinder 2 is a positive element.

5.3.3 Spectrograph System

A nearly "photon's-eye" view of the Spectrograph system is shown in Figure 5.5. Almost all the parts are standard laboratory-grade components (including the optics), which as was proposed in Chapter 3, is the driving force behind building this prototype. The only custom parts are the components which hold the cylindrical optical mounts horizontal.

After leaving the Collimator system, the output beams pass through an equilateral prism (60 mm on each dimension) made of BK7 glass (a Schott Glass Technologies borosilicate crown glass). A prism was chosen over a diffraction grating solely on throughput considerations. The system can be modified to accomodate a diffraction grating should higher spectral resolution and/or linear dispersion be desired.

In the Schott glass catalog (http://www.schottglasstech.com/), the dispersion char-

acteristics are described in terms of the Sellmeier 1 formula,

$$n^2 = 1 + \frac{k_1\lambda^2}{\lambda^2 - l_1} + \frac{k_2\lambda^2}{\lambda^2 - l_2} + \frac{k_3\lambda^2}{\lambda^2 - l_3}. \tag{5.1}$$

The six constants for BK7 are listed in Table 5.1. Based on straightforward ap-

Constant	Value
k_1	1.039612120×10^0
l_1	$6.000698670 \times 10^{-3}\mu\text{m}^2$
k_2	$2.317923440 \times 10^{-1}$
l_2	$2.001791440 \times 10^{-2}\mu\text{m}^2$
k_3	1.010469450×10^0
l_3	$1.035606530 \times 10^2\mu\text{m}^2$

Table 5.1: The dispersion constants for BK7 following the Sellmeier 1 dispersion formula.

plication of Snell's law and the Rayleigh criterion, the resolving power of a prism spectrograph is given as (Klein and Furtak 1986, Section 6.4),

$$\frac{\lambda}{\Delta\lambda} = b\frac{dn}{d\lambda},$$

where b is the length of the base of the prism and $dn/d\lambda$ is the derivative of equation 5.1,

$$\frac{dn}{d\lambda} = -\frac{\lambda}{n}\Big[\frac{k_1 l_1}{(\lambda^2 - l_1)^2} + \frac{k_2 l_2}{(\lambda^2 - l_2)^2} + \frac{k_3 l_3}{(\lambda^2 - l_3)^2}\Big], \tag{5.2}$$

where n is the square root of equation 5.1. Note in equation 5.2 that

$$\frac{dn}{d\lambda} \propto \frac{1}{\lambda^3}$$

The dispersed light from the prism is then passed through a 63 mm diameter, 400 mm focal length achromat (with the same design specifications as the achromats described in Sections 5.3.1 and 5.3.2), and through the negative and positive cylindrical elements. The negative cylinder has a focal length of -300 mm while the positive cylinder has a focal length of 12.7 mm. Both elements are made of BK7 glass.

Chapter 6

The Prototype Imager – Data Collection

6.1 CHARA Optical Laboratory Facilities

The optical experimentation facilities at GSU that CHARA administers include four optical tables in two separate laboratories. Both laboratories are in the basement of the GSU Natural Sciences Building. Three of the optical tables are Newport Corporation RS-2000 series, 4'×8'×8" (width×length×thickness), floating on air for vibration isolation. The fourth optical table is a Newport Corporation RS-3000 series, 4'×8'×12", again, floating on air for vibration isolation. All experiments subsequently discussed were performed on this optical table.

The RS-3000 optical table is equipped with a 100 watt, tungsten filament light source and a 10 milliwatt, 632.8 nm Helium-Neon laser (HeNe). Each light source has an optical system to create nearly parallel 25 mm collimated beams. Through the use of a mirror in the tungsten lamp beam and a cube beam splitter at the intersection of the HeNe laser and tungsten lamp beams, the beams are made coincident (Section 6.4.1 describes the technique used to superimpose the HeNe laser and tungsten lamp beams). At the main beam splitter, there are two sets of superimposed sources, one where the HeNe beam is in reflection (within the beam splitter) and tungsten lamp beam is in transmission, and the other where the HeNe beam is in transmission and the tungsten lamp beam is in reflection. It was decided to build the Launcher system on the former set of beams.

The three beams simulating the Array telescopes are created by two plate beam splitters and a mirror. The first beam splitter in the input chain is a 30/70 (reflected/transmitted) beam splitter. This beam splitter feeds the fixed launcher. The second beam splitter in the input chain is a 50/50 beam splitter. The mirror caps the input chain, finalizing the Array telescope simulation. The plate beam splitters used are on the order of 1 mm thick and are not compensated. Since the lengths of the fiber optic strands are only equalized to within a few millimeters, a few extra millimeters of glass difference is acceptable. The extra dispersion shows up as a relative displacement of the zero-path-length point. The plate beam splitters have over three waves (at 632.8 nm) of error across a 25 mm spot in the center. Because single-mode fiber optic strands are excellent spatial filters, this is also acceptable. Finally, the amount of power in each simulated telescope was measured. Simulated telescope one received 24% of the power, two received 35% of the power, and three received 41% of the power. A schematic layout (showing the relative positions of the simulated telescopes) is shown in Figure 3.10, and a photo is shown in Figure 3.11.

6.2 One Beam Coupling Investigation

Using a crude positioning of the launching lens (the technique was eventually refined and is described in Section 6.4.2), the laser was brought to a focus on the strand tip. It was noted that the polished strand tip reflected off-axis laser light very well (a significant area is polished stainless steel). The laser at full power created too much granulation on the stainless steel to be able to accurately determine where the image was being formed. So, the first step was to reduce the amount of laser power incident on the strand tip through the use of neutral density (ND) filters. Using a flashlight, dimmed through the use of ND filters, the strand tip was faintly illumninated and the X-Y positioner adjusted to center the laser image. Upon removal of the ND from the laser, the cladding faintly glowed the color of the laser for about the first 10 cm of the strand.

Due to inhomogeneities in the diameter of the fiber optic strand sheath and coarse standard sizing of hypo tubing, the inner diameter of the hypo tubing was quite a bit larger than the outer diameter of the sheath. As a result, the strand was not generally centered in the hypo tubing and light did not couple into the core on the

first attempt. Coupling was eventually achieved after much trial-and-error. Times ranged from two days to about a week. The most straight-forward technique (but not necessarily the most efficient) was to use a spiral search pattern.

Once coupling was obtained, the brightness was maximized by adjusting the X-Y strand positioner for a peak in the brightness and then adjusting the focus (Z-axis) of the lauching lens for the maximum brightness. A few iterations produced a satisfyingly bright output spot. Further refinements were made by adjusting the angular position of the lens and re-adjusting the X-Y strand positioner to re-obtain the peak brightness. However, it was noted that the angular adjustments made no discernible improvement in peak brightness to the eye.

Starting with an input power of about 250 μW (the laser fluctuated at the level of about $\pm 5\mu$W), the initial output power was 50 μW. This was a coupling of about 20%, achieving the design goal. It was subsequently discovered by using a spiral search that this power was from a bright spot on one of the Airy rings. Finding the maximum peak in the area brought the output power to 97 μW, increasing the coupling to nearly 39%.

6.3 Two-beam Interference

6.3.1 Proof of Concept

As a proof of concept, a two beam, monochromatic (632.8 nm) interferometer was built. The input mechanism was identical to that described in Section 5.3.1. For the output, a mount was created which held the two fiber optic strands 15.9 mm apart. Two achromats (described in Section 5.3.2) were mounted on the ends of two 63.5 mm lever arms at roughly the correct point to achieve collimation. These two beams were brought to a focus by a 152.4 mm focal length singlet lens. A 10$\times$ microscope objective was was put into the path to magnify the fringe pattern enough to create about ten fringes across a 7.0$\times$5.0 mm (width$\times$height) CCD chip. The CCD camera used here is the Philips Monochrome CCD Imaging Module, VC62505T (Amperex Electronic Company, A Division of North American Philips Corporation, Imaging Products Business Unit, Providence Pike, Slatersville, Rhode Island 02876, USA). Field performance of this camera is touched upon in (Turner et al. 1992). Figure 6.1

Figure 6.1: The experimental setup for acquisition of fringes with two beams. The light exits the fiber at the right of the figure, being first collimated, then sent through a polarizer, then re-imaged with the lens on the left of the figure to a microscope objective (not shown) which magnifies the image for detection by a CCD video camera (not shown).

shows the experimental setup. In spite of the fact that the final adjustment involved balancing astigmatism, focus, and beam parallelism (none was particularly good), excellent fringes were formed at the overlap from the scattered halos of each beam. Figure 6.2 shows the fringes formed at the overlap areas.

Though the proof of concept was successful, it pointed out a number of shortcomings of the conceptual design for the Collimator system. The main problem was the inability to guarantee that the optical axis of the fiber optic strand was parallel to the long axis of the stainless steel tubing. At this point, it was decided to bend the strand tips to achieve parallel optical axes and add an X-Y translational stage to the collimation lenses to compensate for the translation of the optical axis of the strand. The final version is described in Section 5.3.2.

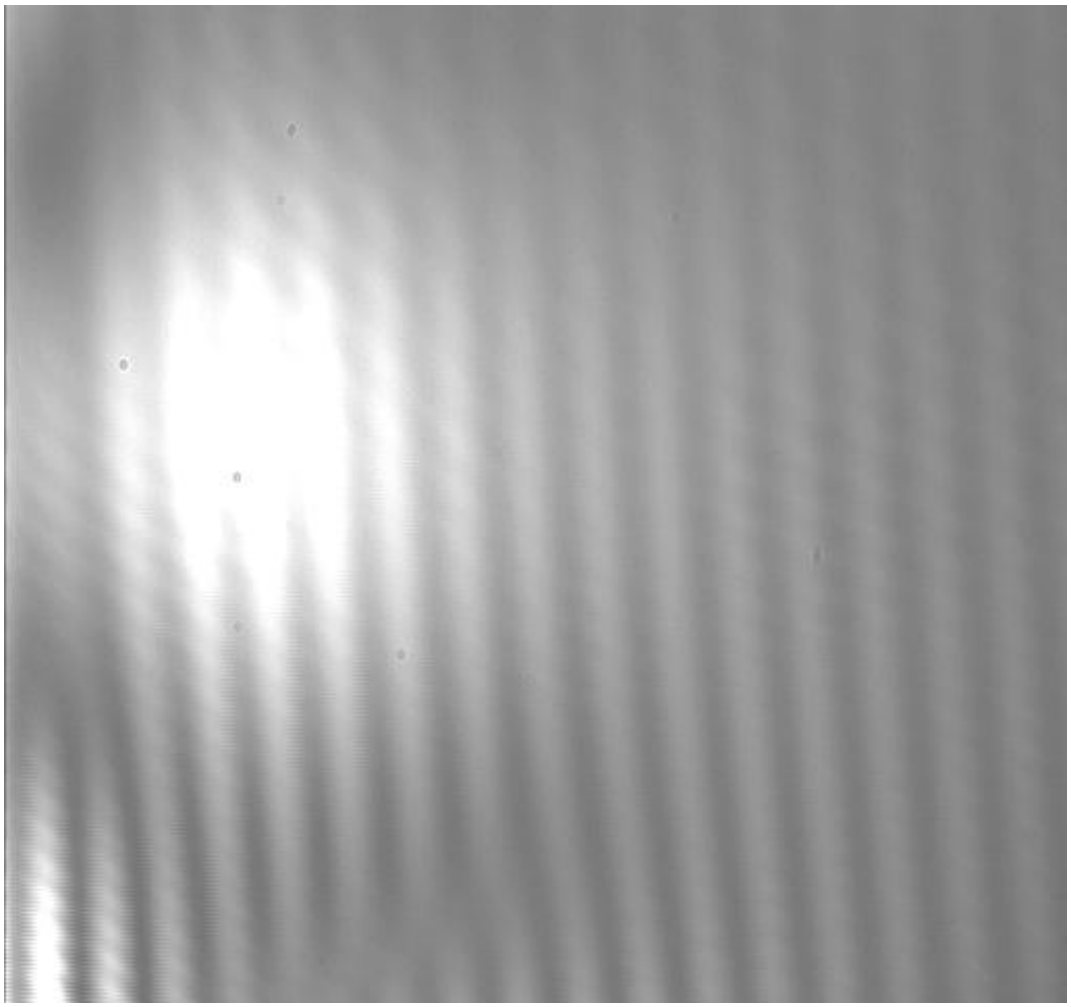

Figure 6.2: Interference fringes from two beams. The cores of the beams do not overlap. These are fringes from the overlapping halos.

6.3.2 Coupling with Laser Light

After performing the proof of concept (Section 6.3), a few tests were performed to evaluate the performance of the fiber optic strand setup with respect to polarization. In Section 4.3.3, a number of empirical relations are quantified with respect to how polarization is affected by physical conditions of the optic strands. The tests performed here were much more qualitative. The prototype imager was not designed with capabilities to measure and/or monitor twists and bends in each individual strand. The first (and very important) observation was that the fringes were still visible in unpolarized light when the reinforced strand cables just dangled loosely off the end of the optical table. Setting the loose cables into motion caused the polarization to vary (as is to be expected) and the contrast of the fringes fluctuated. The contrast was always better with a polaroid filter in place, so for data collection, a polaroid was always used.

Following a lead from Shaklan (1989) and others in the single-mode fiber optic community, an effort was made to control relative polarization between the fiber optic strands. This was done by creating two loops in one of the cables. There was one topological crossing (that is to say that the two loops were not extensions of the same helix). When everything was tied down well, adjusting the angle would change the polarization a slight bit. This technique of polarization control is know colloquially as "Mickey Mouse ears", for the obvious likeness to the signature silhouette of Walt Disney's famous rodent.

By far the most important discovery about polarization control turned out to be stillness – if the cables were still the fringe contrast was high, if they were in motion, contrast was low. For the creation of the three-strand prototype, it was decided to simply let the cables dangle off the end of the optical table. Prior to clamping down the Fiber Collimator system end, the cables were held from their launcher end and all induced twists from the previously described tests were worked out by gently shaking the cable. The cables were then draped over the end of the table and clamped down at the Fiber Collimator end. A permanent twist in the teflon tubing caused the cable to gently curl under the optical table.

6.4 Three-Beam Interference

In Section 6.3, the two-beam proof of concept involved getting interference fringes using laser light only – in retrospect, a relatively straightforward task because of the long coherence length of the HeNe laser ($l_c > 30$cm). Getting the three-beam prototype to work involved a lot of alignment. The alignment tasks separate fairly neatly into four groups, superimposing the laser and white light input beams (Section 6.4.1), coupling laser (and later white) light into the optic strands (Section 6.4.2), collimating and creating the non-redundant pattern on the output of the strands (Section 6.4.3), and aligning the Spectrograph (Section 6.4.4). Some of the techniques to improve coupling efficiency are discussed in Section 6.3.2. Finally, the procedure used to find the white light zero path difference points is described in Section 6.4.5.

6.4.1 Alignment – Laser and White Light

A coarse alignment of the laser and white light sources was done in the conventional manner, both beams were projected onto the far wall of the laboratory and the main beam splitter and steering mirror were adjusted until the beams overlapped (Figure 3.10).

At this point, nothing further could be done until laser light was coupled into the strands. Once that was done (Section 6.4.2), the tilt adjustments and translation stage on the white light fold mirror (Figure 3.10) were adjusted until white light coupled into the optic strands as well. Due to the flexibility of the posts supporting the fold mirror, the coupling could not be optimized for both the laser and white light simultaneously. As a result, the X-Y position of the optic strand tip needed to be slightly readjusted when going between the sources.

6.4.2 Alignment – Launcher System

As described in Section 5.3.1, the lenses that focus the collimated beam onto the strand tip are mounted in a gimbal mount with adjustments for five of the six degrees of freedom (there is no provision for rotating the lens along the optical axis). In addition to nearly full freedom of motion with lens position, the tips of the optic strands are mounted in finely motorized X-Y positioners, where X and Y refer to the

axes perpendicular to the optical axis of the lens.

Figure 3.10 shows a schematic design of the layout. The Newport rails were laid out in a staggered pattern to partially compensate for the non-perpendicular phase center. The rails were fastened down, using the ends of the tie-down slots as a common reference. The optical elements which steer the light parallel to the rails were adjusted using the Fiber Launcher system components minus the motorized X-Y strand positioner. The gimballed lens mount was squared up using an aluminum plate clamped to the front of the Fiber Launcher I-beam and a set of machinist's calipers. With a lens installed, a target was placed at the focal point at the proper height and centered on the I-beam. Moving the Fiber Launcher between each end of the rail, the steering element was adjusted until the beam was parallel to the rail. At this point, the motorized X-Y strand positioners were reinstalled. Getting light to couple into the strands followed the technique outlined in Section 6.2

6.4.3 Alignment – Collimator System

The Fiber Collimator system was assembled to the state shown in Figure 5.4. "Output" 3, the output of "Telescope" 3, was chosen to be the reference for the optical axis. The four (clustered) screws which fasten *Fiber Collimator, Part 2C* to *Part 2B* (Figures C.18 and C.19) were tensioned to a point where *Part 2C* appeared parallel to *Part 2A* (Figure C.17). The Fiber Collimator system base was then squared up to the edge of the optical table. The horizontal axis perpendicular to the optical axis was adjusted to make the optical axis parallel to the edge of the optical table. The height of the beam was made parallel to the table surface by adjustment of the vertical axis. Finally, the focus of the lens was then adjusted to collimate the output beam.

A similar process was done for "Output" 1 and "Output" 2, only instead of using the table edge as a reference, "Output" 3 was used as the reference. At this point, it was noted that the three "Output" outputs were not quite colinear, and were canted at a slight angle. For construction of the prototype, it was decided that it was a minor effect. It did lead to some registration problems described in Section 6.4.4.

6.4.4 Alignment – Spectrograph System

The first issue of aligning the Spectrograph system involved choosing the axial plane of the imaging portion, which is to say, the axis of the achromat and two cylindrical elements. For the initial setup, the cylindrical elements were not inserted into the optical chain. Their presence would complicate matters by allowing too many more degrees of freedom. Next, the orientation and position of the prism and the Collimator system were mutually adjusted to steer the collimated laser beams correctly down the imaging optical axis. Quite a bit of iteration had to be done, because it was discovered that to first order, rotating the equilateral prism hardly steered the beam at all. Rotation affected the degree of dispersion (again, only moderately). To complicate matters a bit further, "Output" 1 was vignetted by the achromat mount when the plane of the output beams passed through the center of the achromat. As a result, the Collimator system assembly had to be moved perpendicular to the optical axis a slight amount to avoid the vignetting.

The proceedure for collimating the output beams outlined in Section 6.4.3 has its limitations. Because the diameters of the beams are so small ($\sim$ 3mm), diffraction, even over rather short distances of 5 m, becomes a dominant enough effect to make collimation difficult to do by projecting onto targets. The final collimation was done using a magnified image of the focused Airy spot (recall that the cylindrical elements are still out of the optical chain). Again using "Output" 3 as a reference, the focus point of the microscope objective was adjusted along with the focus point of the "Output" 3 collimation lens to optimize the quality of the Airy spot. Collimation of "Output" 2 and "Output" 1 was done adjusting only their respective collimation lenses, being very careful to leave the position of the microscope objective alone. However, prior to being able to perform the collimation tasks on the latter two "Outputs", the Airy spots had to be brought into the field of view defined by "Output" 3, and basically be made to overlap the "Output" 3 Airy spot. This was done by adjusting the axes of the collimation lenses perpendicular to the (Collimation system) optical axis which, to first order, moves the Airy spot in the image plane. In "Output" 2, following this superposition procedure resulted in an Airy spot of such poor image quality that it was decided to adjust the output angle of the optic strand tip by adjusting the screws linking *Fiber Collimator, Part 2B* and *Part 2C* (see Section 6.4.3), and at times pushing up or down on *Part 2C* to get angular adjustment

in that direction. Readjusting the position of the collimation lens then produced a more acceptable image.

At this point, the Airy spots of the three "Outputs" overlapped, and as an interesting side comment, fringes were formed across the Airy spots representing all the baselines. In fact, it was at this point that it was discovered that the remapped output array was not in a line. The baseline 3-2 fringes were slightly tilted with respect to the baseline 2-1 fringes. Relative tilt had to be introduced to "Output" 2 and "Output" 1 to overlap the Airy spots.

Finally, the cylindrical elements were inserted into the optical chain at near the correct point described in Section 3.5. The addition of extra glass in the path moved the focal point of the achromat further away. Because the placement of the negative cylindrical element is not as critical as the positive element, it received only a single axis of translation – horizontally across the optical axial plane. The positive cylindrical element received two axes of translation – across the optical axial plane and along it (the focus). The microscope objective could translate across the optical axial plane, giving one the ability to sample different portions of the spectrum. Each of the cylindrical elements was held by a mount which allowed minimal rotation ($\pm 5°$) of the element about an axis parallel to the optical axis of the achromat. This allowed the principal axes of the cylindrical elements to be lined up with the line of the remapped output array.

Reacquiring the focus involved going back to the reference, "Output" 3. After getting a rough focus with "Output" 3, with cylindrical elements that means concentrating as much light as possible into a line of light, the "focus" position of the microscope objective was fixed. All future adjustments to the focus were taken up by moving the positive cylindrical element. A typical iteration sequence consisted of adjusting the rotation on the negative cylindrical element to concentrate the light into a line as best as possible and then rotating the positive cylindrical element to get the line of light straight up and down again. Moving the image was done by adjusting the X and Y axes (*not* the collimation adjustment) of the collimation lens. Image motion in the horizontal direction could also be done by moving the positive cylindrical element along that axis. However, that moves all of the "Outputs" so it must be used with some care. It was at this point that it was discovered that the non-colinearity was a bit of a problem. Optimizing the cylindrical element orienta-

tion for the best overlap of two "Outputs" left the third too far off. Adjusting the collimation lens to compensate eventually led to a vignetting of the third "Output" when alignment was close. The solution to this problem, which led to very good laser fringes, was to split the difference. The cylindrical elements were carefully adjusted in rotation to have their principal axes vertical. Then, a spot in the image plane was chosen and each of the "Outputs" was adjusted to locate its image at that location. When one of the "Outputs" vignetted in the attempt, a different spot was chosen. The location of the "Output" image when it vignetted gave a good clue on where to locate the second trial location. This produced overlapping image lines on the third attempt. The cylindrical elements were then adjusted to tighten the image widths and get the image lines vertical. When white light was then coupled in the effect of the compromise was to have zones in the spectrum of good overlap and less-than-optimal overlap. However, as is shown in Section 6.4.5, the overlap was good enough to find the white light fringes.

6.4.5 Zero Path Point Search

As is shown in Figure 3.10, the extra distances from the beam splitter simulating "Telescope" 3 to the beam splitters simulating "Telescopes" 2 and 1 is compensated for by staggering the optical rails of the individual launchers. If everything else were equal, the zero path point should then be at similar fiducial marks on the respective optical rails. Inspection of Figure 5.4 makes it very clear that everything else was not equal. Figure C.21 was consulted to find the amount of offset at the Fiber Collimator system end and its effects were applied to fiducial settings on Fiber Launcher system end. The micrometers on "Telescope" 2 and "Telescope" 1 were set to the middle of their travel, the micrometer carriages were moved to the nearest millimeter, and the value was declared the center point of the zero path search space.

The CCD camera (described in Section 6.3) used for all adjustment involving laser light and two-beam data collection (see Figure 6.2) lacked the low light sensitivity for performing the white light zero path point search. A switch was made to an intensified detector. The detector is an Intensified Silicon Intensified Target (ISIT) detector, Model 66, built by Dage-MTI, Inc. (208 Wabash Street, Michigan City, Indiana 46360, USA) in 1984. The active detector area is approximately 13.0×10.0 mm (width×height) with a resolution of 400 scan lines at the center and 350 scan lines

at the corners. It was originally purchased for the CHARA Speckle Interferometry program (McAlister et al. 1987) but proved to be inadequate to the task of dealing with atmospherically degraded images because of the inability to gate the active detector time to the atmospheric coherence time, about half of the RS-170 video frame time. The ISIT camera is equipped with two controls, one to control the voltage of the intensifier gain and the other control the video output appearance. In practice the controls work much like the "brightness" and "contrast" controls on a typical computer monitor. Walker (1987) describes the physics of ISIT type detectors (and many others).

The white light spectrum was centered up on the ISIT detector and the search was underway. The first baseline searched was the 2-3 baseline, "Telescope" 3 as usual being the reference. The search procedure consisted first of retracting fully the micrometer on the Fiber Launcher. The micrometer was then stepped forward by hand, waiting several seconds between steps for any oscillation set up in the dangling cables to damp out. The micrometer was always driven in the forward direction (pushing the I-beam away from the micrometer). It was found that when the springs were being extended, the I-beam was less likely to find a bi-stable point along the rail. Based on the estimate of the effective spectral resolution of the Spectrograph, the step size could have been as large as 0.050 mm with confidence of not stepping past the zero point without detection. The step size was set conservatively at 0.025 mm, the main reason being the difficulty of maintaining a consistent step size. After the full 12.7 mm of the micrometer was traversed, the fiducial on the rail was reset forward 10 mm (giving 2.7 mm of overlap), the micrometer fully retracted, and process repeated. The search space was to have been (using the default carriage setting as the reference point): +0 mm, +10 mm, -10 mm, -20 mm, +20 mm, +30 mm, -30 mm, etc. The baseline 2-3 zero path point was found in the +0 mm search while that for baseline 1-2 was found in the -20 mm search. White light fringes corresponding to baseline 3-1 were not found. It is suspected that the main effect hampering detection is differential dispersion. A simplified analysis follows in Section 6.5.2.

6.5 Data Analysis

6.5.1 Reduction

Data were taken of the spectrum in several wavelength bands with all the permutations of two and three telescopes. A bias frame was created by preventing all three "Telescopes" from launching into their respective strands. All light incident upon the detector was backgroud illumination which was expected to be the same for all frames. Seven frames were averaged to create a smooth bias frame. Flat frames were created by allowing each of the three "Telescopes" to individually illuminate the detector. From these frames, four flat frames were created, the first using the frames from all three "Telescopes", the second using the frames from "Telescope" 3 and "Telescope" 2, the third using the frames from "Telescope" 2 and "Telescope" 1, and the last using "Telescope" 3 and "Telescope" 1. In each set of flat frames, the data from the "Telescopes" in question was taken individually and coadded. There were no fringes in the flat frames. In calculating each flat frame, a strip 87 columns wide on the far left and 72 columns wide on the far right were masked off and not used in the calculation of the flat field. These columns were set to one in the final flat frames.

A typical white light data frame from all three "Telescopes" simultaneously is shown in Figure 6.3. Along the bottom of the figure are tick marks with labels. These numbers are an approximate wavelength calibration (in nm) of the spectrum. The 540 nm, 580 nm, and 620 nm positions were located using three different narrow-band interference filters. The full-width half-maxima (FWHM) of these filters were 10 nm, 9 nm, and 10 nm, respectively. The 633 nm label corresponds to the HeNe laser. Figure 6.4 shows a typical raw image from the HeNe laser.

The spatial frequencies of the baselines were obtained using the power spectrum. Specifically, all relevent frames were broken up into columns. If the column intersected the spectrum and contained no negative or zero values, the column (480 data points) was imbedded within a data string 2048 data points long, with the extra points set to the average value of the column, and the power spectrum of the data string was calculated. The individual power spectra were then co-added in Fourier space and the results plotted. The power spectrum of the laser baselines is shown in Figure 6.5. Figure 6.6 is the power spectrum of the all three baselines in unfiltered

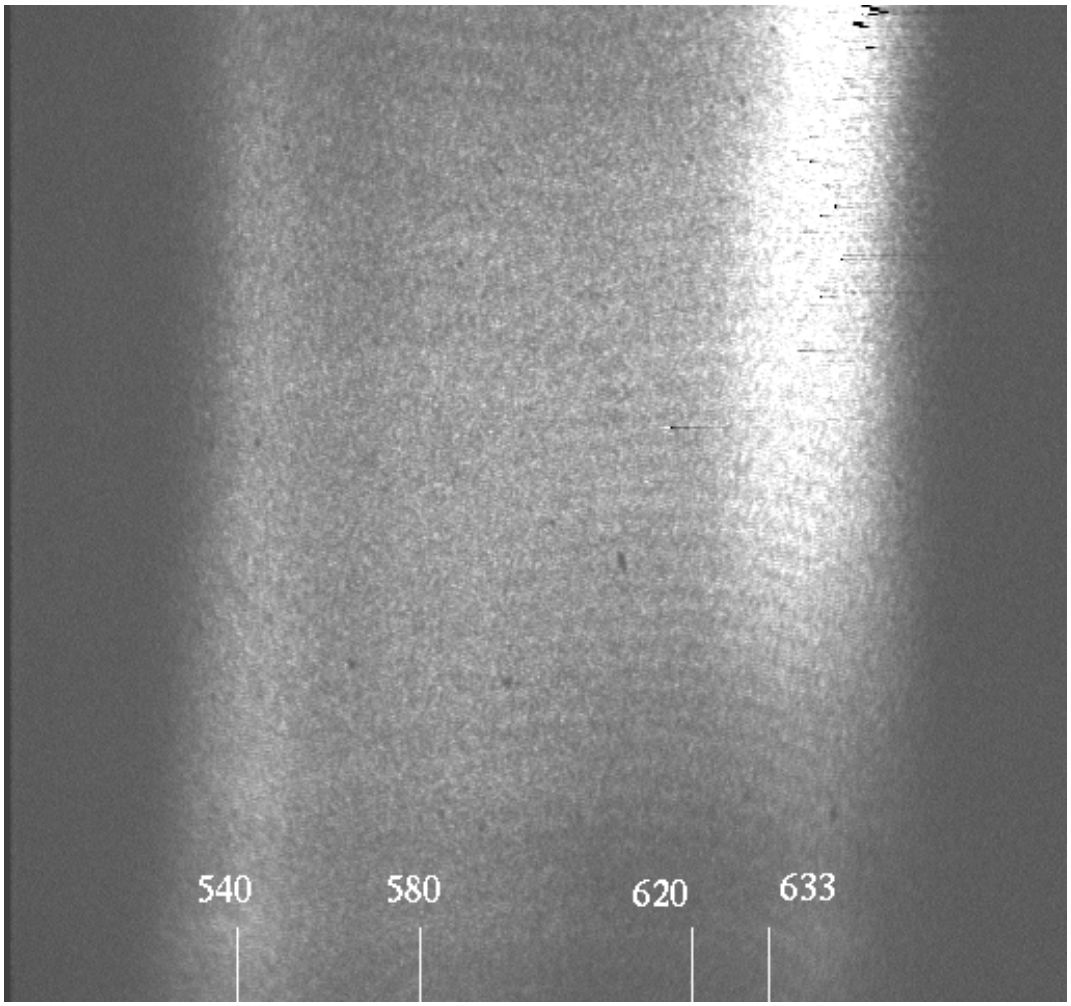

Figure 6.3: A typical data frame, unfiltered, before applying the bias and flat frames. The numbers along the bottom are approximate wavelength values in nm – no effort was made to calibrate the non-linear dispersion characteristics of the prism. The dark few columns on the far left are residual sync errors between the ISIT output and the frame digitizer. The horizontal dark streaks within the bright area in the upper right are artifacts of the ISIT intensification method at saturation. The baseline 2-3 fringes can be seen best at about 620 nm, halfway down in the frame.

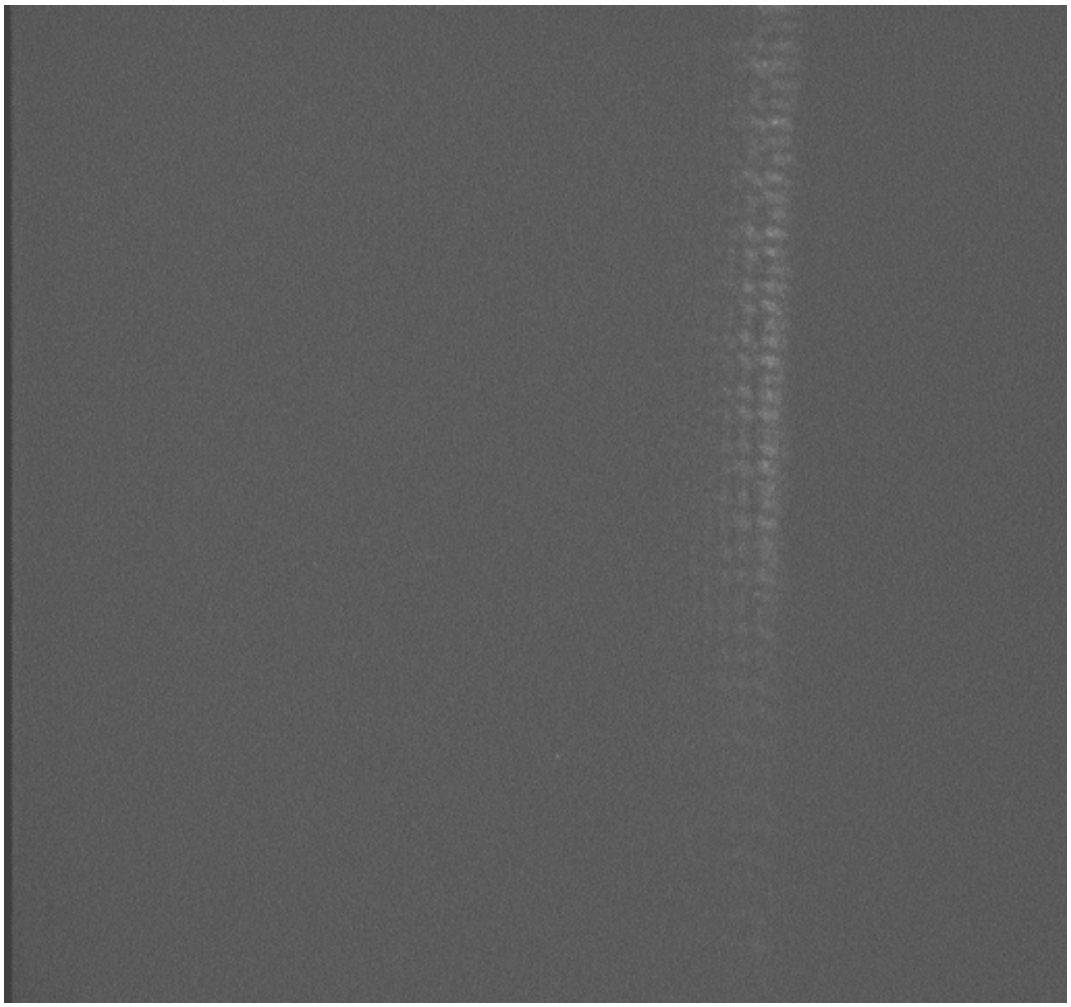

Figure 6.4: A typical data frame of the HeNe laser, before applying the bias and flat frames. Note that there is a set of higher frequency fringes not visible in Figure 6.3.

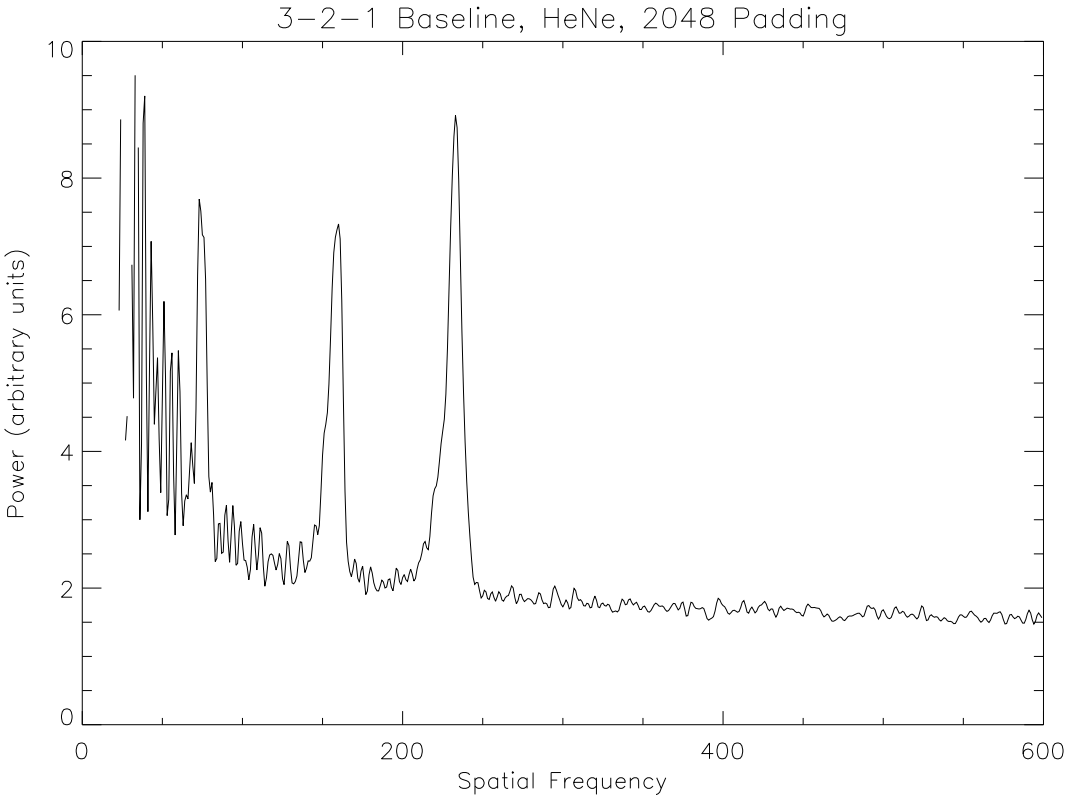

Figure 6.5: The power spectrum of the HeNe laser data. The relevent data (480 points) was imbedded within a data string 2048 data points long, where the extra padding was set to the average of the data set. Note the three peaks at about 75, 160, and 230.

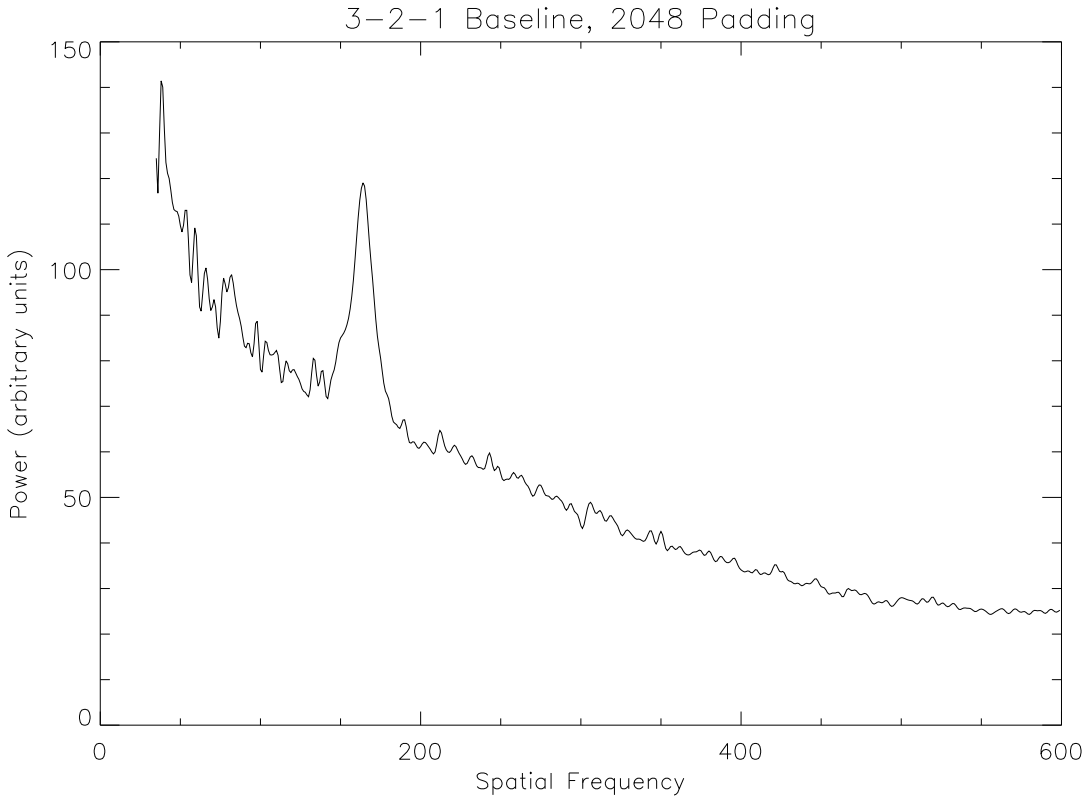

Figure 6.6: The power spectrum of the unfiltered white light data. The padding technique is described in the text and in the caption to Figure 6.5. Note that even though detector has light illuminating it from each of the "Telescopes", only the two lowest frequency baselines show up above the noise.

white light. Note in this case that only two of the three baselines are evident, at about 75 and 160 in the spatial frequency units. Figures 6.7, 6.8, and 6.9 show the power spectra of 3-2 baseline, 2-1 baseline, and 3-1 baseline respectively without the light of the other "Telescope" to add the extra two baselines. In the case of the 2-1 baseline, removing "Telescope" 3 from the data makes the peak near 75 more evident.

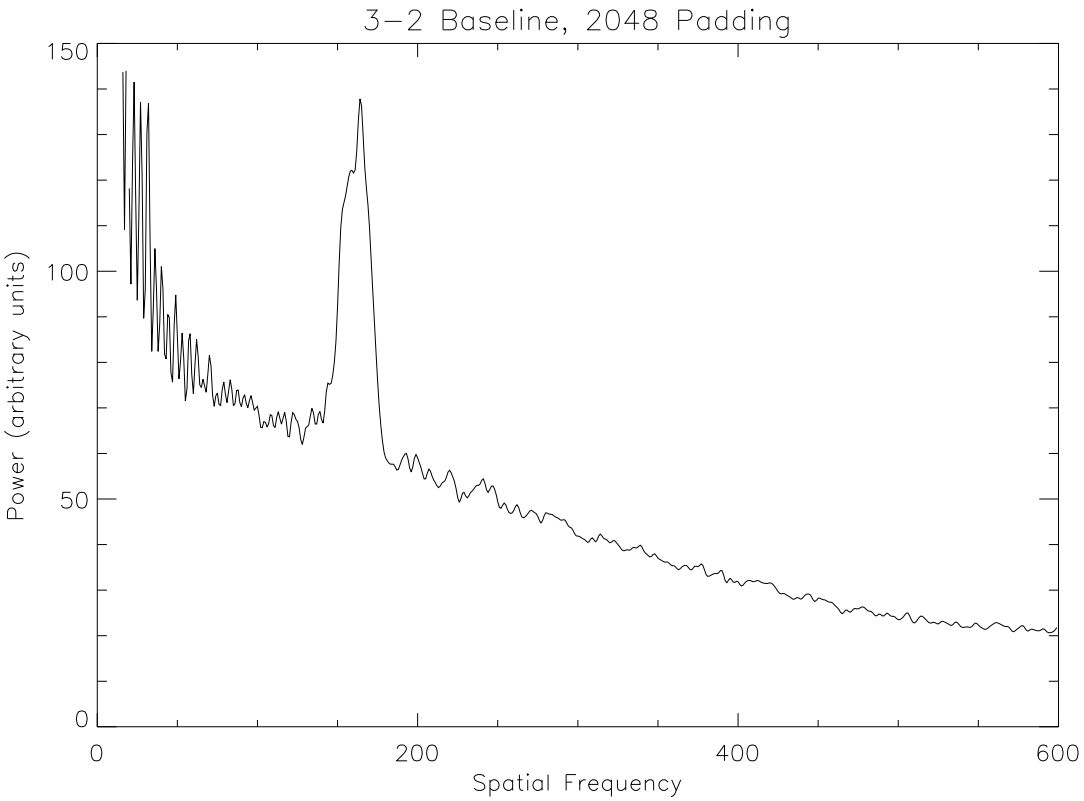

Figure 6.7: The power spectrum of the unfiltered white light data. The padding technique is described in the text and in the caption to Figure 6.5. This is data for the 3-2 baseline only.

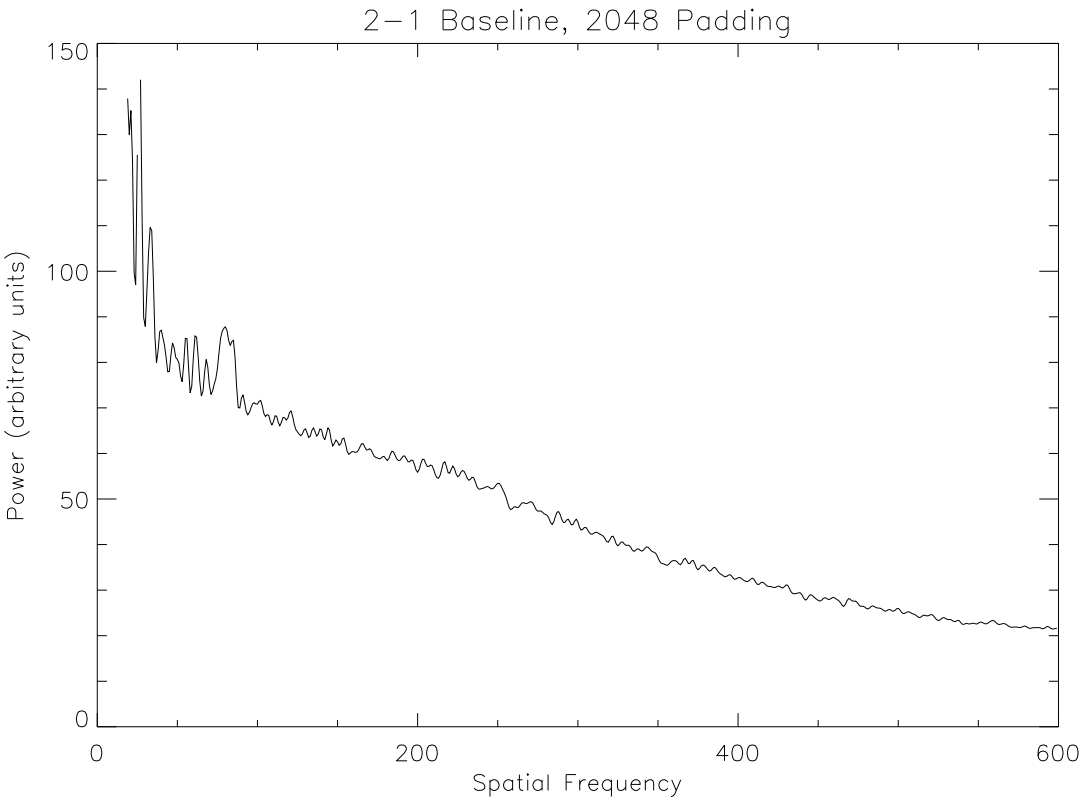

Figure 6.8: The power spectrum of the unfiltered white light data. The padding technique is described in the text and in the caption to Figure 6.5. This is data for the 2-1 baseline only.

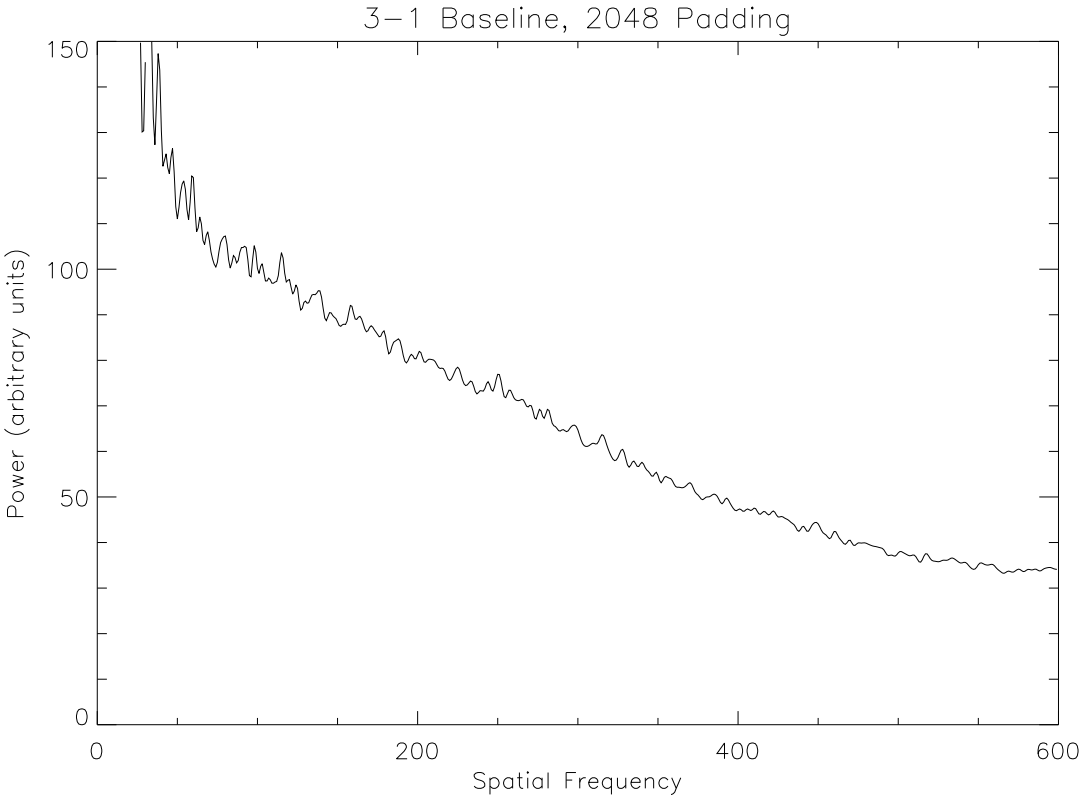

Figure 6.9: The power spectrum of the unfiltered white light data. The padding technique is described in the text and in the caption to Figure 6.5. This is data for the 3-1 baseline only. Note the absence of an obvious peak. See Section 6.5.2 for an explanation.

6.5.2 Interpretation

As was noted in Section 6.4.5, white light fringes were not found for the 3-1 baseline. It is suspected that differential dispersion, arising from differing strand lengths, prevented detection of the highest frequency baseline in the white light images. Recall from equation 1.8,

$$I(w) = 1 + V(w)\cos(2\pi w\mathcal{D}(w)), \tag{6.1}$$

that the path length difference between the arms of the interferometer (in this case, the internal channels of the imager) is wavenumber dependent. In the case here, there are only two media to worry about, glass and air. In this case, $\mathcal{D}(w)$ can be written as,

$$\mathcal{D}(w) = s_a n_a(w) + s_g n_g(w),$$

where s_a and s_g are the path length differences between the channels of air and glass media respectively, while $n_a(w)$ and $n_g(w)$ are the corresponding (wavenumber dependent) indices of refraction. To be able to calculate the effect of a finite bandpass, as in Section 1.1.1, it is convenient to expand the argument of the cosine function in equation 6.1 in terms of a Taylor series, keeping only terms of the order of $w - w_0$.

Let

$$\begin{aligned} H(w) &= 2\pi w\mathcal{D}(w) \\ &= 2\pi w[s_a n_a(w) + s_g n_g(w)], \end{aligned}$$

and consequently,

$$\frac{dH(w)}{dw} = 2\pi[s_a n_a(w) + s_g n_g(w) + w s_a n_a'(w) + w s_g n_g'(w)].$$

The Taylor expansion about w_0 is approximated as

$$H(w) \simeq H(w_0) + (w - w_0)\frac{dH(w)}{dw}\Big|_{w_0}.$$

Allowing the following substitutions (for notational simplification),

$$\begin{aligned} F &= H(w_0) \\ &= 2\pi w[s_a n_a(w_0) + s_g n_g(w_0)], \\ G &= \frac{dH(w)}{dw}\Big|_{w_0}, \\ &= 2\pi[s_a n_a(w_0) + s_g n_g(w_0) + w_0 s_a n'_a(w_0) + w_0 s_g n'_g(w_0)], \end{aligned}$$

and

$$\alpha = w - w_0,$$

the effect of the finite bandpass, including dispersion, is given as,

$$\begin{aligned} I(w_0, \Delta w) &= \frac{1}{\Delta w}\int_{w_0-\Delta w/2}^{w_0+\Delta w/2}\Big[1 + V(w)\cos(H(w))\Big]dw \\ &\simeq 1 + \frac{V(w_0)}{\Delta w}\int_{-\Delta w/2}^{\Delta w/2}\cos(F + G\alpha)d\alpha \\ &\simeq 1 + V(w_0)\frac{\sin\Big(\frac{G}{2}\Delta w\Big)}{\Big(\frac{G}{2}\Delta w\Big)}\cos(F). \end{aligned} \tag{6.2}$$

In the process of finding the zero path point, the path was adjusted until the contrast in the fringes was the greatest. Because F is on the order of 150 times larger than $\frac{G}{2}\Delta w$ in equation 6.2, $\cos(F)$ is not the significant influence on the coefficient of $V(w_0)$. Adjusting for high contrast was, in effect, setting $\frac{G}{2}\Delta w$ to zero,

$$\frac{G}{2}\Delta w = \pi\Delta w\Big[s_a\Big(n_a(w_0) + w_0 n'_a(w_0)\Big) + s_g\Big(n_g(w_0) + w_0 n'_g(w_0)\Big)\Big], \tag{6.3}$$

$$s_a\Big(n_a(w_0) + w_0 n'_a(w_0)\Big) = -s_g\Big(n_g(w_0) + w_0 n'_g(w_0)\Big)\Big],$$

$$s_g = -\frac{n_a(w_0) + w_0 n'_a(w_0)}{n_g(w_0) + w_0 n'_g(w_0)}s_a. \tag{6.4}$$

In the experiment, differential air paths between the channels were roughly determined. It was found that "Telescope" 1 had about 18800 μm more air path than

"Telescope" 3, which in turn had 4400 μm more air path than "Telescope" 2. Putting variable indices on these numbers (and being very careful about the signs), one gets,

$$s_{a12} = 23200\mu\text{m},$$
$$s_{a23} = -4400\mu\text{m},$$

and

$$s_{a31} = -18800\mu\text{m}.$$

Empirically, the fringes were visible over a path length envelope of about 50 μm, and as a result, $\Delta w \simeq 0.02\mu\text{m}^{-1}$. From inspection of the spectrum visible with the ISIT detector, the central wavelength was about 596 nm, resulting in a central wavenumber of $w_0 \simeq 1.6779\mu\text{m}^{-1}$. Dispersion coefficients were not available for the core glass of the optical strand, so it was approximated by BK7 glass, giving values of the index and the derivative of the index of $n_g(w_0) = 1.52$ and $n'_g(w_0) = 0.015\mu\text{m}^{-1}$, respectively. The respective values for air were $n_a(w_0) = 1.0003$ and $n'_g(w_0) = 5.4 \times 10^{-6}\mu\text{m}^{-1}$, completing the constants required for evaluation.

From equation 6.4, the path difference due to glass can be found in two of the baselines and determined for the third,

$$s_{g12} = -15019\mu\text{m},$$
$$s_{g23} = 2848\mu\text{m},$$

and

$$\begin{aligned} s_{g31} &= -(s_{g12} - s_{g23}) \\ &= 12171\mu\text{m}. \end{aligned}$$

At this point, s_{g31} and s_{a31} are already defined – there are no path lengths one can adjust in the 1-3 baseline without out altering the values in the 1-2 and 2-3 baselines. Any amount that $\frac{G}{2}\Delta w$ differs from zero is a fundamental problem. Inserting these

results into equation 6.3,

$$\begin{aligned}\left(\frac{G}{2}\Delta w\right)_{31} &= \pi(0.02)\Big[(-18800)(1.0003)+(12171)(1.55)\Big] \\ &= 3.7,\end{aligned}$$

and the coefficient of $V(w_0)$ becomes 0.14. As can be seen here, the dispersion has reduced the contrast to 14% of the initial fringe contrast. It should be noted here that although one might be able to detect fringe visibilities of 0.14, the actual contrast value is probably lower. First of all, the dispersion characteristics were approximated by BK7 glass. BK7 has only a moderate dispersion compared to most glasses available. The core glass probably has a higher dispersion coefficient. Finally, it was noted that the visibility coefficient was very sensitive to the dispersion coefficient, a sensitivity amplified by the differential glass path. In light of this, it is very important to get the lengths of the fiber optic strands as close to the same as possible.

One final observation addresses the width of the white light peaks with respect to the laser peaks. Because of the weak signal strengths within the white light data, and a limited ability to collect data, peak strengths were boosted by using the whole spectrum. Since the fringe frequency is wavelength dependent, this process incurred the penalty of broader peaks. In practice, this can be overcome by using just a portion of the spectrum but many frames.

Chapter 7

The Prototype Imager in the CHARA Array

Prototype devices enable one to discover, prior to large investments of time and money in design, where the critical components are in a concept. This prototype imager pointed out a number of places where more care must be taken in construction. While the prototype as a whole cannot be used in its present iteration (it is too difficult to align), parts of it can be used. However, there are a few other issues that must be dealt with to get scientifically useful data, the intensity of each frame of data must be individually calibrated. This chapter concludes with a discussion of the anticipated observing procedure.

7.1 Intensity Calibration

In coupling starlight to fiber optic strands, one has to deal with turbulence. Even though the interferometer has a tip-tilt system in operation to keep the bright spot in the speckle pattern centered on the strand tip, the atmosphere introduces higher order degradation of the image (Section 4.3.4). Due to turbulence, the effective mode profile of the incoming starlight changes with respect to the mode profile of the strand (Shaklan and Roddier 1988), and as a result, the intensity of light coupled changes. To get accurate photometric information, the intensity must be calibrated.

In building FLUOR (Coudé du Foresto and Ridgway 1992), this issue came up. It was solved by splitting the light from each of the two telescopes into two beams

(for a total of four output beams) using an single directional coupler. One of the output beams from each of the telescopes is used for intensity monitoring, while the other two are sent through a bi-directional coupler for visibility measurements.

Something similar will have to be done with the CHARA Array imager. Each of the "Telescopes" will have an single directional coupler which will siphon off 10% of the light to use for intensity calibration. As a result, the polishing procedure described in Sections 5.2.1 and 5.2.2 will only apply to one end of each strand. The other will have to be prepared for connection to a single directional coupler. It is hoped that a commercial cable with one end already prepared for connection to the coupler can be bought, and a polishing process similar to that in Chapter 5 can be done.

7.2 Hypothetical Observing Procedure

With intensity calibration in place, using the imager would be relatively straightforward. The procedure would be something like the following. One would first have to make sure that the phase centers of the fringe tracking system correspond to the phase centers of the imaging system. One would use the common white light autocollimation system of the interferometer as a whole and move the "Telescope" launch points to compensate. Most likely, once a calibration star is acquired and the fringe tracking system locked, a bit more adjustment would be required of the launch points. At this time, the "Mickey Mouse ears" would be adjusted to equalize the polarizations and maximize the fringe constrast (Coudé du Foresto et al. 1996).

At this point, the imager is ready for target data. Once the target is acquired and locked, The detector collects its data in large sequences of short exposures, short enough to freeze the seeing and therefore have fringes of each baseline simultaneously. The exposure time would be adjusted according to the brightness of the object, seeing conditions, position in the sky, and probably some other factors that have not been forseen. An estimate of the exposure time is about 15 milliseconds, corresponding to the atmospheric "boiling" time at 600 nm. At the same time, the intensity calibrators would be collecting data. The detector and intensity calibrators will be synchronized in some way and the intensity calibration will probably be an automatic step in the reduction process.

At some point the sequence of short exposures would be "finished", and a new sequence would be started. The detector is not actually stopping, the exposures are merely binned differently. Because the Earth is in rotation, at some point the ellipse drawn out in the *uv* plane will be too different from a point to give accurate results. This effect is known as *baseline smearing*. Subsequent data goes into the calculation of the next "point" in the *uv* plane. Once acceptable coverage in the *uv* plane is attained, the complex visibilities (or phase closures) can be Fourier inverted to create the image.

Chapter 8

Summary and Conclusion

8.1 Critical Summary

It became clear during the alignment of the Collimator system that translation stages that rely on a tenon moving within a mortice are not appropriate in a precision alignment situation. For the stages to function at all, a small bit of play has to be included. This play leads to bistable points during alignment and significantly couples the adjustment axes. For the imager used in the CHARA Array, it is recommended that commercial translation stages employing pre-loaded bearings rolling in a way track be used. The staggered pattern shown in Figure 5.4 will have to be increased. In addition, the strand tip clamp will have to be modified to allow a closer packing.

Dispersion is a very detrimental effect. In the production version of the imager, extreme care will have to be taken to ensure that the optic strand lengths are as close to equal as possible. By building all the strands in parallel fashion will go far in getting the lengths equal. Strand length equality is further complicated by the needs of intensity calibration, discussed in Section 7.1, where one end of the strand has to be modularized to connect to a standard fiber coupler.

The most critical task to investigate prior to incorporation into the Array is development of the intensity calibration system. Procedures will have to be developed that insure strand lengths to rather tight tolerances, while still allowing modularity. In addition, a unified control system will need to be developed that controls the detector and intensity calibration systems, keeping them synchronized with each other.

8.2 Conclusion

In conclusion, using single-mode fiber optic strands as a beam transfer system within an instrument allows one to use smaller, "off-the-shelf" optics, which are less expensive and tend to be of higher average quality than the larger, custom alternatives. Added difficulty in construction and alignment is made up for in the high quality of interfered wavefronts intrinsic to single-mode strands. The imager has the advantage of being completely passive, collecting data at all available baselines and phase closures without any moving parts. Apart from temperature changes and instrument settling, internal adjustments (after initial alignment) will be minimal.

The prototype fulfilled its duty of shedding light on potential trouble spots in development. In summary, it is *very* critical that the lengths of the single-mode strands be very close to the same length. It might even be worthwhile to develop a test interferometer for use during polishing that can measure dispersion, and hence length difference, to use as polishing feedback. Alignment is also important. One needs to be able to adjust more parameters than was originally thought. Among these are angular adjustments for the strand tips within the Fiber Collimator system. With these modifications, a very successful imager could be built for the CHARA Array.

Appendix A

Systems Listing

Listed here is a complete parts listing of each of the three systems as well as a parts listing for optic strand polishing. Column three of each of the tables that follow is the source for the item in question. All but two of the codes, *built* and *GSU*, can be found in the vendor listing in Appendix B. *GSU* indicates that the item was found in the Georgia State University, Department of Physics and Astronomy facilities while *built* indicates that the part was machined. Column four gives a reference or stock number in the vendor's catalog.

A.1 Launcher System

Qnty	Item	Source	Reference
3	Precision Optical Rail	Newport	PRL-24
8	Precision Rail Carriage	Newport	PRC-3
3	*Part 1A*	built	
3	*Part 1B*	built	
3	*Part 1C*	built	
3	*Part 1D*	built	
66	1/4-20×1/2" Socket Cap Screw	MSC	05520051
3	5-Axis Gimbal Optic Mount	Newport	LP-2
3	*Part 5A*	built	
3	Precision Optimized Achromat 120 mm f.l.	MG	01LAO138
3	X-Y Fiber Positioner	NewFocus	8051
1	Economical Multi-Axis Driver	NewFocus	8801
1	Control Pad	NewFocus	8620
3	*Part 4A*	built	
3	*Part 4B*	built	
3	*Part 4C*	built	
6	8-32×3/4" Socket Cap Screw	MSC	05507074
3	2-56×3/16" Nylon Set Screw	SmallParts	E-SSN-256-3
8	*Part 2A*	built	
8	8-32×1-1/4" Socket Cap Screw	MSC	05507124
4	3" extension spring	GSU	
2	5/16-18×1/2" Hex Cap Screw	MSC	67433201
2	*Part 3A*	built	
2	Starrett Micrometer Head	Ziegler	T463P
2	Starrett Ball Attachment	Ziegler	247C
2	8-32×3/4" Socket Cap Screw	MSC	05507074

A.2 Collimator System

Qnty	Item	Source	Reference
2	Sliding Base	Newport	B-1
2	Post Holder	Newport	VPH-2
2	Support Post	Newport	SP-2
2	1/4-20×1/2" Socket Cap Screw	MSC	05520051
1	*Part 3A*	built	
12	#8 SAE Flat Steel Washer	MSC	67746446
12	8-32×3/4" Socket Cap Screw	MSC	05507074
3	*Part 2A*	built	
3	*Part 2B*	built	
3	*Part 2C*	built	
3	*Part 2D*	built	
54	6-32×3/4" Flat Head Screw	MSC	67566844
12	6-32×1/4" Flat Head Screw	MSC	67566687
3	2-56×3/16" Nylon Set Screw	SmallParts	E-SSN-256-3
3	*Part 1A*	built	
3	*Part 1B*	built	
3	*Part 1C*	built	
3	*Part 1D*	built	
3	*Part 1E*	built	
3	*Part 1F*	built	
9	Vlier Steel Spring Plunger	MSC	62119193
9	2-56×3/8" Stainless Set Screw	MSC	67265165
15	8-32×3/8" Hex Machine Screw	MSC	67424085
3	M4×0.7×8 mm Hex Cap Screw	MSC	67442640
6	8-32 Hex Machine Screw Nut	MSC	87921292
12	#8 Nylon Washer	MSC	67353409
3	6 mm Lens Mount	Newport	LH-25
3	Precision Optimized Achromat 10 mm f.l.	MG	01LAO001

A.3 Spectrograph System

Qnty	Item	Source	Reference
3	Sliding Base	Newport	B-2
3	Post Holder	Newport	VPH-2
1	Support Post	Newport	SP-2
7	1/4-20×1/2" Socket Cap Screw	MSC	05520051
1	Prism Table	Newport	PT-1
1	Equilateral Dispersing Prism	MG	01PES011
2	Support Post	Newport	SP-1
1	Self-Centering Lens Mount	Newport	LCM-2
3	Precision Optimized Achromat 400 mm f.l.	MG	01LAO333
2	Alumnium Single-Axis Stage	Newport	460A-X
2	*Part 2A*	built	
2	*Part 2B*	built	
8	6-32×3/4" Flat Head Screw	MSC	67566844
4	8-32×1/2" Thumb Screw	MSC	67388645
2	Adjustable Cylindrical Lens Holder	MG	07LHC013
1	Precision Plano-Cylindrical Glass Lens	MG	01LCN144
1	Aluminum Multi-Axis Stage	Newport	460A-XY
1	Precision Plano-Cylindrical Glass Lens	MG	01LCP125
2	1/4-20×3/4" Socket Cap Screw	MSC	05520077
1	Microscope Objective Mount	Newport	LH-MU
1	40× Microscope Objective	Newport	M-40X

A.4 Fiber Optic Strand Creation

Qnty	Item	Source	Reference
1	Type 304W Stainless Hypodermic Tubing	SmallParts	E-HTX-24-12
1	353ND Epoxy Resin	Epo-Tek	353ND-A
1	353ND Epoxy Hardener	Epo-Tek	353ND-B
1	3.8 μm Core Single-Mode Fiber Optic	Newport	F-SV-20
1	15 Gauge Teflon Tubing	SmallParts	E-SWTT-15-50
1	*Jig 1A*	built	
1	*Jig 1B*	built	
1	4-40×1/8" Stainless Set Screw	SmallParts	E-SSX-440/2
1	Starrett Pin Vise	Ziegler	162A
1	60 μm Grit Alumnium Oxide Abrasive	Moyco	LPA-600
1	30 μm Grit Alumnium Oxide Abrasive	Moyco	LPA-600
1	12 μm Grit Alumnium Oxide Abrasive	Moyco	LPA-600
1	5 μm Grit Alumnium Oxide Abrasive	Moyco	LPA-600
1	3 μm Grit Alumnium Oxide Abrasive	Moyco	LPA-600
1	1 μm Grit Alumnium Oxide Abrasive	Moyco	LPA-600
1	0.3 μm Grit Alumnium Oxide Abrasive	Moyco	LPA-600
1	Fibrmet Polishing Extender	Buehler	69-3080-032
1	*Jig 2A*	built	
1	AO Spencer Microscope	GSU	

Appendix B

Hardware Vendors

This is a list of all the hardware vendors that were used to purchase tools and components for assembly of the prototype. Not included in this listing is a supplier of the raw materials for the machining tasks. In machining parts for the prototype, all of the pieces were small and used no exotic metals. As a result, the Physics and Astronomy shop at Georgia State University had scrap pieces at hand. The *Key* column in the tables below correspond to the vendor key in Appendix A.

Key	Vendor	Note
Buehler	Buehler Limited 41 Waukegan Rd Lake Bluff, Illinois 60044 800-283-4537 FAX: 708-295-7979	Supplier of fiber optic polishing products.
Epo-Tek	Epoxy Technology Incorporated 14 Fortune Dr Billerca, Massachusetts 01821	Supplier of zero-shrink epoxies.
MG	Melles Griot 1770 Kettering St Irvine, California 92614 800-835-2626 FAX: 714-261-7790 http://www.mellesgriot.com	Supplier of generic optics, and optical components.
MSC	MSC Industrial Supply Company 6700 Discovery Blvd Mableton, Georgia 30126 800-944-9803 FAX: 800-255-5067 http://www.mscdirect.com	Has many locations throughout the United States.

Key	Vendor	Note
Moyco	Moyco Precision Coated Abrasives 200 Commerce Dr Montgomeryville, Pennsylvania 18936	
NewFocus	New Focus, Incorporated 2630 Walsh Ave Santa Clara, California 95051-0905 408-980-8088 FAX: 408-980-8883 http://www.newfocus.com	Supplier of clever mounts and motorized components.
Newport	Newport Corporation 1791 Deere Ave Irvine, California 92714 800-222-6440 FAX: 714-253-1680 http://www.newport.com	Supplier of generic optics and optical components.
SmallParts	Small Parts Incorporated 13980 Northwest 58th Ct Miami Lakes, Florida 33014-0650 800-220-4242 FAX: 800-423-9009	Supplier of small parts (big surprise!) – tubing, screws, bearings, etc.
Ziegler	Ziegler Tools 711 Marietta St Northwest Atlanta, Georgia 30313	Distributor of Starrett products.

Appendix C

Mechanical Drawings

The mechanical drawings are divided into four groups – the Launcher system, the Collimator system, the Spectrograph system, and the Jigs. Individual system drawings are organized through the use of three parameters – the system designation, the assembly number, and the part letter. Jig drawings are organized with two parameters, the jig name and part letter. The numbering and lettering of the assemblies and parts is somewhat arbitrary – reflecting more the order in which they were conceived and created than some overall unification plan. These drawings refer only to parts created in the GSU Physics & Astronomy machine shop by the author. Parts purchased for the various systems are documented in Appendix A. Commercial sources for these parts are documented in Appendix B.

C.1 Fiber Launcher System

The Launcher system has five assemblies. Assembly 1 has four parts, Assembly 2 one part, Assembly 3 one part, Assembly 4 three parts, and Assembly 5 one part. Three copies of each of the Assembly 1, Assembly 4, and Assembly 5 parts were built. Eight copies of the Assembly 2 part were built. Two copies of the Assembly 3 part were built. These are listed in the following pages and complete this section.

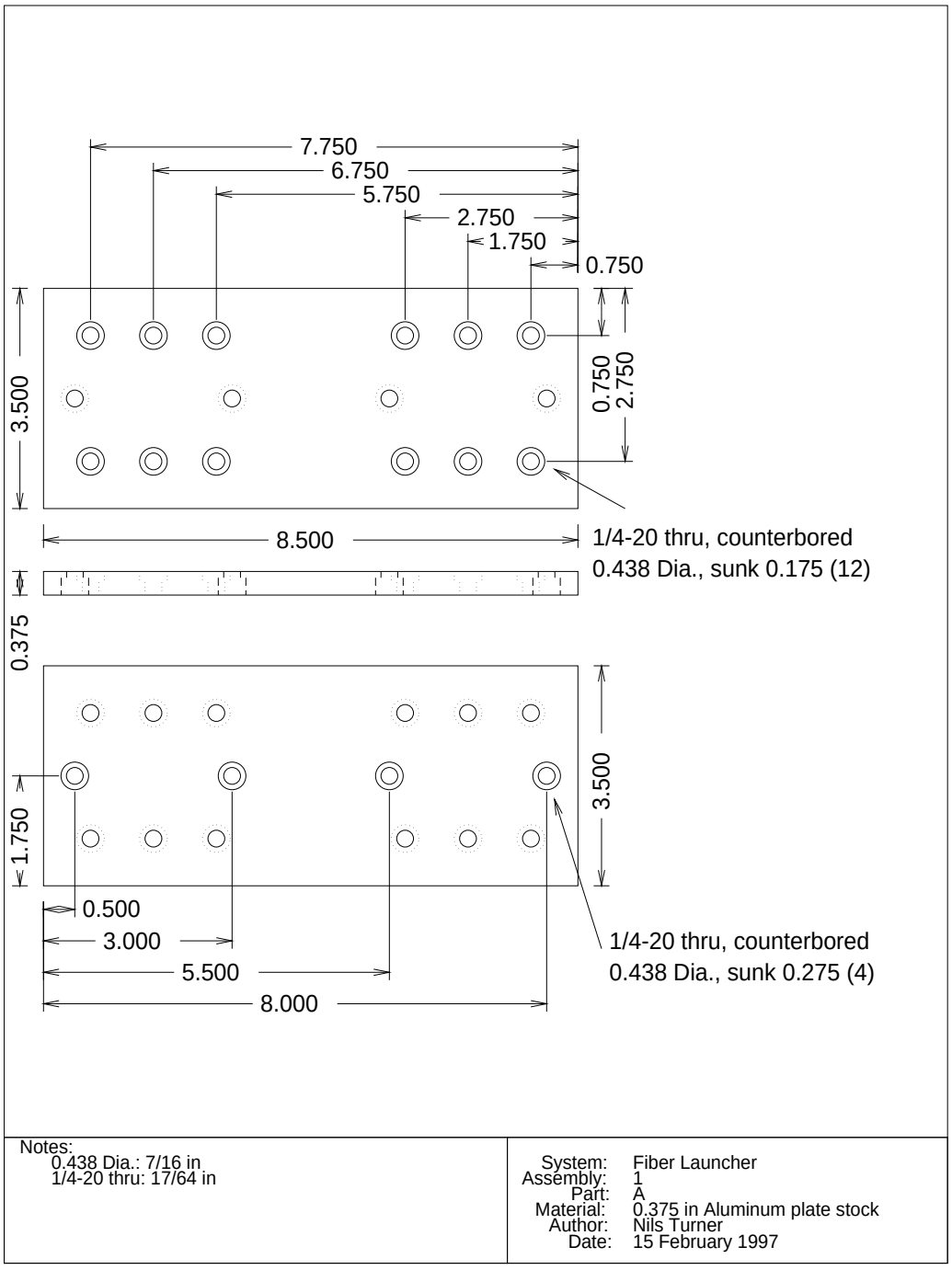

Figure C.1: *Fiber Launcher, Part 1A*. This part is the bottom plate of the I-beam referred to in Section 5.3.1.

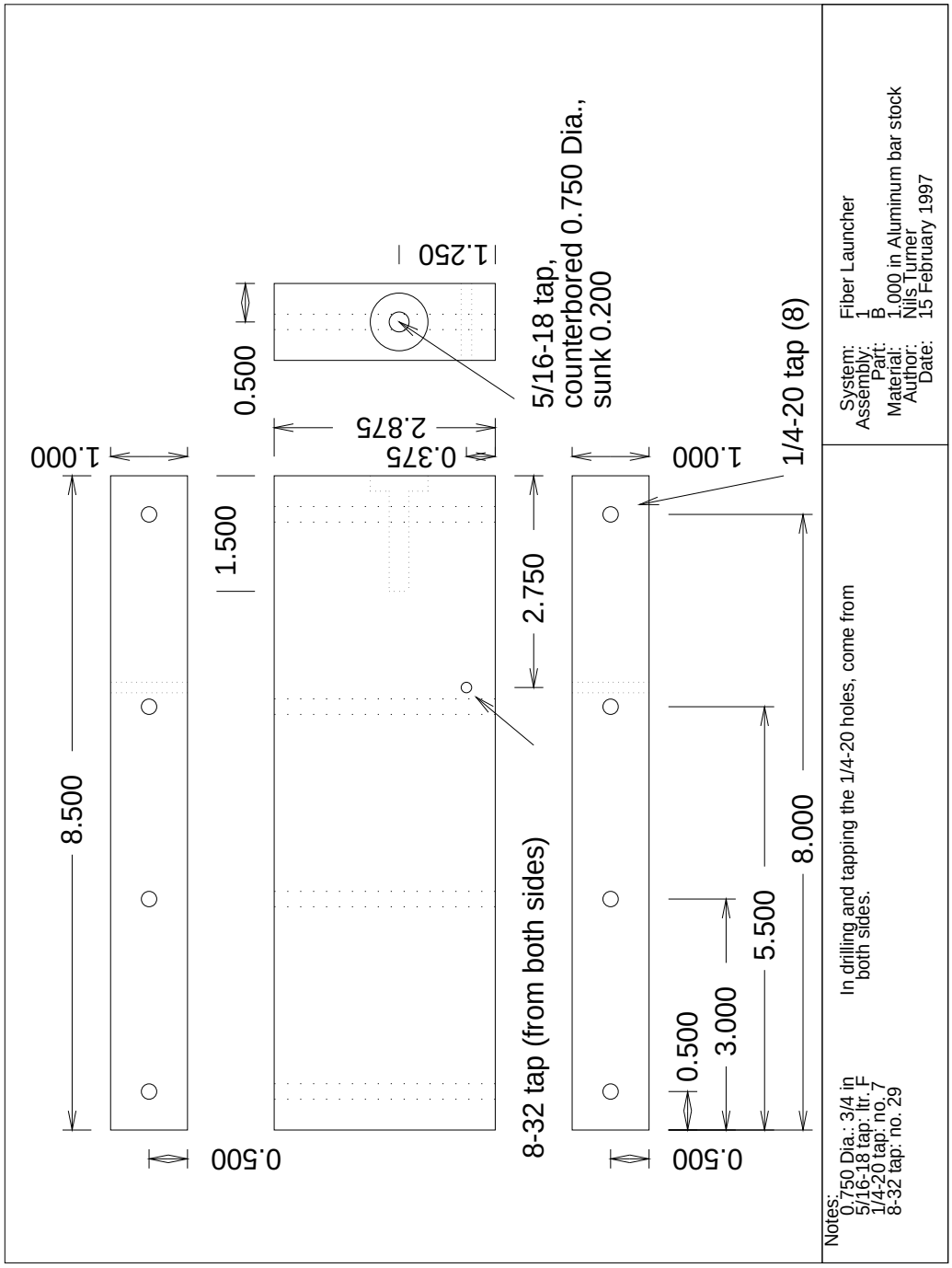

Figure C.2: *Fiber Launcher, Part 1B.* This part is the vertical member of the I-beam referred to in Section 5.3.1.

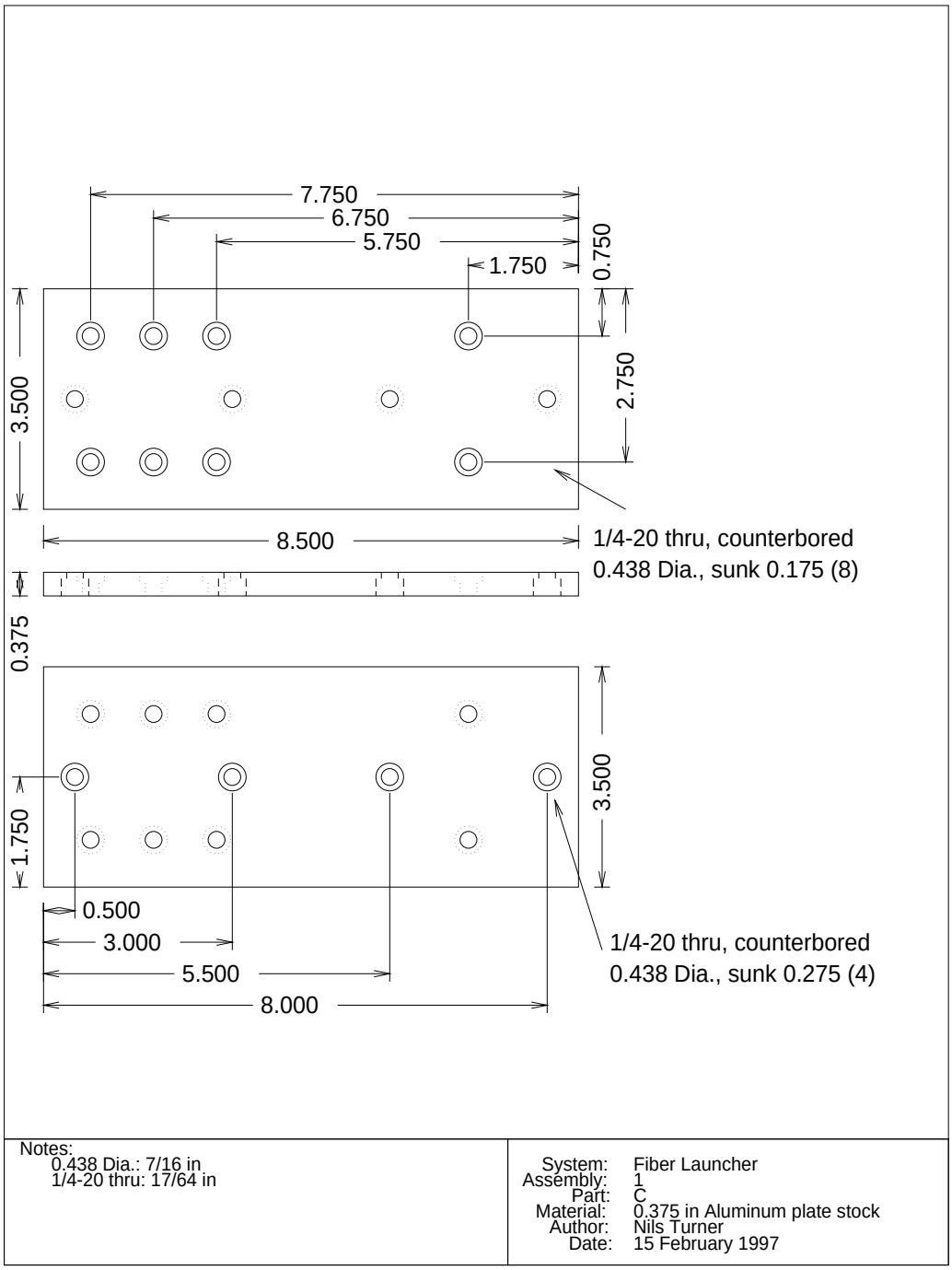

Figure C.3: *Fiber Launcher, Part 1C.* This part is the top plate of the I-beam referred to in Section 5.3.1.

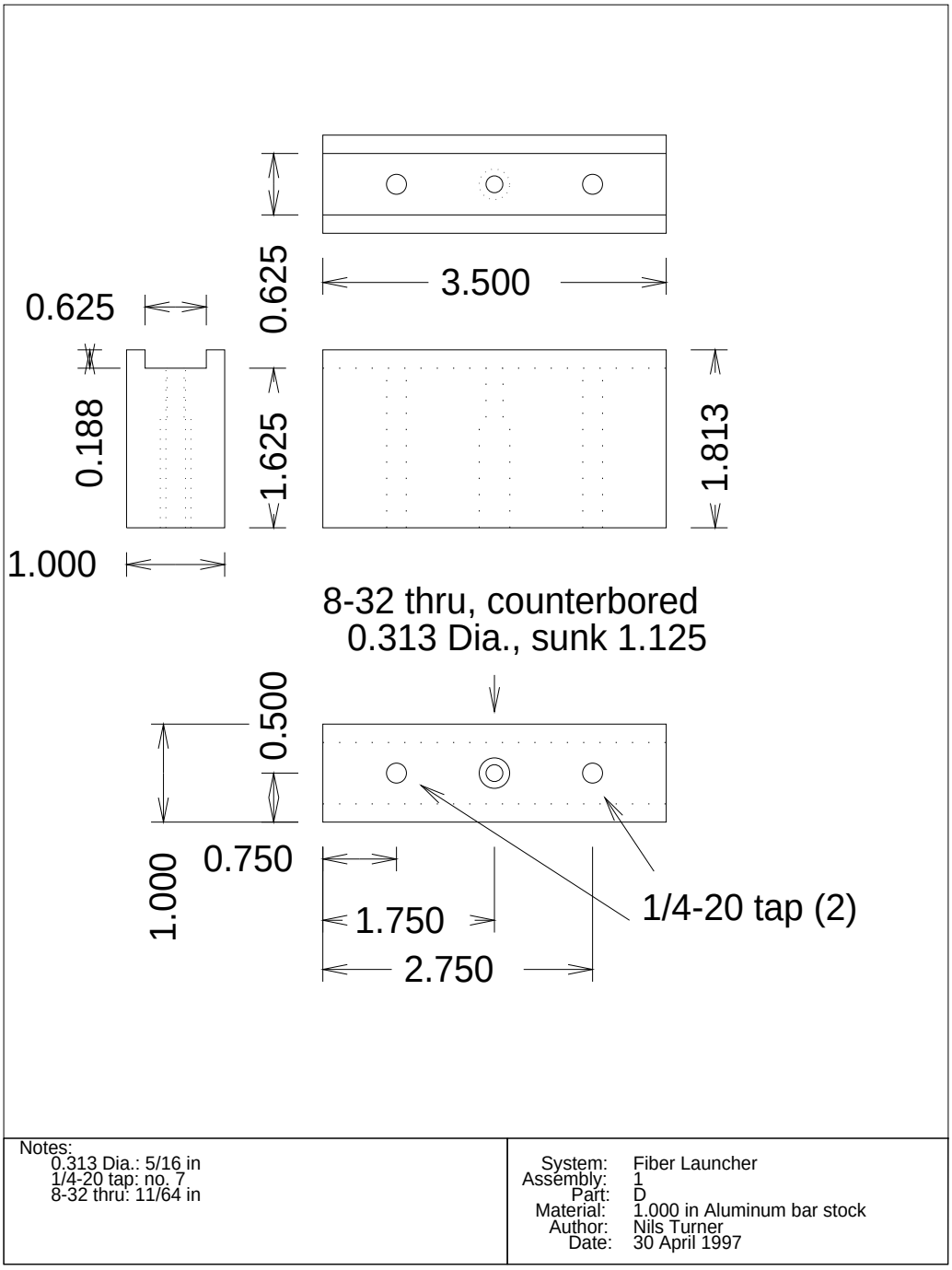

Figure C.4: *Fiber Launcher, Part 1D.* This part supports the motorized X-Y fiber optic strand positioner.

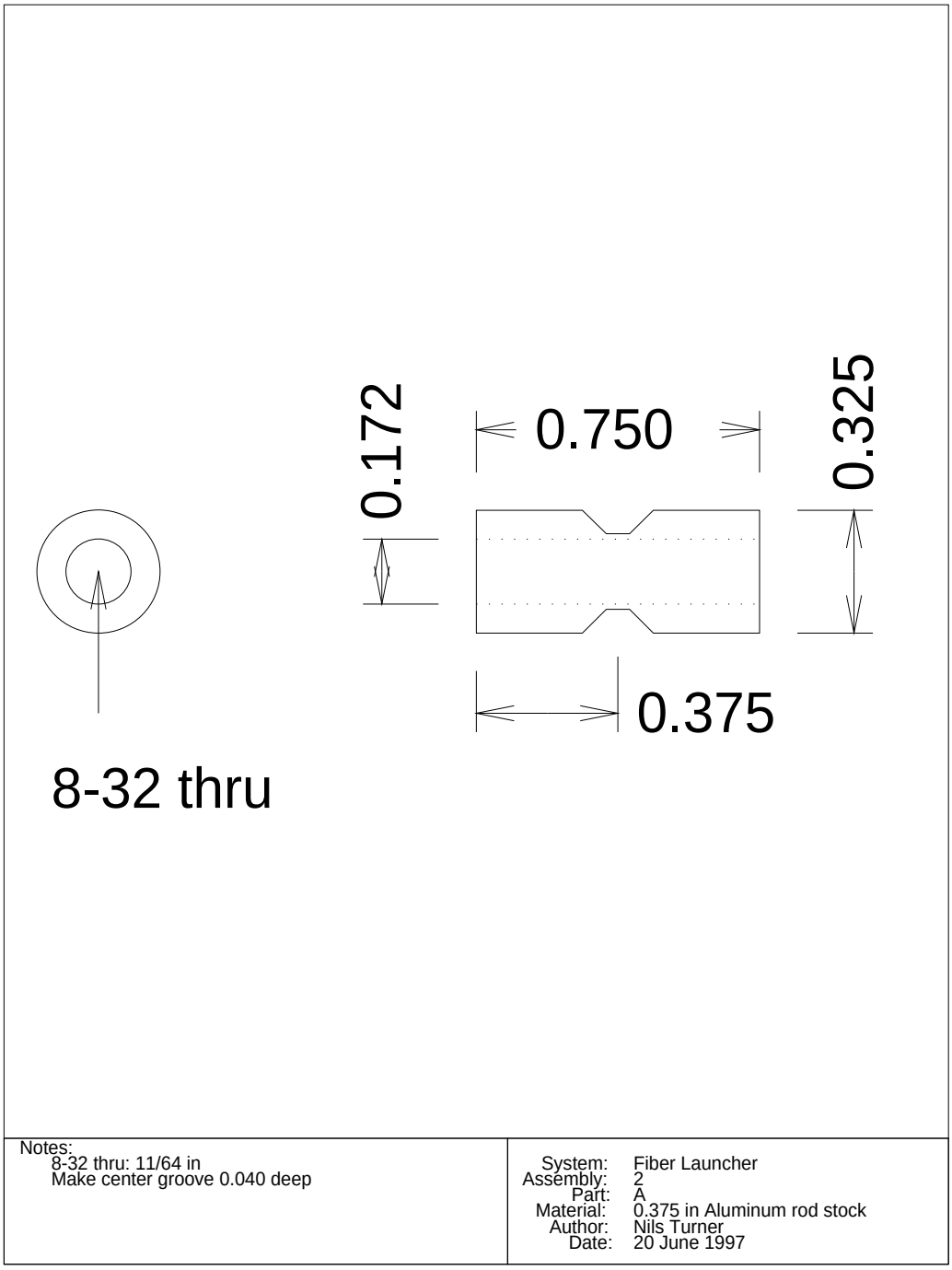

Figure C.5: *Fiber Launcher, Part 2A*. This part is one of four support posts for the springs that keep the I-beam described in Section 5.3.1 against the micrometer.

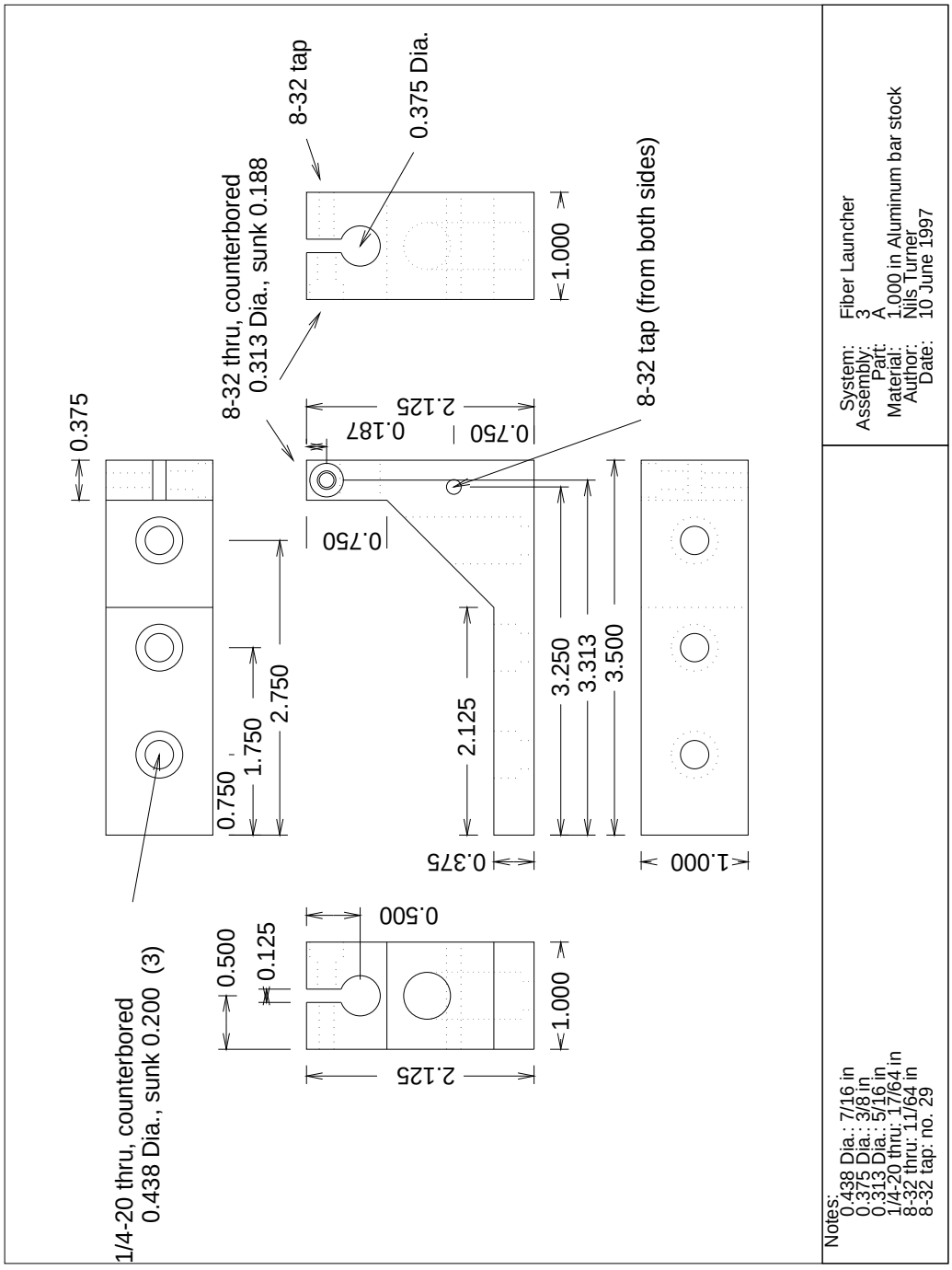

Figure C.6: *Fiber Launcher, Part 3A*. This part is the micrometer clamp.

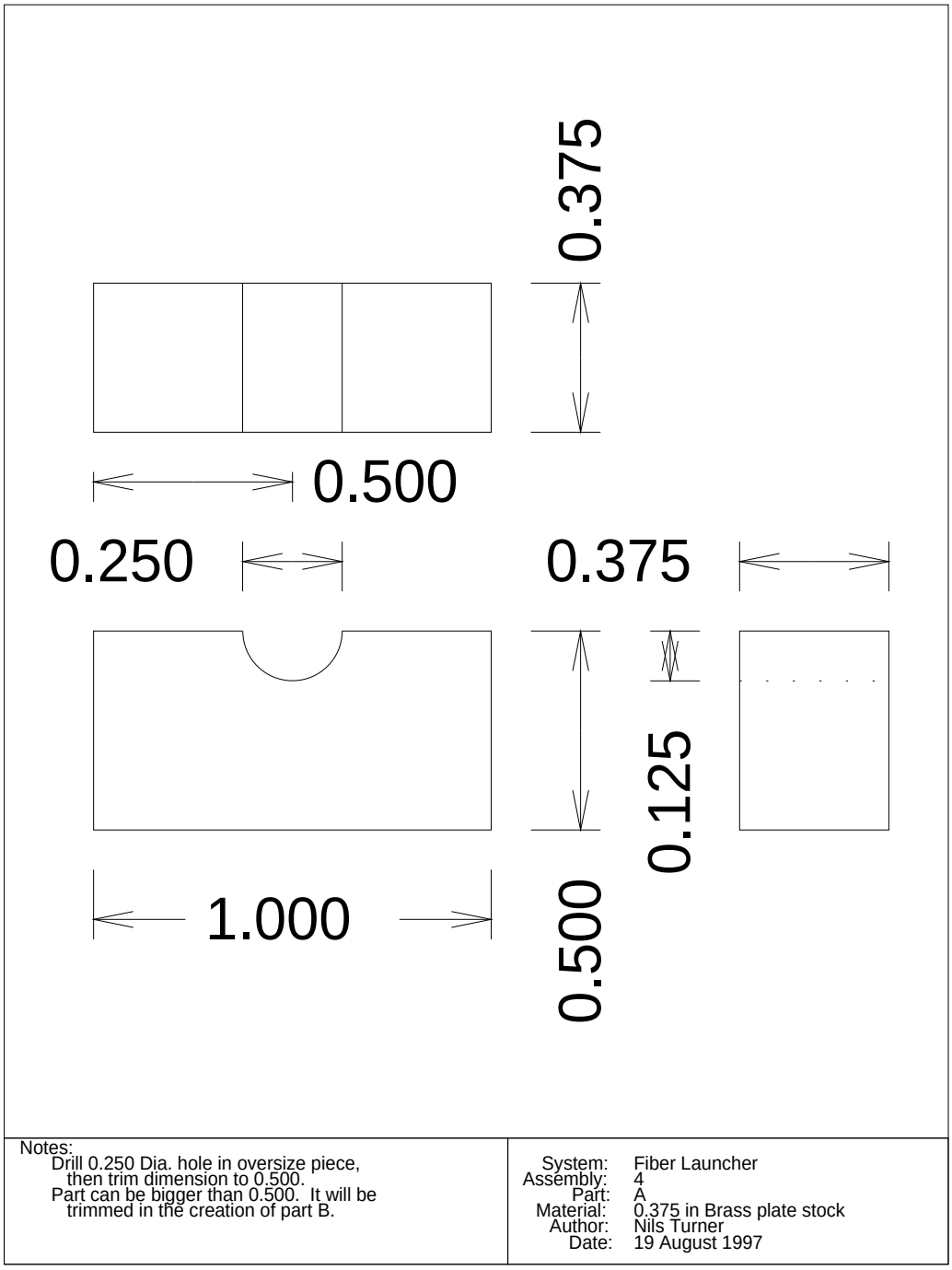

Figure C.7: *Fiber Launcher, Part 4A*. This part is a piece of the strand cable clamp. It gets brazed to *Part 4B*.

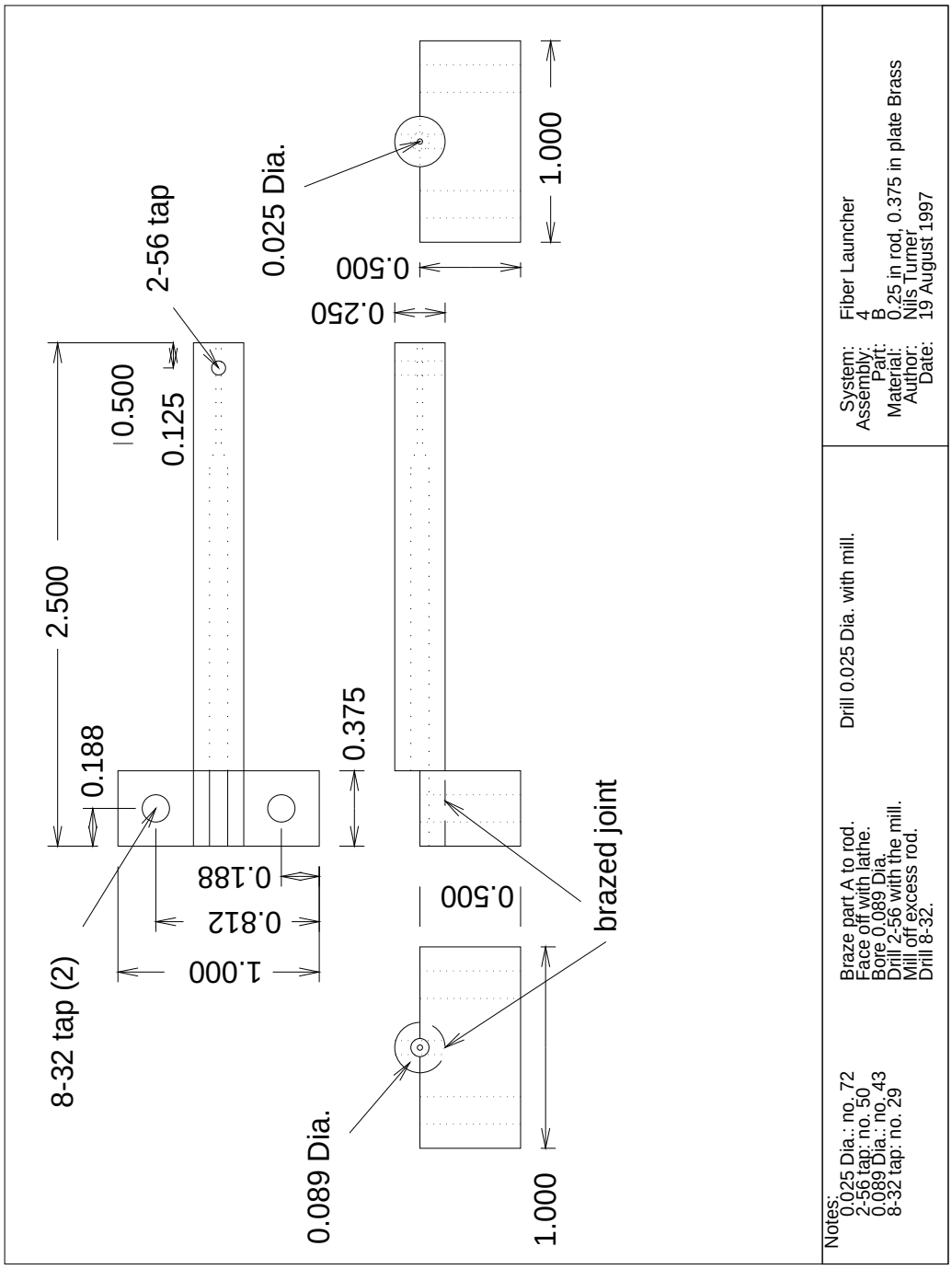

Figure C.8: *Fiber Launcher, Part 4B.* This part is a piece of the strand cable clamp. It gets brazed to *Part 4A*.

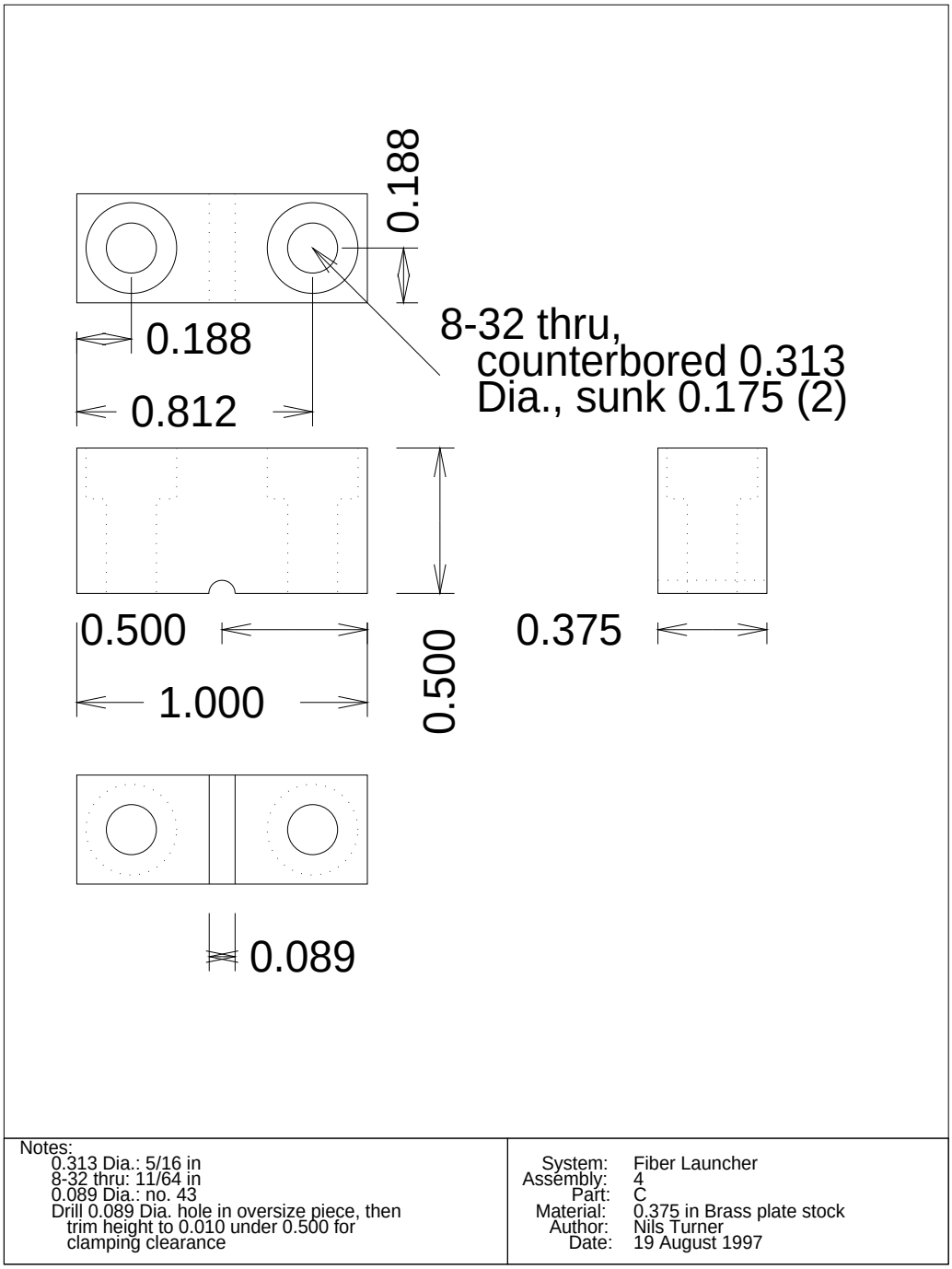

Figure C.9: *Fiber Launcher, Part 4C.* This part is a piece of the strand cable clamp.

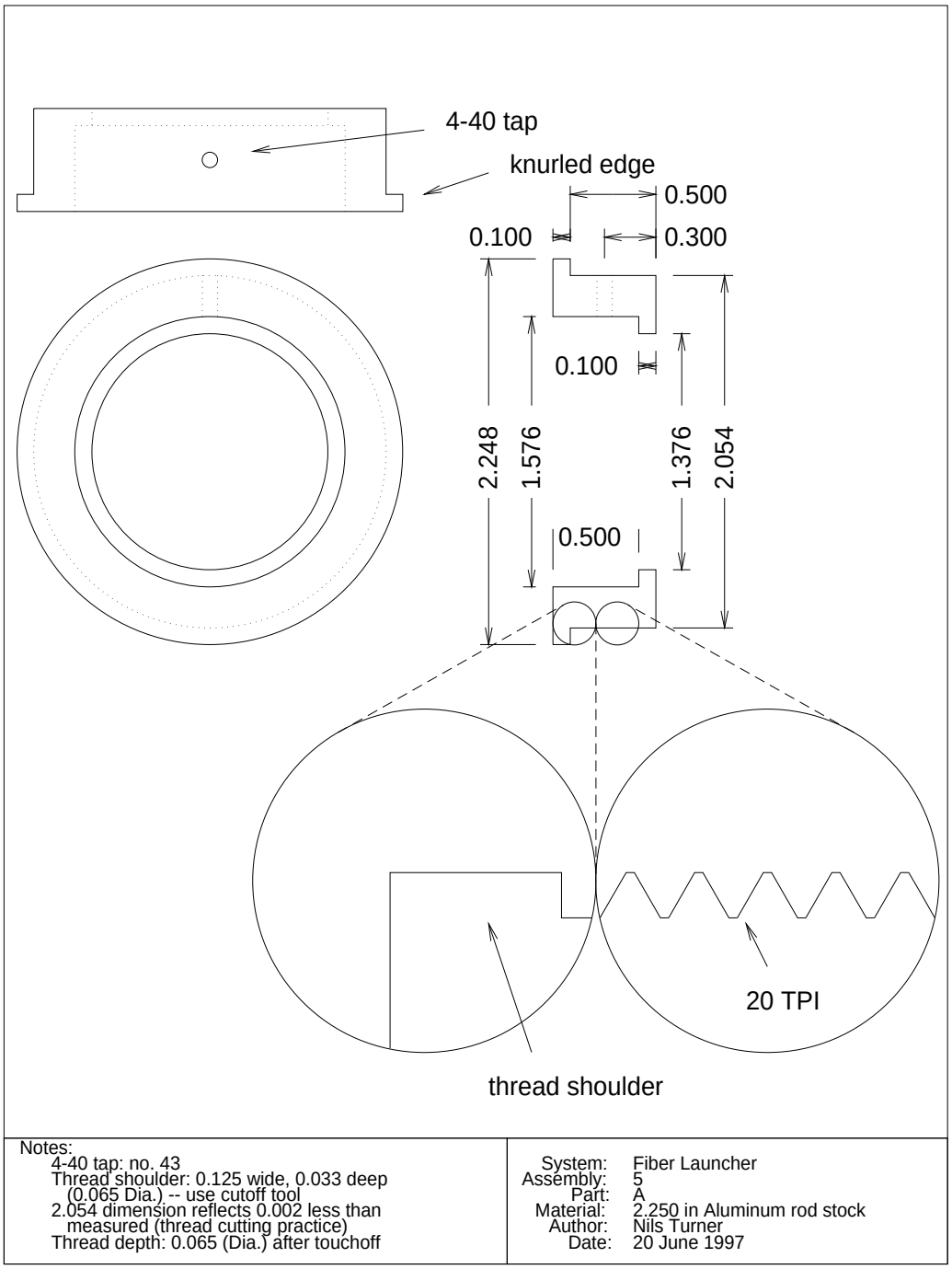

Figure C.10: *Fiber Launcher, Part 5A*. This part is a lens adapter ring. It allows 40 mm diameter lenses to be used in 2 inch lens mounts.

C.2 Fiber Collimator System

The Collimator system has three assemblies. Assembly 1 has six parts, Assembly 2 four parts, and Assembly 3 one part. Three copies of each of the Assembly 1 and Assembly 2 parts were built. Only one copy of the Assembly 3 part was built. These are listed in the following pages and complete this section.

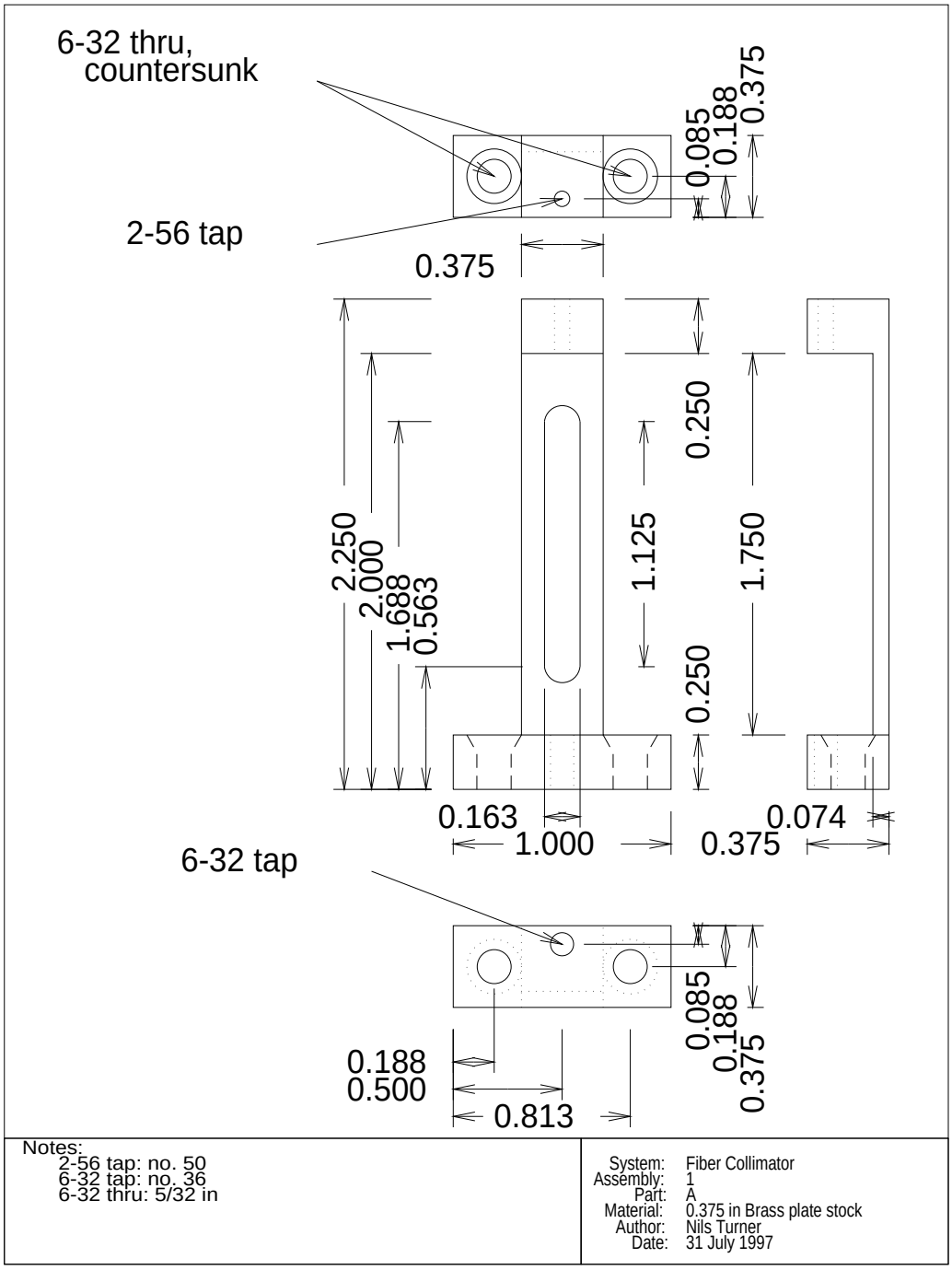

Figure C.11: *Fiber Collimator, Part 1A*. This part is a piece of the collimation lens X-Y-Z translation stage.

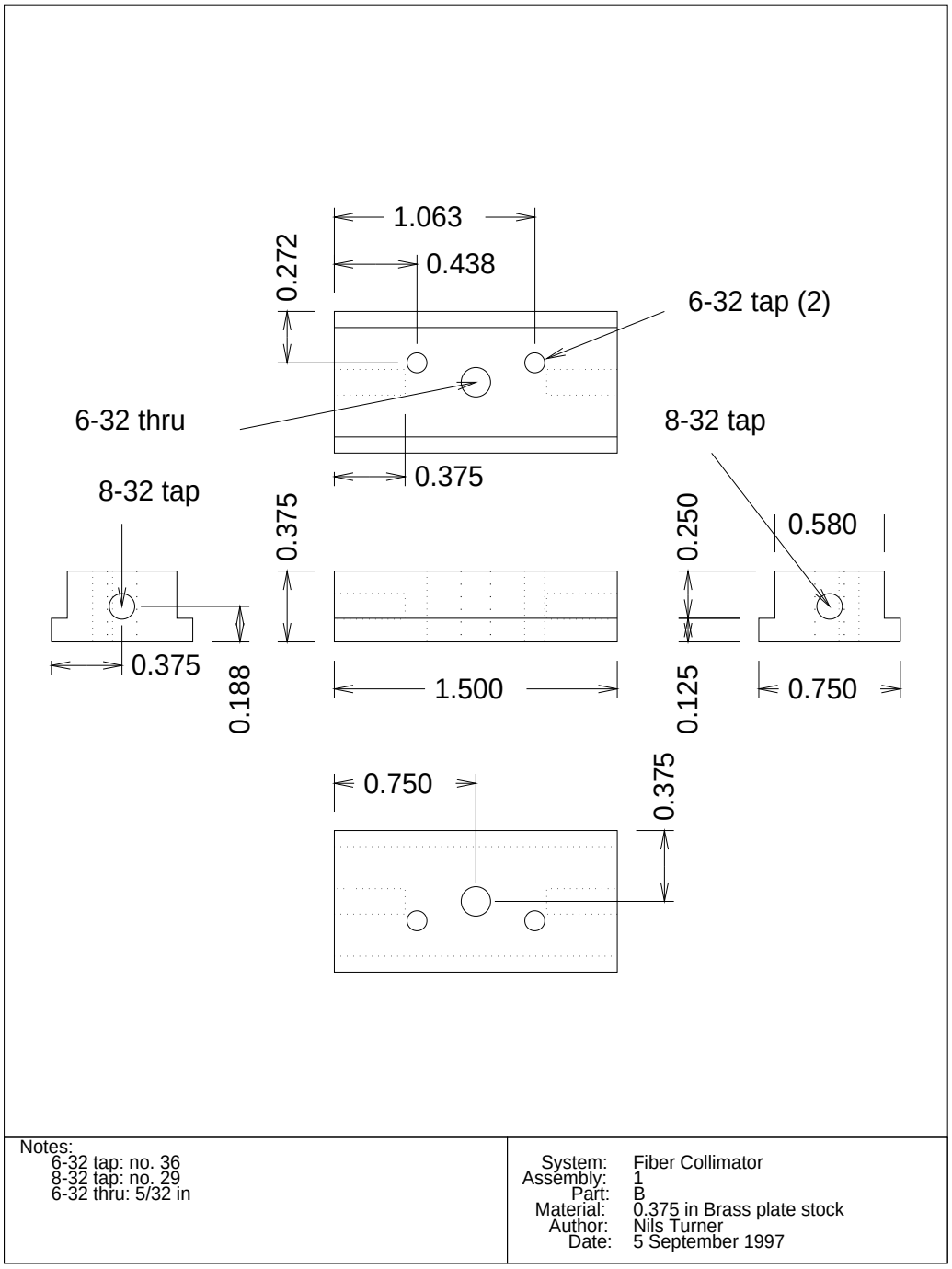

Figure C.12: *Fiber Collimator, Part 1B.* This part is a piece of the collimation lens X-Y-Z translation stage.

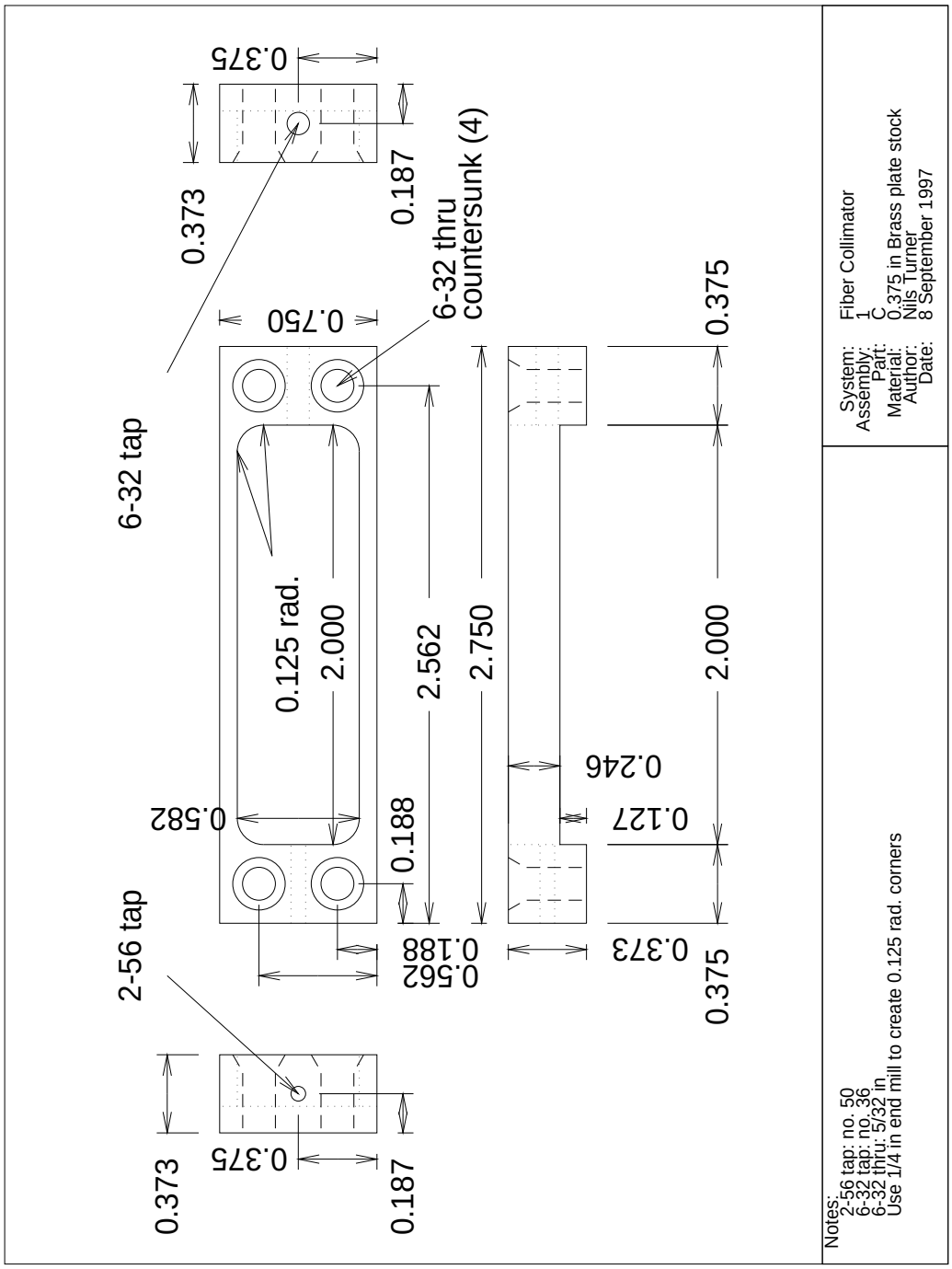

Figure C.13: *Fiber Collimator, Part 1C.* This part is a piece of the collimation lens X-Y-Z translation stage.

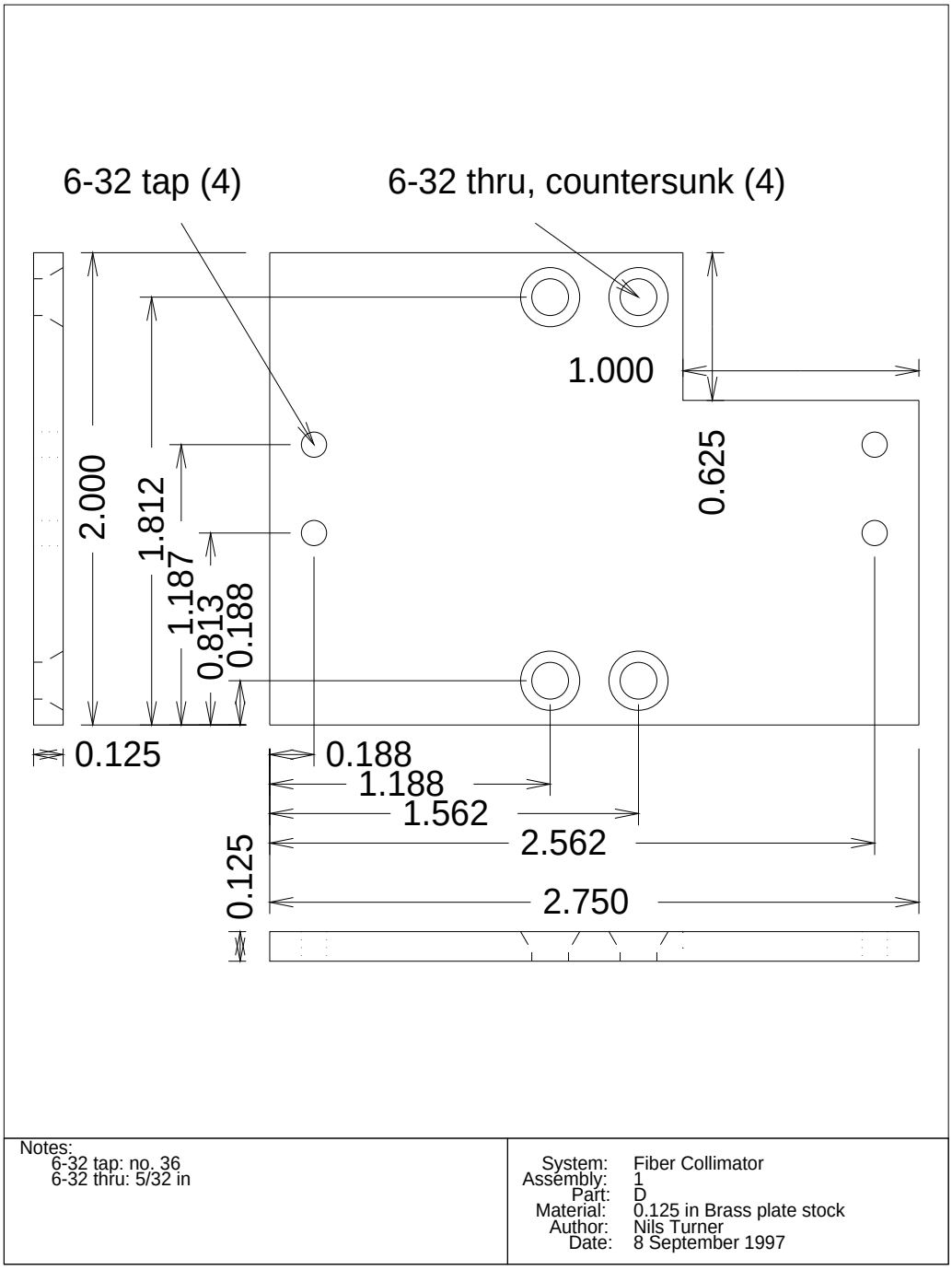

Figure C.14: *Fiber Collimator, Part 1D.* This part is a piece of the collimation lens X-Y-Z translation stage.

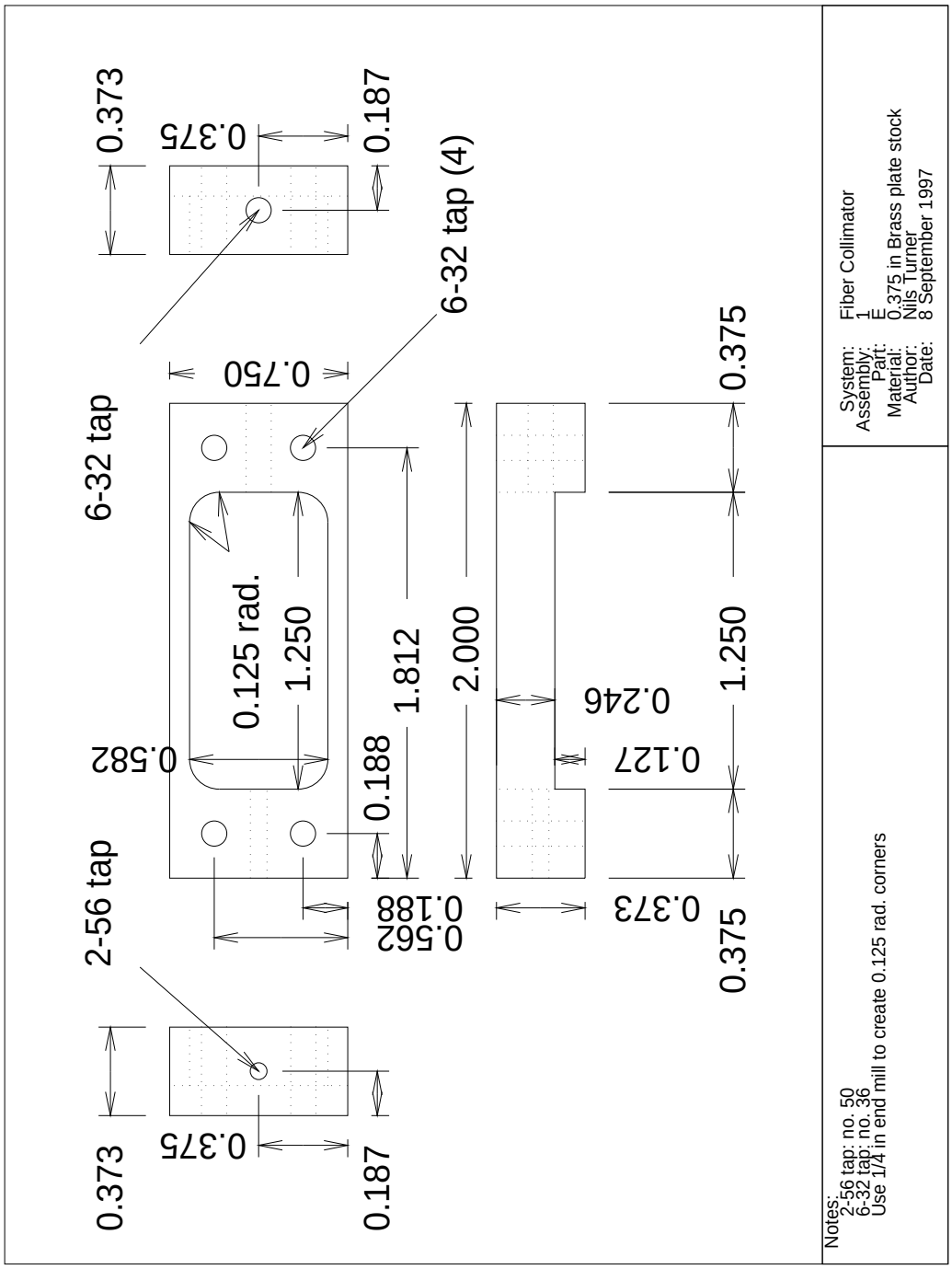

Figure C.15: *Fiber Collimator, Part 1E.* This part is a piece of the collimation lens X-Y-Z translation stage.

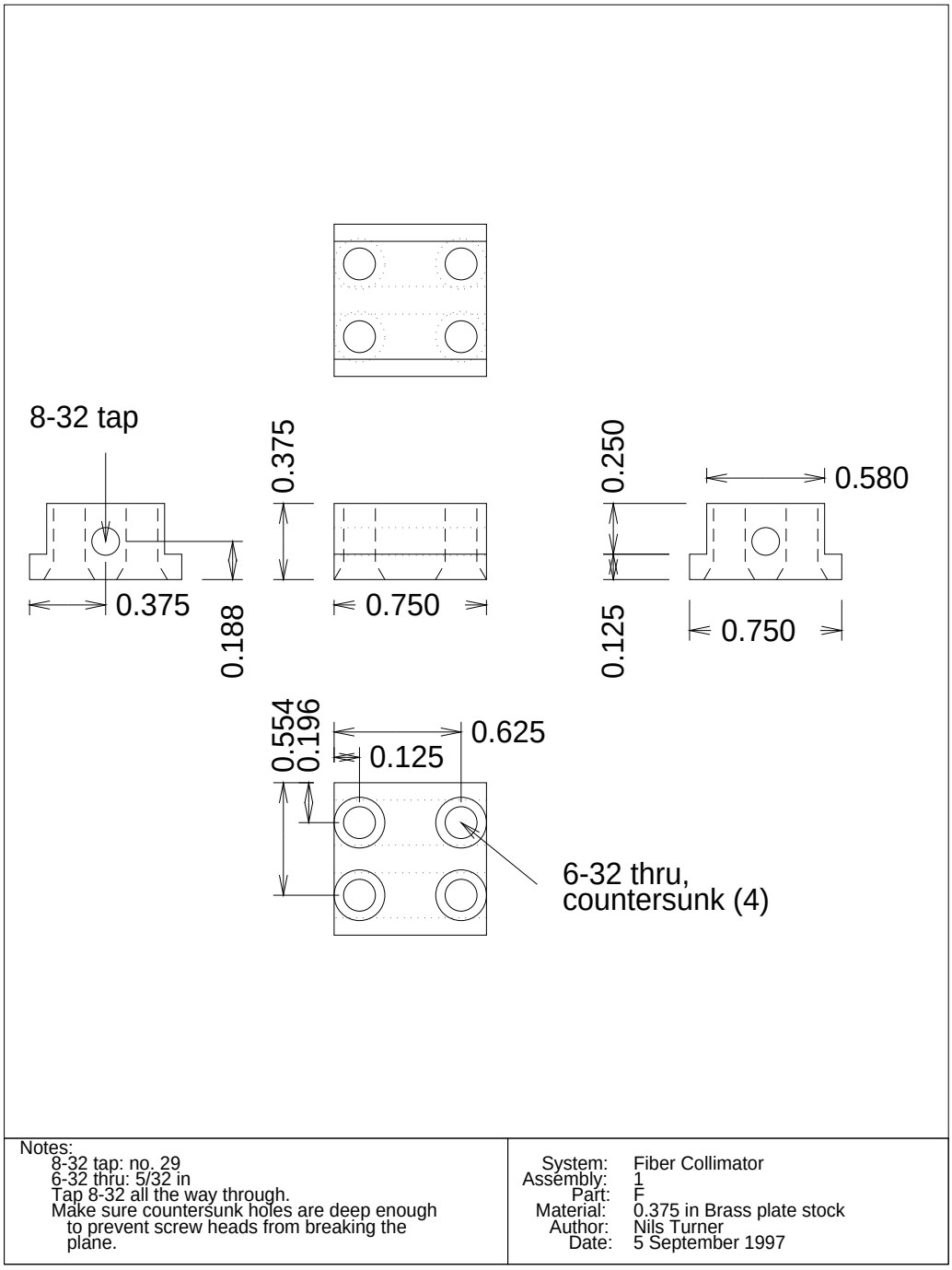

Figure C.16: *Fiber Collimator, Part 1F.* This part is a piece of the collimation lens X-Y-Z translation stage.

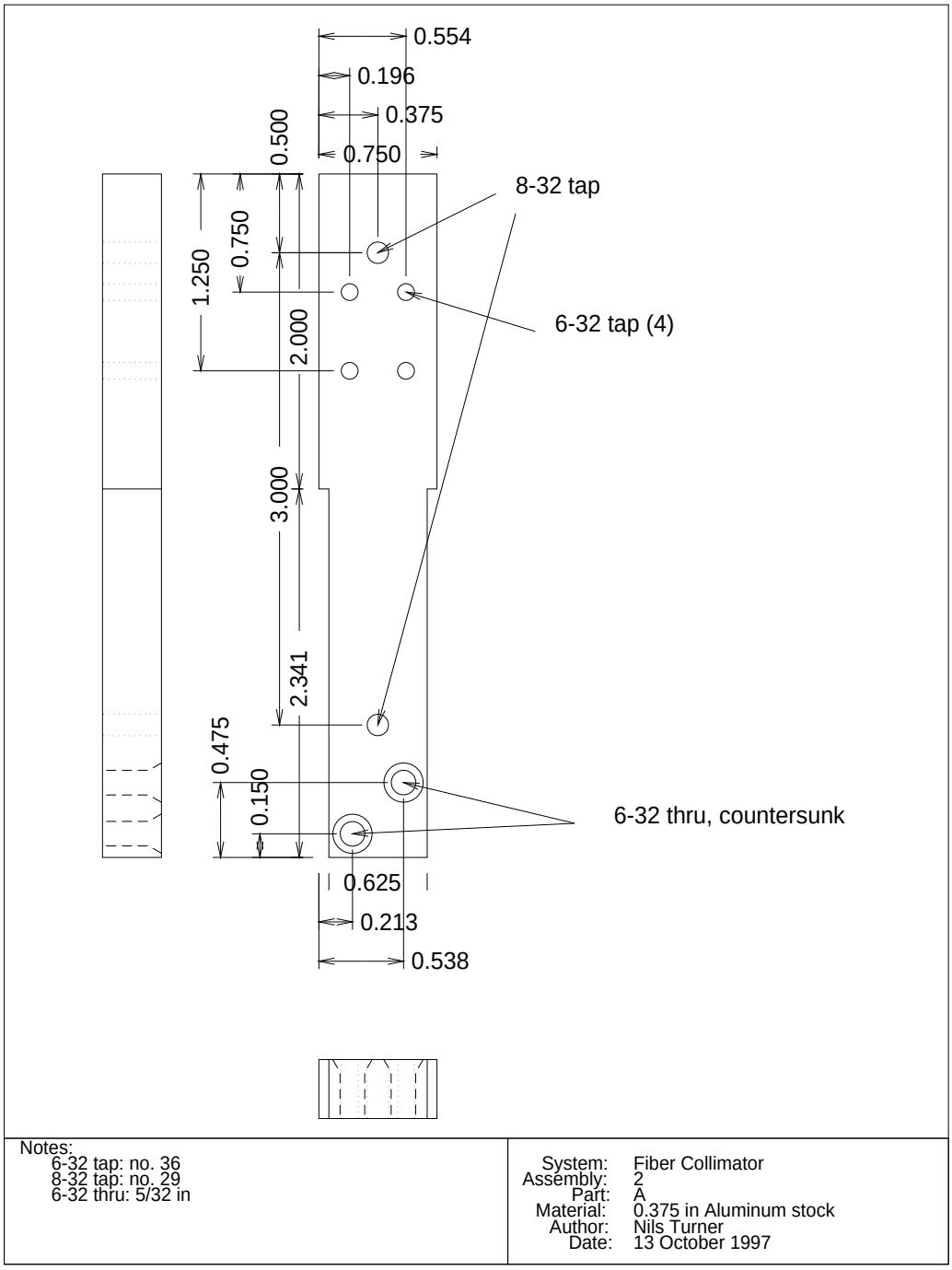

Figure C.17: *Fiber Collimator, Part 2A*. This part is a piece of the fiber optic strand tip clamp and positioner.

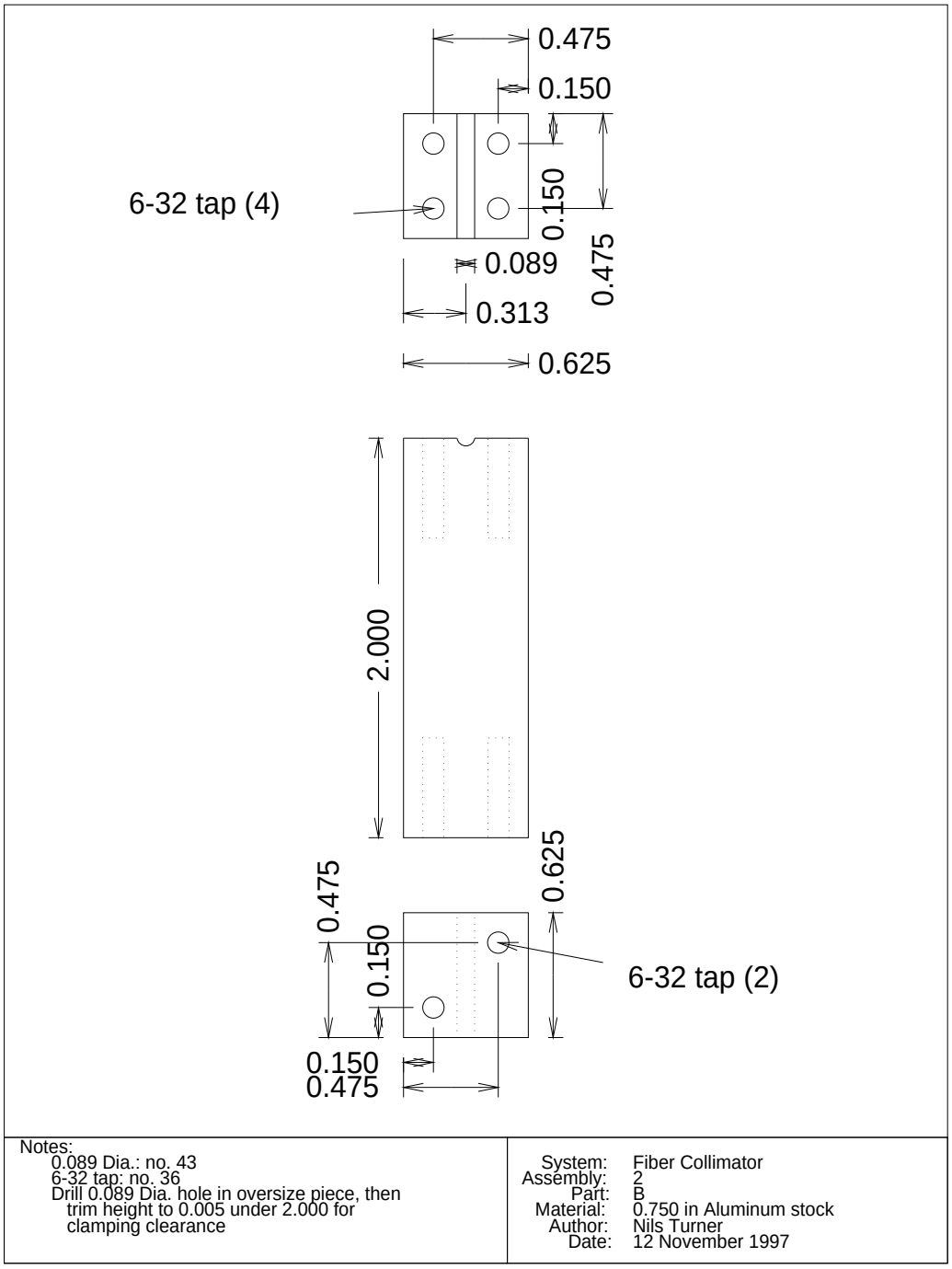

Figure C.18: *Fiber Collimator, Part 2B.* This part is a piece of the fiber optic strand tip clamp and positioner.

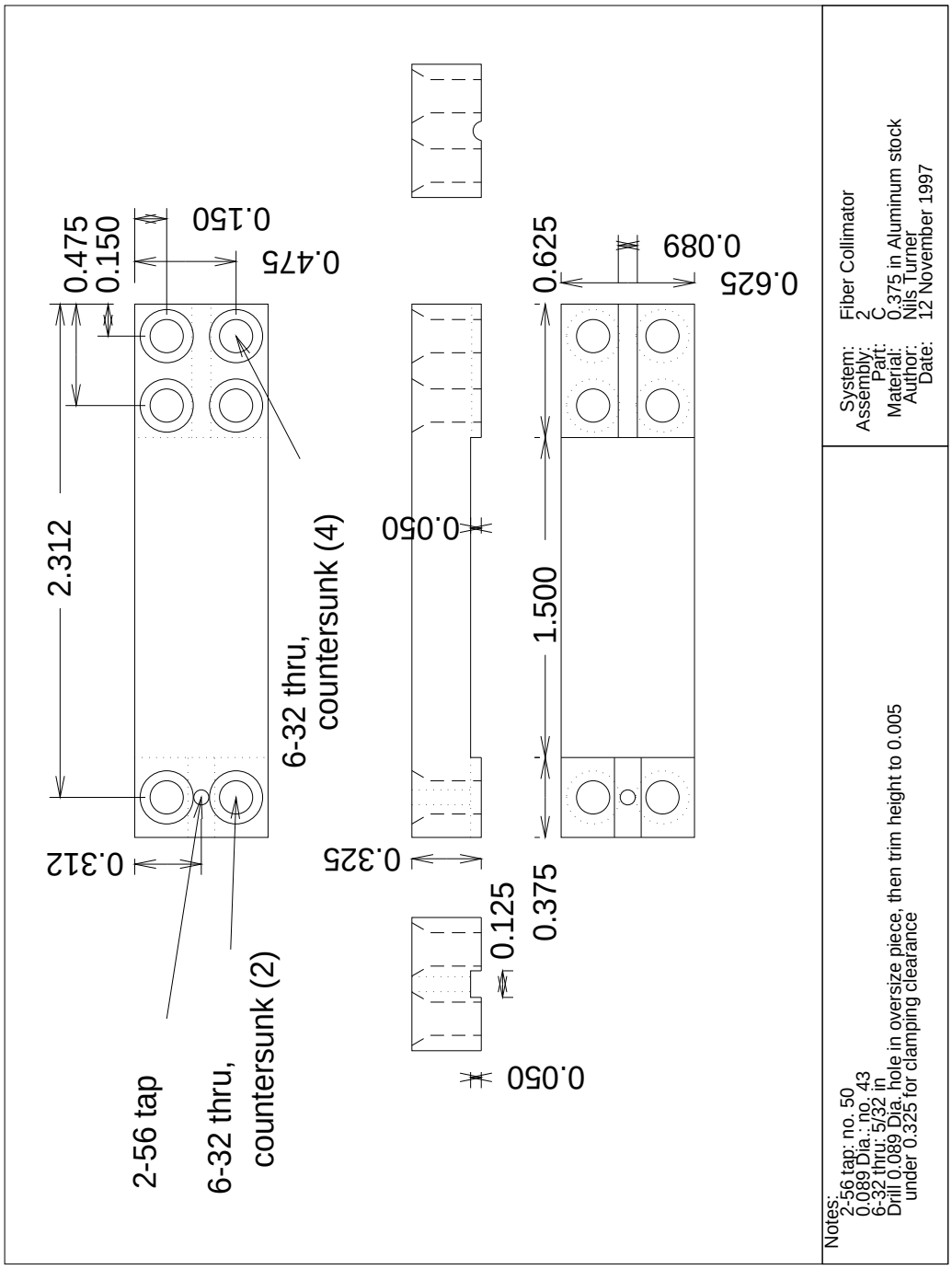

Figure C.19: *Fiber Collimator, Part 2C.* This part is a piece of the fiber optic strand tip clamp and positioner.

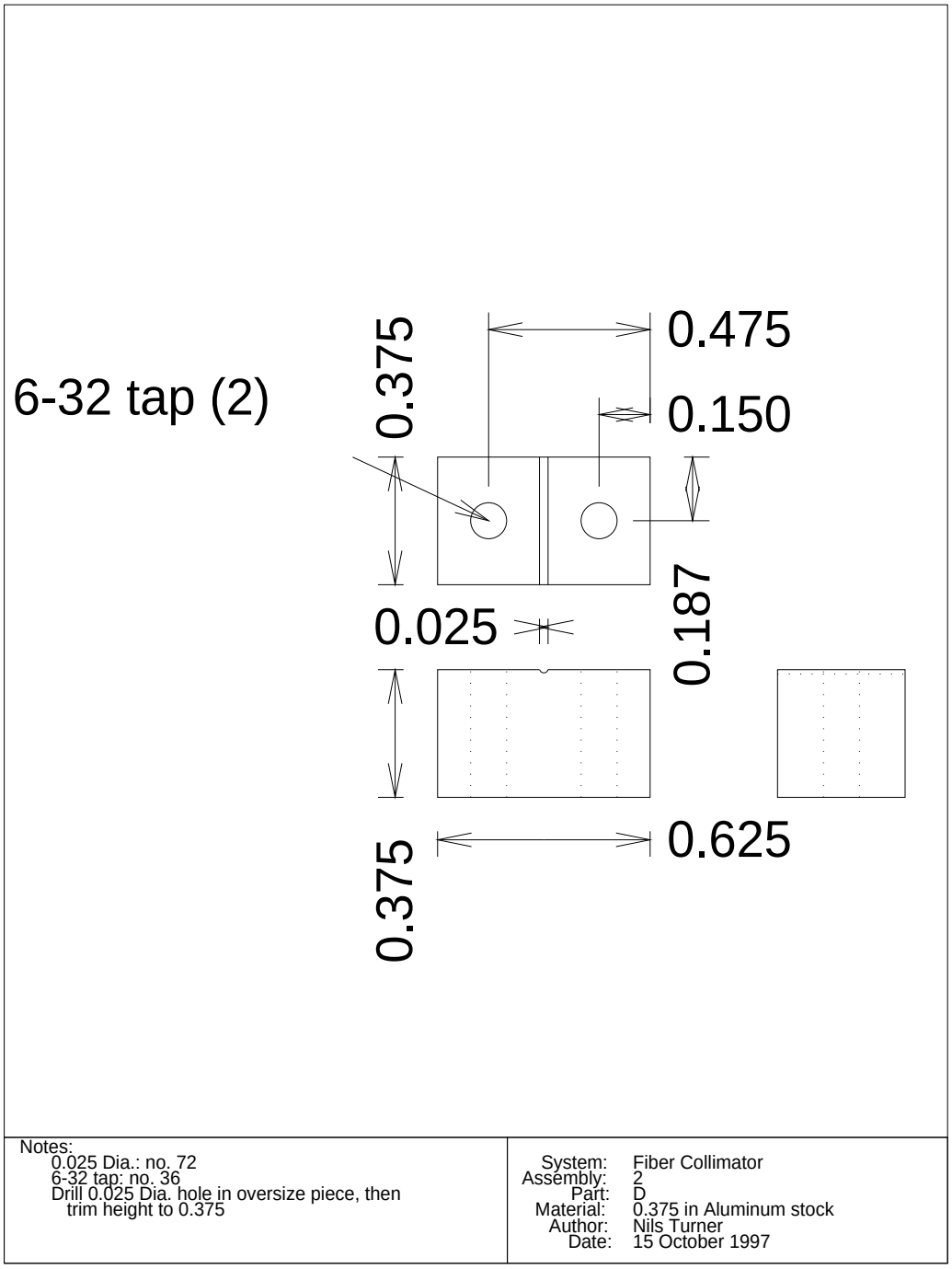

Figure C.20: *Fiber Collimator, Part 2D.* This part is a piece of the fiber optic strand tip clamp and positioner.

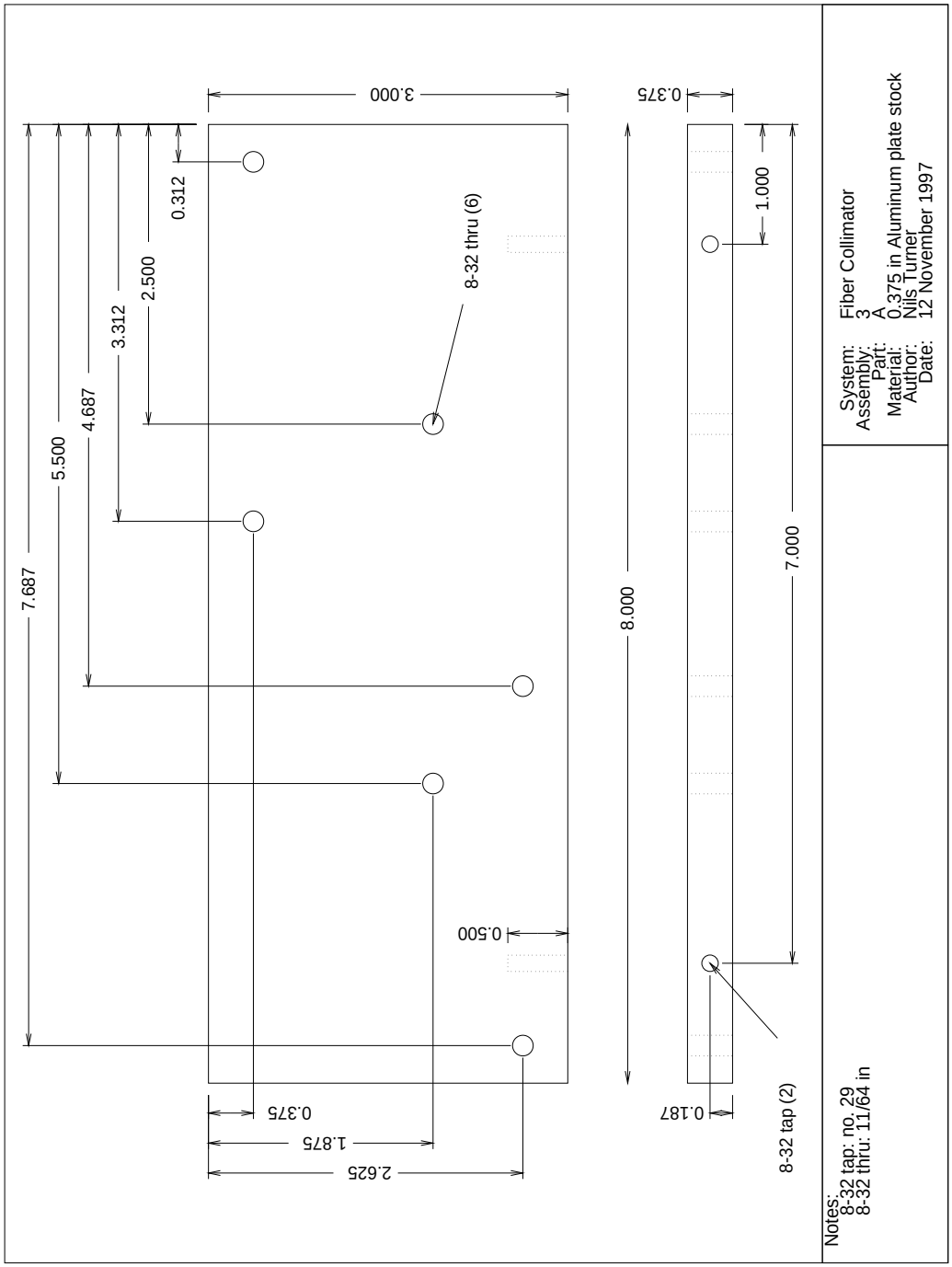

Figure C.21: *Fiber Collimator, Part 3A*. This part provides a base for the assembled parts in Assembly 1 and Assembly 2, staggering the X-Y-Z translation stages for a close packing.

C.3 Spectrograph System

The Spectrograph system has one assembly. Assembly 2 has two parts. Two copies of each of the Assembly 2 parts were built. Assembly 1 has been removed from the listing. It was a mount for a fast, f-1.6, achromat which proved unsuitable for use in the Spectrograph system. Assembly 2 parts are listed in the following pages and complete this section.

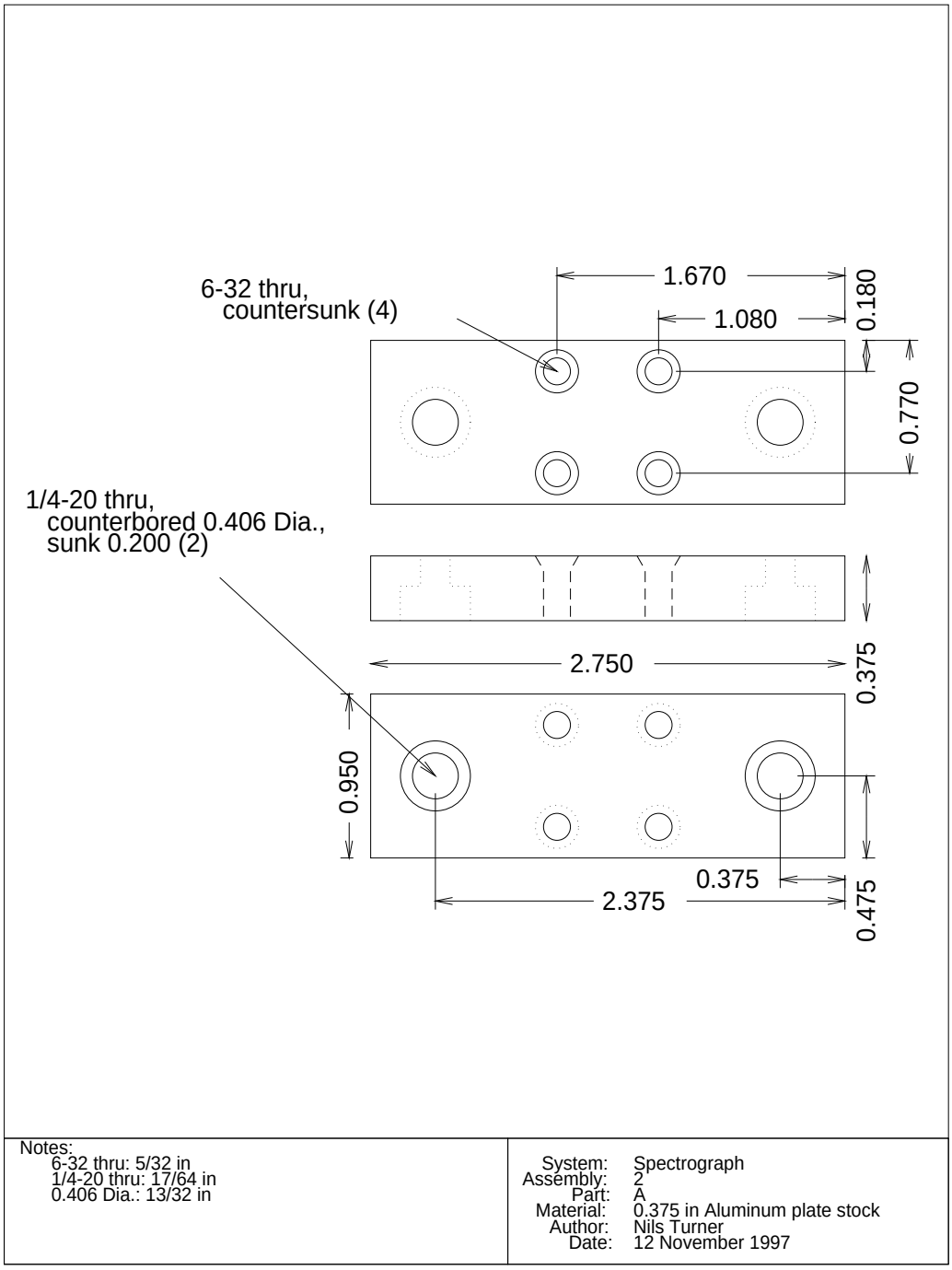

Figure C.22: *Spectrograph, Part 2A*. This part is a piece of the cylindrical element mount rotation adapter.

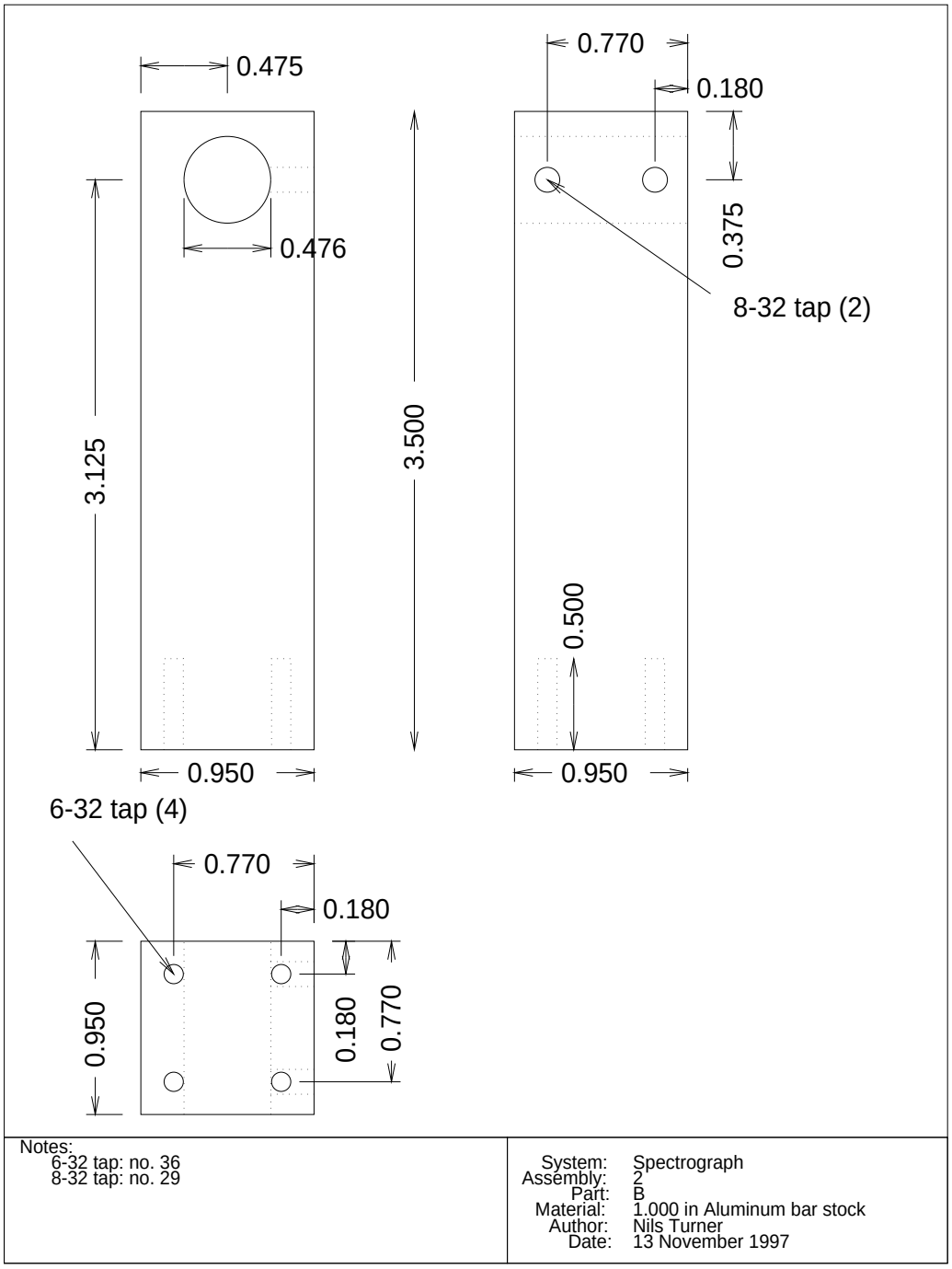

Figure C.23: *Spectrograph, Part 2B.* This part is a piece of the cylindrical element mount rotation adapter.

C.4 Jigs

There are two jigs that were created to aid in assembly of the prototype imager. They were both used in fiber optic strand creation. Jig 1 has two parts and Jig 2 has one part. Only one of each part was built. The parts are listed on the following pages and complete this section.

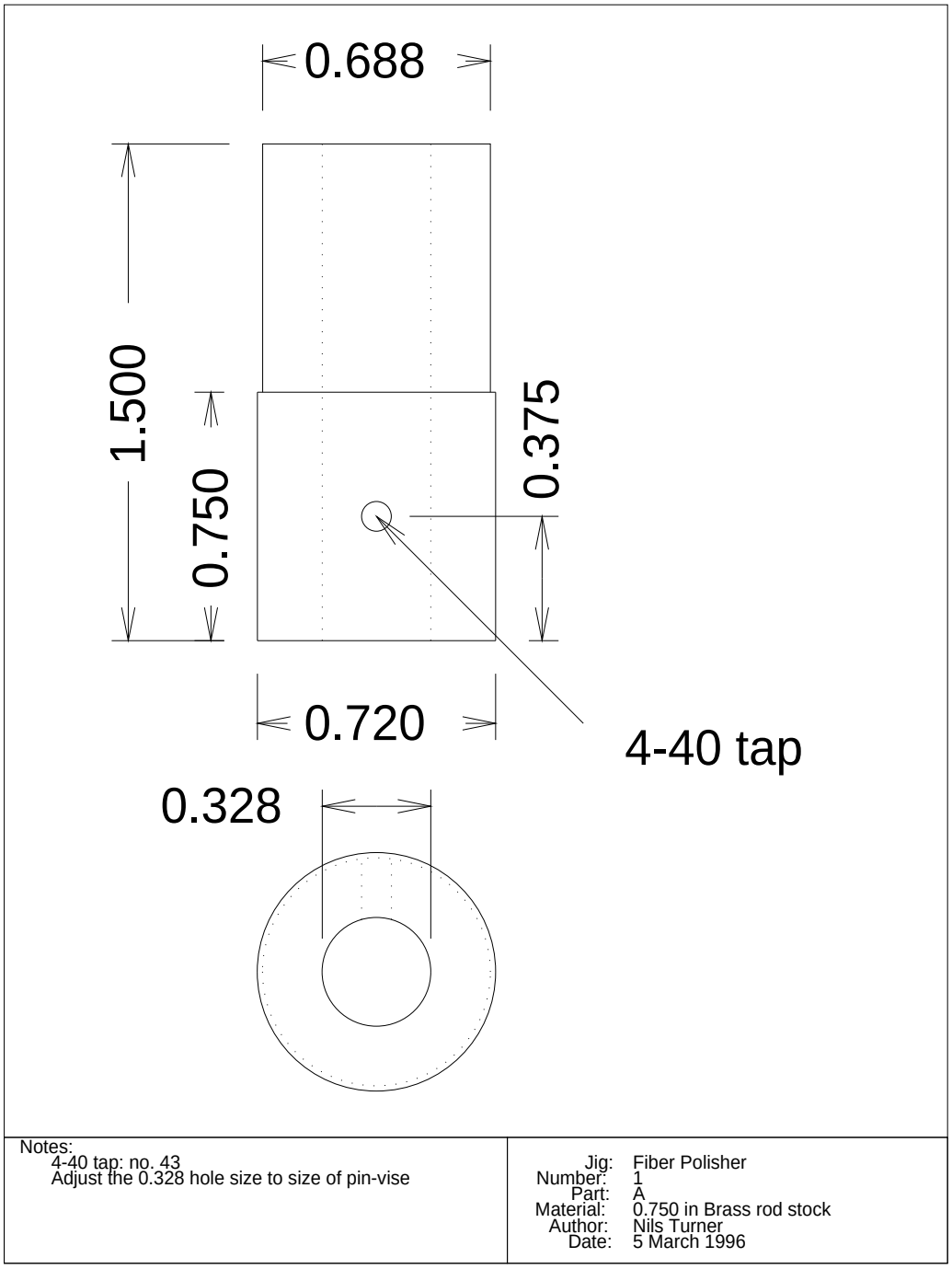

Figure C.24: *Fiber Vise, Part A.* This part mounts a pin-vise for holding the strand tip during polishing.

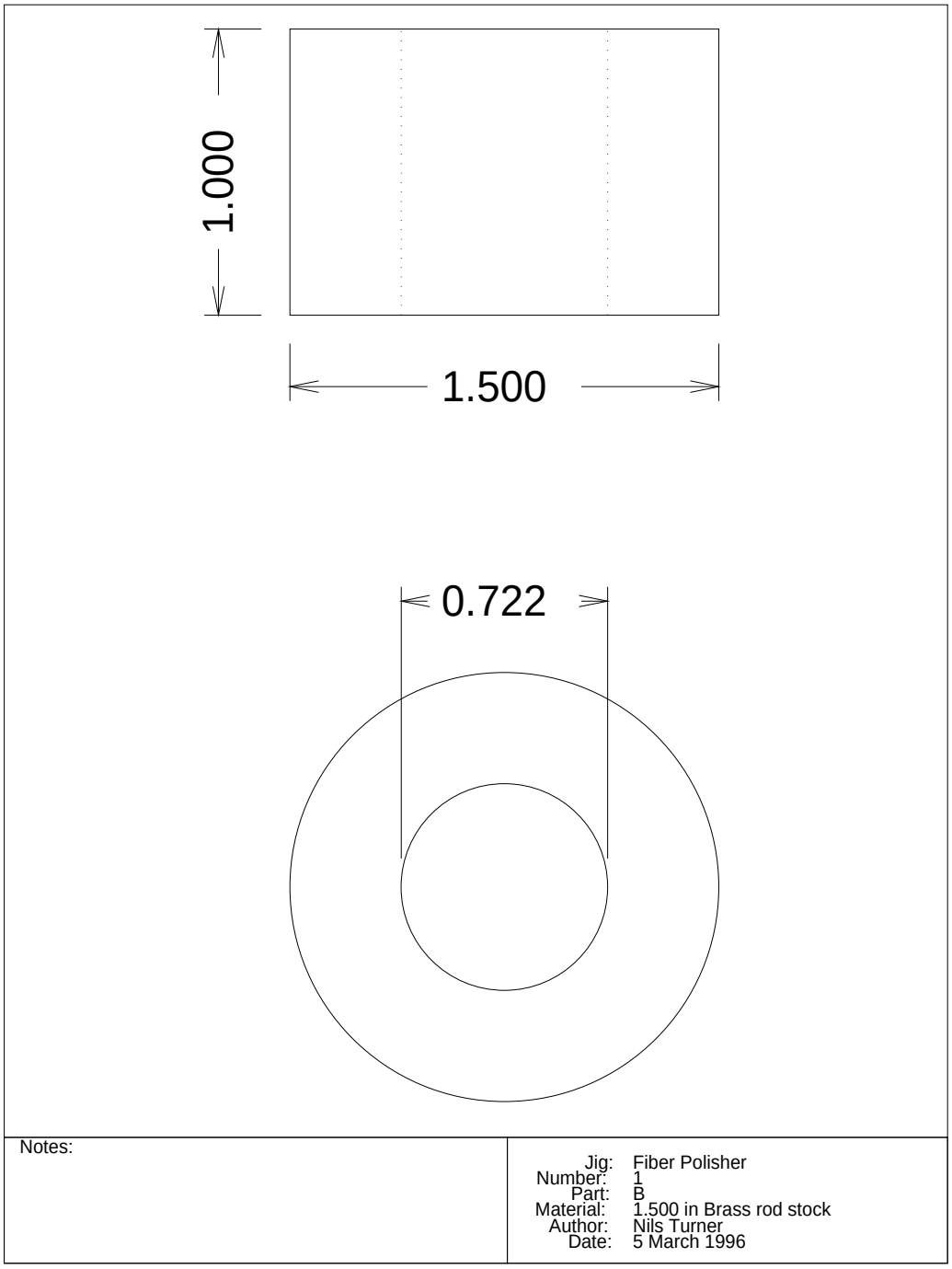

Figure C.25: *Fiber Vise, Part B.* This part keeps *Part A* square to the abrasive surface during polishing.

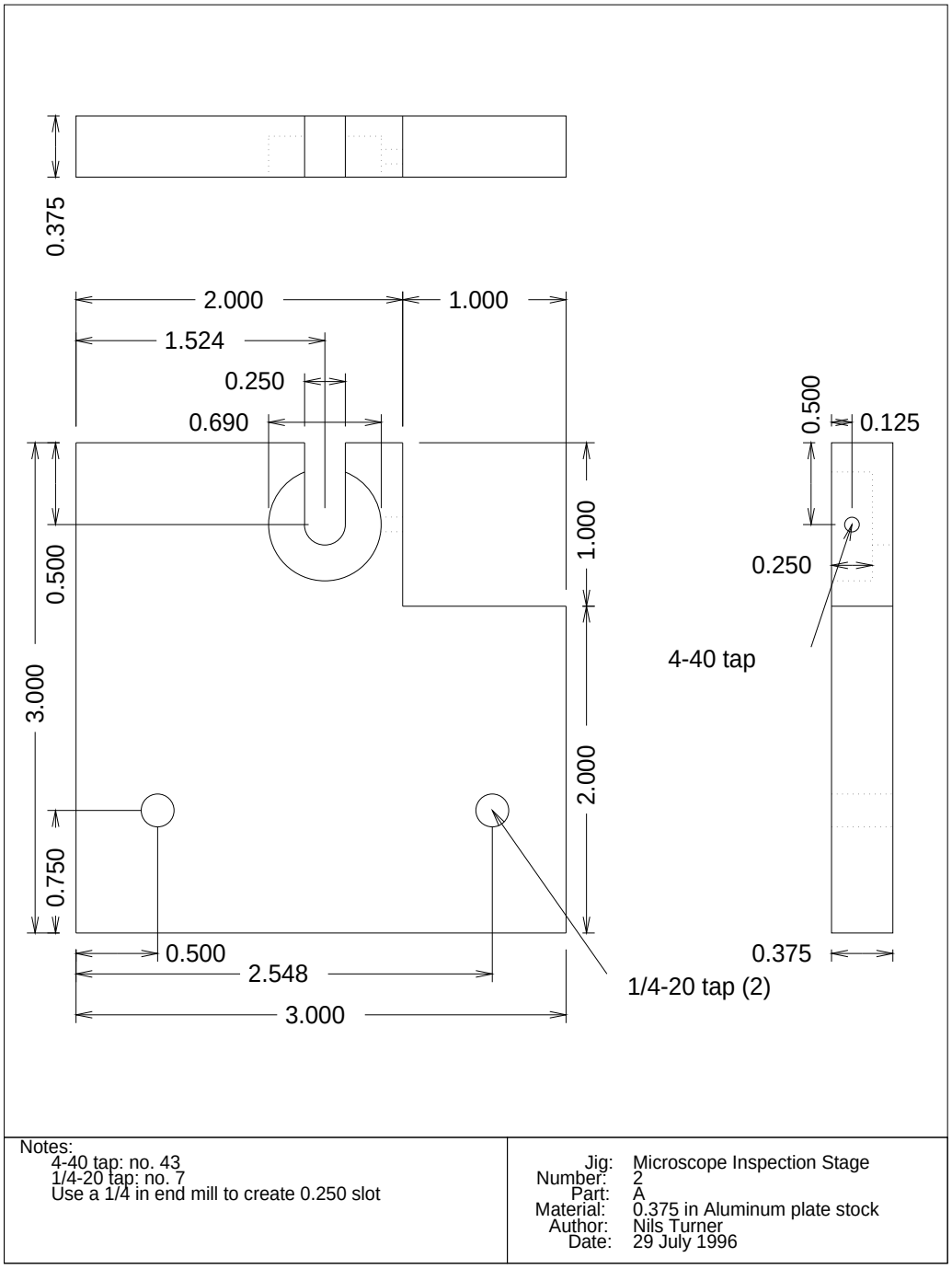

Figure C.26: *Microscope Stage, Part A.* This part replaces the standard microscope slide platform on a 1960s era AO Spencer biological microscope.

Appendix D

Cylinder Functions

Jahnke et al. (1960) refer to the solutions of *Bessel's equation*,

$$x^2 f''(x) + x f'(x) + (x^2 - \nu^2) f(x) = 0, \tag{D.1}$$

as cylinder functions. The equation is well known and is frequently used to teach one the power series method of solving differential equations. As a result, most any textbook for a course on differential equations will present a discussion. An excellent discussion can be found in Boyce and DiPrima (1986).

D.1 Notation

Notation for the various components of the solution of equation D.1 varies between authors. Since equation D.1 is a second order equation, two linearly independent solutions must be found to completely characterize the solution. These two solutions take different forms depending on whether ν is an integer or not. If ν is *not* an integer, the solution is simply

$$f(x) = A J_\nu(x) + B J_{-\nu}(x), \tag{D.2}$$

where $J_\nu(x)$ is commonly known as the *Bessel function of order* ν. It is also known as the *Bessel function of the first kind, of order* ν.

If ν is an integer, $J_\nu(x)$ and $J_{-\nu}(x)$ are no longer linearly independent. A second

solution can be generated through a technique known as *reduction of order* (Boyce and DiPrima 1986). This second solution is named the *Neumann function of order* ν or the *Bessel function of the second kind, of order* ν, represented as $Y_\nu(x)$. It is usually the practice to change ν to n in the integer case. The solution then becomes

$$f(x) = AJ_n(x) + BY_n(x). \tag{D.3}$$

Two other functions can be generated from $J_\nu(x)$ and $Y_\nu(x)$,

$$\begin{aligned} H_\nu^{(1)}(x) &= J_\nu(x) + iY_\nu(x) \\ H_\nu^{(2)}(x) &= J_\nu(x) - iY_\nu(x). \end{aligned} \tag{D.4}$$

These functions are known as *Hankel functions of order* ν or *Bessel functions of the third kind, of order* ν. Together, they make up a complete set of solutions to Bessel's equation. The Hankel functions are useful for imaginary values of the argument, x.

D.2 Series Representations

The most straight-forward way of representing the Bessel function analytically is to resort to series notation,

$$J_\nu(x) = \sum_{k=0}^{\infty} \frac{(-1)^k}{k!\,\Gamma(\nu + k + 1)} \left(\frac{x}{2}\right)^{\nu+2k}, \tag{D.5}$$

where $\Gamma(\nu + k + 1)$ is the generalized factorial function,

$$\Gamma(\nu + k + 1) = \int_0^\infty e^{-t} t^{\nu+k} dt. \tag{D.6}$$

In the case that $\nu + k$ is an integer greater than or equal to -1,

$$\begin{aligned} \Gamma(\nu + k + 1) &= \Gamma(n + 1) \\ &= n! \end{aligned} \tag{D.7}$$

Representing the Bessel function of the second kind is notationally more complex.

Courant and Hilbert (1989) express the relationship between $J_\nu(x)$ and $Y_\nu(x)$ as

$$\pi Y_\nu(x) = \frac{\partial J_\nu(x)}{\partial \nu} - (-1)^\nu \frac{\partial J_{-\nu}(x)}{\partial \nu} \tag{D.8}$$

When the order is *not* an integer, the relationship between $J_\nu(x)$ and $Y_\nu(x)$ is given as

$$Y_\nu(x) = \frac{1}{\sin \nu\pi}\Big(J_\nu(x)\cos \nu\pi - J_{-\nu}(x)\Big). \tag{D.9}$$

As can be easily seen in equation D.9, when ν approaches an integer, the sine function approaches 0. To overcome this problem, one must resort to the series representation of $J_n(x)$ (equation D.5) and equation D.8. The result comes out to be

$$\pi Y_n(x) = 2J_n(x)\ln\frac{e^\gamma x}{2} - \Big(\frac{x}{2}\Big)^n \sum_{k=0}^{\infty} \frac{(-1)^k(\varphi(k)+\varphi(k+n))}{k!\,(k+n)!}\Big(\frac{x}{2}\Big)^{2k} - \Big(\frac{x}{2}\Big)^{-n}\sum_{k=0}^{n-1}\frac{(n-k-1)!}{k!}\Big(\frac{x}{2}\Big)^{2k}, \tag{D.10}$$

where

$$\varphi(k) = \sum_{m=1}^{k}\frac{1}{m} \tag{D.11}$$

and γ, known as the *Euler constant*, is given as

$$\gamma = \lim_{k\to\infty}(\varphi(k) - \ln k). \tag{D.12}$$

Numerically, $\gamma = 0.577215665\ldots$, and $e^\gamma = 1.781072418\ldots$.

D.3 Behavior Near Zero

The Bessel function is nicely behaved at 0 for all values of ν.

$$J_\nu(0) = \begin{cases} 1 & \nu = 0, \\ 0 & \nu \neq 0. \end{cases} \tag{D.13}$$

For $Y_\nu(0)$, due to the asymptotic nature near 0 of many of the orders, several cases must be considered. From equations D.9 and D.13, $Y_\nu(0) = 0$ for all non-integer values of ν. When ν is an integer, $Y_\nu(x)$ asymptotically approaches 0. For these cases, limits must be considered. When $\nu = 0$, equations D.10 and D.13 combine to give

$$\lim_{x\to 0} Y_0(x) = \frac{2}{\pi} \ln \frac{e^\gamma x}{2}. \tag{D.14}$$

In equation D.10, note that there are three terms on the right side of the equation. When ν (or n) is an integer greater than or equal to 1, the first term is always 0. Due to the values of x in the numerator, the second term is also 0 for the above specified values of ν (or n). In the third term, there is always a term when $k = 0$, and therefore a value proportional to $\frac{1}{x}$ survives, and must be kept for the assessment of the limit. Compiling these results, one gets

$$\lim_{x\to 0} Y_\nu(x) \begin{cases} 0 & \nu \text{ not an integer} \\ \frac{2}{\pi} \ln \frac{e^\gamma x}{2} & \nu = 0 \\ -\frac{(\nu-1)!}{\pi} \left(\frac{2}{x}\right)^\nu & \nu = 1, 2, 3, \ldots . \end{cases} \tag{D.15}$$

From equations D.4, D.13, and D.15, one can easily piece together the behavior

of the Hankel functions near 0.

$$\lim_{x\to 0} H_\nu^{(1)}(x) = \begin{cases} 0 & \nu \text{ not an integer} \\ 1 + \frac{2i}{\pi}\ln\frac{e^\gamma x}{2} & \nu = 0 \\ -\frac{i(\nu-1)!}{\pi}\left(\frac{2}{x}\right)^\nu & \nu = 1, 2, 3, \dots, \end{cases}$$
$$\lim_{x\to 0} H_\nu^{(2)}(x) = \begin{cases} 0 & \nu \text{ not an integer} \\ 1 - \frac{2i}{\pi}\ln\frac{e^\gamma x}{2} & \nu = 0 \\ \frac{i(\nu-1)!}{\pi}\left(\frac{2}{x}\right)^\nu & \nu = 1, 2, 3, \dots . \end{cases} \tag{D.16}$$

D.4 Basic Relations

The following is an abridged list of some basic properties of individual cylinder functions. A more complete list can be found in Gradshteyn and Ryzhik (1994) or Jahnke et al. (1960). If the order is specifically an integer, it is specified as n.

D.4.1 Relations of Particular Cylinder Functions

$$J_\nu(-x) = (-1)^\nu J_\nu(x) \tag{D.17}$$

$$\begin{aligned} H_{-\nu}^{(1)}(x) &= e^{i\nu\pi} H_\nu^{(1)}(x) \\ H_{-\nu}^{(2)}(x) &= e^{-i\nu\pi} H_\nu^{(2)}(x) \end{aligned} \tag{D.18}$$

$$\begin{aligned} J_{-n}(x) &= (-1)^n J_n(x) \\ Y_{-n}(x) &= (-1)^n Y_n(x) \end{aligned} \tag{D.19}$$

$$\begin{aligned} J_{\frac{1}{2}}(x) &= -Y_{-\frac{1}{2}}(x) \\ &= \sqrt{\frac{2}{\pi x}}\sin(x) \\ J_{-\frac{1}{2}}(x) &= -Y_{\frac{1}{2}}(x) \\ &= \sqrt{\frac{2}{\pi x}}\cos(x) \end{aligned} \tag{D.20}$$

$$\begin{aligned} H^{(1)}_{\frac{1}{2}}(x) &= -i\sqrt{\frac{2}{\pi x}}e^{ix} \\ H^{(1)}_{-\frac{1}{2}}(x) &= \sqrt{\frac{2}{\pi x}}e^{ix} \\ H^{(2)}_{\frac{1}{2}}(x) &= i\sqrt{\frac{2}{\pi x}}e^{-ix} \\ H^{(2)}_{-\frac{1}{2}}(x) &= \sqrt{\frac{2}{\pi x}}e^{-ix} \end{aligned} \tag{D.21}$$

D.4.2 General Properties

The following is an abridged list of some basic properties common to all cylinder functions. A more complete list can be found in Gradshteyn and Ryzhik (1994) or Jahnke et al. (1960). A cylinder function of order ν is denoted in general as $Z_\nu(x)$. The basic recursion relation for derivatives are

$$Z'_\nu(x) = Z_{\nu-1}(x) - \frac{\nu}{x}Z_\nu(x)$$

and

$$Z'_\nu(x) = \frac{\nu}{x}Z_\nu(x) - Z_{\nu+1}(x). \tag{D.22}$$

Finding the sum and difference between equations D.22, one gets the following two equations

$$2Z'_\nu(x) = Z_{\nu-1}(x) - Z_{\nu+1}(x) \tag{D.23}$$

and

$$\frac{2\nu}{x} Z_\nu(x) = Z_{\nu-1}(x) + Z_{\nu+1}(x). \tag{D.24}$$

References

Armstrong, J. T. (1994). Progress of the Big Optical Array (BOA). In Breckenridge, J. B., editor, *Amplitude and Intensity Spatial Interferometry II*, volume 2200 of *Proceedings of the SPIE*, pages 62–80, PO Box 10, Bellingham, Washington 98227-0010. SPIE. Conference held 15–16 March 1994, Kona, Hawaii.

Baldwin, J. E., Beckett, M. G., Boysen, R. C., Burns, D., Buscher, D. F., Cox, G. C., Haniff, C. A., Mackay, C. D., Nightengale, N. S., Rogers, J., Scheuer, P. A. G., Scott, T. R., Tuthill, P. G., Warner, P. J., Wilson, D. M. A., and Wilson, R. W. (1996). The first images from an optical aperture synthesis array: Mapping of Capella with COAST at two epochs. *Astronomy and Astrophysics Letters*, 306:L13–L16.

Barden, S. C., Armandroff, T., Massey, P., Groves, L., Rudeen, A. C., Vaughnn, D., and Muller, G. (1992). Hydra – Kitt Peak multi-object spectroscopic system. In Gray, P. M., editor, *Fibre Optics in Astronomy II*, volume 37 of *Astronomical Society of the Pacific Conference Series*, page 185, 390 Ashton Avenue, San Francisco, California 94112.

Barry, D. J. (1995). *Design of and Studies with a Novel One Meter Multi-Element Spectroscopic Telescope*. PhD thesis, Georgia State University, Atlanta, Georgia 30303-3083.

Bedding, T. R., Robertson, J. G., Marson, R. G., Gillingham, P. R., Frater, R. H., and O'Sullivan, J. D. (1992). MAPPIT: Interferometry with non-redundant masks and wavelength dispersion. In Beckers, J., and Merkle, F., editors, *High-Resolution Imaging by Interferometry II*, NOAO-ESO Conference Proceedings, pages 391–400, Karl-Schwarzschild-Strasse 2 D-8046, Garching bei München, Germany. European

Southern Observatory, European Southern Observatory. Conference held 15–18 October 1991.

Benson, J. A., Dyck, H. M., Ridgway, S. T., Dixon, D. J., Mason, W. L., and Howell, R. R. (1991). The infrared diameter of Alpha Herculis measured with a michelson interferometer. *Astronomical Journal*, 102(6):2091–2097.

Benson, J. A., Hutter, D. J., Elias II, N. M., Bowers, P. F., Johnston, K. J., Hajian, A. R., Armstrong, J. T., Mozurkewich, D., Pauls, T. A., Rickard, L. J., Hummel, C. A., White, N. M., Black, D., and Denison, C. S. (1997). Multichannel optical aperture synthesis imaging of Zeta 1 Ursae Majoris with the Navy Prototype Optical Interferometer. *Astronomical Journal*, 114:1221.

Born, M., and Wolf, E. (1989). *Principles of Optics: Electromagnetic Theory of Propagation, Interference and Diffraction of Light*. Pergamon Press, Maxwell House, Fairview Park, Elmsford, New York 10523, sixth (corrected) edition.

Boyce, W. E., and DiPrima, R. C. (1986). *Elementary Differential Equations and Boundary Value Problems*. John Wiley and Sons, New York, New York, fourth edition.

Boysen, R. C., and Rogers, J. (1992). The design of COAST. In Beckers, J., and Merkle, F., editors, *High-Resolution Imaging by Interferometry II*, NOAO-ESO Conference Proceedings, pages 921–928, Karl-Schwarzschild-Strasse 2 D-8046, Garching bei München, Germany. European Southern Observatory, European Southern Observatory. Conference held 15–18 October 1991.

ten Brummelaar, T. A. (1997). Correlation measurement and group delay tracking in optical stellar interferometry with a noisy detector. *Monthly Notices of the Royal Astronomical Society*, 285:135–150.

ten Brummelaar, T. A., and Bagnuolo, Jr., W. G. (1994). CHARA beam combiner design. In Breckenridge, J. B., editor, *Amplitude and Intensity Spatial Interferometry II*, volume 2200 of *Proceedings of the SPIE*, pages 140–151, PO Box 10, Bellingham, Washington 98227-0010. SPIE. Conference held 15–16 March 1994, Kona, Hawaii.

Buck, J. A. (1995). *Fundamentals of Optical Fibers*. John Wiley and Sons, New York, New York.

Buscher, D. F. (1988). *Getting the Most out of C.O.A.S.T.* PhD thesis, Cambridge University, Cambridge, United Kingdom.

Clark, B. G. (1994). Coherence in radio astronomy. In Perley, R. A., Schwab, F. R., and Bridle, A. H., editors, *Synthesis Imaging in Radio Astronomy*, volume 6 of *Astronomical Society of the Pacific Conference Series*, chapter 1, pages 1–10. Astronomical Society of the Pacific, 390 Ashton Avenue, San Francisco, California 94112.

Colavita, M. M., Shao, M., Hines, B. E., Wallace, J. K., Gursel, Y., Malbet, F., Yu, J. W., Singh, H., Beichman, C. A., Pan, X. P., Nakajima, T., and Kulkarni, S. R. (1994). ASEPS-0 testbed interferometer. In Breckenridge, J. B., editor, *Amplitude and Intensity Spatial Interferometry II*, volume 2200 of *Proceedings of the SPIE*, pages 89–97, PO Box 10, Bellingham, Washington 98227-0010. SPIE. Conference held 15–16 March 1994, Kona, Hawaii.

Cornwell, T., and Fomalont, E. B. (1994). Self-calibration. In Perley, R. A., Schwab, F. R., and Bridle, A. H., editors, *Synthesis Imaging in Radio Astronomy*, volume 6 of *Astronomical Society of the Pacific Conference Series*, chapter 1, pages 185–197. Astronomical Society of the Pacific, 390 Ashton Avenue, San Francisco, California 94112.

Coudé du Foresto, V., Perrin, G., Mariotti, J.-M., Lacasse, M. G., and Traub, W. (1996). The FLUOR/IOTA fiber stellar interferometer. In *Integrated Optics for Astronomical Interferometry*, Astrofib 96, pages 115–125. Conference held 15–16 October 1996, Grenoble, France.

Coudé du Foresto, V., and Ridgway, S. T. (1992). FLUOR: A stellar interferometer using single-mode infrared fibers. In Beckers, J., and Merkle, F., editors, *High-Resolution Imaging by Interferometry II*, NOAO-ESO Conference Proceedings, pages 731–740, Karl-Schwarzschild-Strasse 2 D-8046, Garching bei München, Germany. European Southern Observatory, European Southern Observatory. Conference held 15–18 October 1991.

Courant, R., and Hilbert, D. (1989). *Methods of Mathematical Physics*, volume 1 of *Wiley Classics*. John Wiley and Sons, New York, New York, first English edition. Translated and revised from the original German. Reissue of 1953 Interscience Publishers release.

Davis, J. (1993). The Sydney University Stellar Interferometer (SUSI). In Robertson, J. G., and Tango, W. J., editors, *Very High Angular Resolution Imaging*, pages 135–142, PO Box 322, 3300 AH Dordrecht, The Netherlands. Kluwer Academic Publishers. IAU Symposium 158 held at the Women's College, University of Sydney, Sydney, New South Wales, Australia.

Davis, J., and Tango, W. J. (1986). New determination of the angular diameter of Sirius. *Nature*, 323:234–235.

Di Benedetto, G. P., and Rabbia, Y. (1987). Accurate angular diameters and effective temperatures for eleven giants cooler than K0 by Michelson interferometry. *Astronomy and Astrophysics*, 188:114–124.

Dyck, H. M., Benson, J. A., Carleton, N. P., Coldwell, C., Lacasse, M. G., Nisenson, P., Panasyuk, A., Papaliolios, C., Pearlman, M. R., Reasenberg, R. D., Traub, W. A., Xu, X., Predmore, C. R., Schloerb, F. P., and Gibson, D. M. (1995). First 2.2 μm results from the IOTA interferometer. *Astronomical Journal*, 109(1):378–382.

Eickhoff, W., Yen, Y., and Ulrich, R. (1981). Wavelength dependence of birefringence in single-mode fiber. *Applied Optics*, 20(19):3428–3435.

Fried, D. L. (1965). The effect of wave-front distortion on the performance of an ideal optical heterodyne receiver and an ideal camera. In *Conference on Atmospheric Limitations to Optical Propagation*. United States National Bureau of Standards CRPL.

Gay, J., and Mekarnia, D. (1988). Infrared interferometry at CERGA. In Merkle, F., editor, *High-Resolution Imaging by Interferometry*, NOAO-ESO Conference Proceedings, pages 811–816, Karl-Schwarzschild-Strasse 2 D-8046, Garching bei München, Germany. European Southern Observatory, European Southern Observatory. Conference held 15–18 March 1988.

Gradshteyn, I. S., and Ryzhik, I. M. (1994). *Table of Integrals, Series and Products*. Academic Press, Boston, Massachusetts, fifth edition. Translated from the original Russian by Scripta Technica.

Jahnke, E., Emde, F., and Lösch, F. (1960). *Tables of Higher Functions*. McGraw-Hill Book Company, New York, New York, sixth edition. Originally published by B. G. Teubner Verlagsgesellschaft, Stuttgart, Germany.

Jennison, R. C. (1958). A phase sensitive interferometer technique for the measurement of the fourier transforms of spatial brightness distributions of small angular extent. *Monthly Notices of the Royal Astronomical Society*, 118:276–284.

Jeunhomme, L. B. (1983). *Single-Mode Fiber Optics – Principles and Applications*, volume 4 of *Optical Engineering*. Marcel Dekker, 270 Madison Avenue, New York, New York 10016.

Kim, E. J. (1989). Dispersed fringe group delay astrometry using the Mark III stellar interferometer. Master's thesis, Massachusetts Institute of Technology, Cambridge, Massachusetts. M.S.E.E.

Klein, M. V., and Furtak, T. E. (1986). *Optics*. John Wiley and Sons, New York, New York, second edition.

Koechlin, L. (1988). The I2T interferometer. In Merkle, F., editor, *High-Resolution Imaging by Interferometry*, NOAO-ESO Conference Proceedings, pages 695–704, Karl-Schwarzschild-Strasse 2 D-8046, Garching bei München, Germany. European Southern Observatory, European Southern Observatory. Conference held 15–18 March 1988.

Kolmogorov, A. (1961). Turbulence. In Friedlander, S. K., and Topper, L., editors, *Turbulence, Classic Papers on Statistical Theory*. Interscience, New York, New York.

Lawson, P. R. (1993). *Group Delay Tracking with the Sydney University Stellar Interferometer*. PhD thesis, Sydney University, Chatterton Astronomy Department, School of Physics, Sydney, New South Wales, Australia.

Marcuse, D. (1977). Loss analysis of single-mode fiber splices. *Bell System Technical Journal*, 56(5):703–718.

Marcuse, D. (1982). *Light Transmission Optics*. Electrical/Computer Science and Engineering. Van Nostrand Reinhold Company, 135 West 50th Street, New York, New York 10020, second edition.

McAlister, H. A. (1985). High angular resolution measurements of stellar properties. *Annual Reviews of Astronomy and Astrophysics*, 23:59–87.

McAlister, H. A., Bagnuolo, Jr., W. G., Hartkopf, W. I., Robinson, W. G., Garrison, A. K., ten Brummelaar, T. A., Beletic, J. W., Ridgway, S. T., Turner, N. H., Daley, W., Carey, R., Holland, D. E., Lindsey, G., Vaughan, R. G., and Furenlid, I. K. (1994). The CHARA Array: Final report to the National Science Foundation (Cooperative Agreement 90-08941). Technical report, Center for High Angular Resolution Astronomy, Georgia State University, Atlanta, Georgia, 30303-3083.

McAlister, H. A., Hartkopf, W. I., Hutter, D. J., and Franz, O. G. (1987). ICCD speckle observations of binary stars II. measurements during 1982-1985 from the Kitt Peak 4-m telescope. *Astronomical Journal*, 93(3):688–723.

Michelson, A. A. (1891). Measurement of Jupiter's satellites by interference. *Nature*, 45(1155):160–161. Published 17 December.

Michelson, A. A., and Pease, F. G. (1921). Measurement of the diameter of α Orionis with the interferometer. *Astrophysical Journal*, 53(4):249–259.

Shaklan, S. B. (1989). *Multiple Beam Correlation Using Single-Mode Fiber Optics with Application to Interferometric Imaging*. PhD thesis, University of Arizona, Tucson, Arizona.

Shaklan, S. B. (1990). Fiber optic beam combiner for multiple-telescope interferometry. *Optical Engineering*, 29(6):684–689.

Shaklan, S. B., and Roddier, F. (1987). Single-mode fiber optics in a long-baseline interferometer. *Applied Optics*, 26(11):2159–2163.

Shaklan, S. B., and Roddier, F. (1988). Coupling starlight into single-mode fiber optics. *Applied Optics*, 27(11):2334–2338.

Shao, M., Colavita, M. M., Hines, B. E., Staelin, D. H., Hutter, D. J., Johnston, K. J., Mozurkewich, D., Simon, R. S., Hershey, J. L., Hughes, J. A., and Kaplan, G. H. (1988). The Mark III stellar interferometer. *Astronomy and Astrophysics*, 193:357–371.

Snitzer, E. (1961). Cylindrical dielectric waveguide modes. *Journal of the Optical Society of America*, 51(5):491–498.

Tango, W. J., and Twiss, R. Q. (1980). Michelson stellar interferometry. *Progress in Optics*, XVII:239–277.

Tatarskii, V. I. (1961). *Wave Propagation in a Turbulent Medium*. McGraw-Hill, New York, New York.

Turner, N. H., Barry, D. J., and McAlister, H. A. (1992). Astrometric speckle interferometry for the amateur. In McAlister, H. A., and Hartkopf, W. I., editors, *Complementary Approaches to Double and Multiple Star Research*, volume 32 of *Astronomical Society of the Pacific Conference Series*, pages 577–579, 390 Ashton Avenue, San Francisco, California 94112.

Tyson, R. K. (1991). *Principles of Adaptive Optics*. Academic Press, Inc., 1250 6th Avenue, San Diego, California 92101.

Walker, G. A. H. (1987). *Astronomical Observations: An Optical Perspective*. Cambridge University Press, The Pitt Building, Trumpington Street, Cambridge, United Kingdom CB2 1RP.

Wangsness, R. K. (1986). *Electromagnetic Fields*. John Wiley and Sons, New York, New York, second edition.